Characterization of Ambient Aerosol Sources and Processes during CalNex 2010 with Aerosol Mass Spectrometry

Final Report
Contract 08-319

Prepared for:

California Air Resources Board and the
California Environmental Protection Agency
Research Division
P.O. Box 2815
Sacramento, CA 95812

Prepared by:

Principle Investigator:	Jose-Luis Jimenez
Subcontractor:	William H. Brune
Principle Scientist:	Patrick L. Hayes
Researchers:	Amber M. Ortega, Michael J. Cubison

Department of Chemistry & Biochemistry and
Cooperative Institute for Research in Environmental Sciences
University of Colorado
Boulder, CO 80309-0216

5 May 2013

Disclaimer

The statements and conclusions in this Report are those of the contractor and not necessarily those of the California Air Resources Board. The mention of commercial products, their source, or their use in connection with material reported herein is not to be construed as actual or implied endorsement of such products.

Acknowledgements

The authors thank the California Air Resources Board (Contract 08-319) for supporting this work. Patrick Hayes was also supported by a CIRES postdoctoral visiting fellowship. The authors would like acknowledge the numerous scientists who are involved the CalNex research effort. In particular we would like to thank the following for providing data or assisting in the analysis that is presented in this report: K. D. Froyd (PALMS particle type concentration); Y. Zhao and S. S. Cliff (XRF elemental concentration); W. W. Hu and D. W. Toohey (UHSAS number concentration); J. H. Flynn, N. Grossberg and B. L. Lefer (ozone and boundary layer height); S. Alvarez, B. Rappenglück and J. S. Holloway (CO); J. W. Taylor and J. D. Allan (SP-AMS and SP2 black carbon measurements); J. B. Gilman, W. C. Kuster and J. A. de Gouw (VOC concentrations); P. Massoli (aerosol extinction); X. Zhang, J. Liu and R. J. Weber (OCEC concentration); A. L. Corrigan and L. M. Russel (FTIR); G. Isaacman, D. R. Worton, N. M. Kreisberg, S. V. Hering and A. H. Goldstein (2D-TAG); R. Thalman, E. M. Waxman and R. Volkamer (NO_2 concentration); Y. H. Lin, J. D. Surratt, T. E. Kleindienst, J. H. Offenberg (Filter OC); S. Dusanter, S. Griffith and P. S. Stevens (OH concentration); J. Brioude and W. M. Angevine (back-trajectory calculations).

This Report was submitted in fulfillment of ARB contract 08-319, “Characterization of Ambient Aerosol Sources and Processes during CalNex 2010 with Aerosol Mass Spectrometry”, by the University of Colorado under the sponsorship of the California Air Resources Board. Work was completed as of Oct. 2012.

Table of Contents

List of Figures

List of Tables

Abstract

A suite of measurements from the CalNex Pasadena ground site are utilized to characterize aerosols, especially organic aerosols (OA), in the Los Angeles Basin. The concentrations of the species comprising $PM_{2.5}$ and PM_1 are quantified. Sea salt exhibits extensive chloride depletion due to chemical aging leading to substantial supermicron nitrate. Five OA components are identified using positive matrix factorization including hydrocarbon-like organic aerosol (HOA), cooking-influenced organic aerosol (CIOA), and two types of oxygenated organic aerosol (OOA). The correlations with tracers and photochemical age indicate that HOA is a surrogate for primary combustion OA, and OOA is dominated by secondary OA (SOA) mass. A majority of the OA mass is OOA, with lesser contributions from HOA and CIOA. HOA concentrations are lower on Sundays displaying a weekly cycle consistent with reductions in diesel emissions. The OOA to odd-oxygen (ozone + NO_2) ratios for Pasadena, Mexico City, and Riverside are nearly equal, suggesting that SOA and odd-oxygen formation rates are proportional at the different sites. Dilution-corrected OA enhancements for Pasadena increase with photochemical age similar to or slightly higher than analogous data for Mexico City and the northeastern United States. The OA elemental composition for Pasadena is described in a Van Krevelen diagram (H/C vs. O/C) and follows a line that is less steep than that observed in Riverside. The difference is attributed to the greater influence of freshly emitted HOA in Riverside, while the OOA factors from the two locations follow a common evolution. Overall the results demonstrate similarities in SOA properties across several urban locations. Within experimental uncertainties, OOA/ΔCO does not display a weekly cycle, which suggests the dominance of gasoline emissions in secondary OA (SOA) formation under the assumption that most urban SOA precursors are from motor vehicles. After propagation of uncertainties, a diesel contribution to SOA of 0 – 35% is calculated based on the lack of an observed weekly cycle.

Executive Summary

Background. Atmospheric aerosols (i.e., particulate matter or PM) have been the subject of intensive ongoing research due to their important impact on the radiative forcing of climate, which occurs through several mechanisms including the scattering and absorption of solar radiation as well as the alteration of the formation and properties of clouds. In addition, atmospheric aerosols reduce visibility and increase cardiac and respiratory disease in humans. The impact of aerosols on climate, the environment, and human health is determined, in part, by particle size and chemical composition. In many environments, including California, a large fraction (~50%) of the submicron aerosol mass in the lower portion of the atmosphere (i.e., the troposphere) is organic aerosol (OA). The sources, composition, and chemical processing of OA are not well understood, however. Generally, OA is comprised of thousands of individual compounds that are either directly emitted into the atmosphere ('primary' OA or 'POA') or are formed though chemical reactions involving gas phase precursors ('secondary' OA or 'SOA'). The multiple sources and complexity of molecular composition represent major challenges for understanding and prediction of OA properties. Elevated aerosol concentrations are often associated with megacities such as Los Angeles (LA), and particulate matter concentrations in LA are among the highest in the United States. Thus, to develop effective air pollution control strategies for particulates it is necessary to fully understand the sources, composition, and chemistry of aerosols, and in particular, organic aerosols.

Methods. The California Research at the Nexus of Air Quality and Climate Change (CalNex) field campaign was conducted in Spring 2010, and was a multi-institution effort to address outstanding scientific questions regarding air quality and pollution over the state of California. The CalNex campaign featured several research aircraft, the research vessel (R/V) Atlantis off the California coast, and two ground-sites in Pasadena and Bakersfield. A major scientific goal for CalNex was to improve scientific understanding of atmospheric aerosols in California, and specifically, characterize important SOA precursors and formation pathways, as well as the impacts of aerosols on radiative forcing and cloud formation. For CalNex the Pasadena ground site was uniquely equipped to characterize aerosols, and especially, organic aerosols. In total approximately 70 gas and particle phase measurements were taken at the site representing, one of the largest studies of aerosols and their precursors. Additionally, the ground site featured many state-of-the-art aerosol instruments including several that had never been field-deployed previously. This report presents a detailed analysis of aerosol measurements from multiple instruments deployed to the Pasadena ground site during CalNex. The goals of this work are to determine the contributions of various sources to aerosol mass loadings with a particular focus OA, as well as to quantitatively evaluate SOA formation for the Los Angeles Basin and compare it against other major urban regions. To achieve these goals the following approach is utilized: (1) Quantifying the aerosol composition including mass concentrations, sizes, and daily cycles at the Pasadena ground site; (2) Identifying OA sources using statistical analyses of field measurements, which includes examining OA component correlations with key tracers and the weekly cycles in OA component concentrations; (3) Comparing the time scales and efficiency of SOA formation against previous measurements conducted in Riverside, Mexico City, and the northeast United States.

Results. In Pasadena, OA accounts for 41% of the total submicron aerosol mass with the remainder composed of ammonium sulfate (24%), ammonium nitrate (23%), aged sea salt (5%), elemental carbon (3%), mineral dust (2%), metals (1%), and ammonium chloride (1%). The aerosol size distributions show that OA dominates at small diameters (less than ~200 nm), whereas the inorganic contribution is dominant at larger diameters (greater than ~600 nm) due to primarily ammonium nitrate, ammonium sulfate, and aged sea salt. Statistical analyses identified five components of the total OA mass. The identified components include fresh and aged SOA, as well as POA components from cooking and motor vehicles emissions. A large majority of the OA mass is classified as secondary (66%), but there are important contributions from the primary components with vehicle and cooking emissions accounting for approximately 12% and 17% of the total OA mass. POA from motor vehicles and elemental carbon exhibit weekly cycles with substantially lower concentrations on Sundays versus weekdays consistent with the well-known weekday/weekend effect in the Los Angeles Basin due to the decrease in commercial vehicle traffic on weekends. In contrast, SOA did not exhibit a weekday/weekend effect, within experimental uncertainties, which indicates that more than 65% of SOA is from non-diesel emissions. The OOA to odd-oxygen (O_3 + NO_2) ratio for Pasadena is similar to those observed in Riverside and Mexico City, which suggests that the ratios of SOA to odd-oxygen production rates are comparable at the different sites and that similar SOA and odd-oxygen formation chemistries dominate at all these locations. In addition, the dilution corrected OA increases with photochemical age and closely resembles the upper limit of analogous data from Mexico City and the northeastern United States. Thus, within experimental error, the OA production is similar or slightly more efficient in Pasadena compared to other locations. To understand if the chemical aging of OA is similar throughout the LA basin and consistent with other studies, the elemental composition of OA for Pasadena and Riverside was analyzed. This analysis suggests that the changes in SOA composition with aging are similar in Riverside and Pasadena, and consistent with the results from other field and laboratory measurements.

Conclusions. During CalNex OA and, in particular, SOA were observed to be large contributors to the total submicron particulate mass in Pasadena, which is consistent with previous measurements conducted in the LA basin over the past several years. The mean concentrations were 7.0 and 4.6 $\mu g/m^3$ for PM_1 OA and SOA, respectively, and the total average PM_1 concentration was 17 $\mu g/m^3$. For comparison the recently lowered EPA $PM_{2.5}$ standard is 12.0 $\mu g/m^3$ (annual average). Future air pollution control strategies will therefore need to explicitly address these components of particulate matter. The smallest particulates are predominately organic in composition, which has important implications for evaluating the health impacts of air pollution since smaller particles penetrate more deeply into the lungs and are linked to increased risk of disease. The findings reported here highlight several quantitative similarities in SOA properties observed across multiple locations including the ratios of SOA to odd-oxygen, the increases in OA with photochemical age, and the evolution of elemental composition. In addition, SOA concentrations do not exhibit lower concentrations on weekends, unlike POA. A single dominant SOA source, likely gasoline vehicles, would explain both this similarity in SOA properties across several locations as well as the lack of a weekday/weekend effect for SOA. Recommendations for future work include SOA modeling studies of LA and California using various box and 3-D models. Current SOA models are not well constrained, and the CalNex data set provides a unique opportunity to test these SOA models as well as other aspects of air quality models (e.g., emission inventories). In turn, improved SOA models will lead to a more detailed understanding of the important precursors and chemical pathways for SOA formation.

1. Introduction

Atmospheric aerosols have been the subject of intensive ongoing research due to their important impacts on the radiative forcing of climate, which occur through several mechanisms that include the scattering and absorption of solar radiation as well as the alteration of the formation and properties of clouds [*IPCC*, 2007]. In addition, atmospheric aerosols reduce visibility [*Watson*, 2002] and increase cardiac and respiratory disease in humans [*Dockery and Pope*, 1994; *Dockery et al.*, 1993]. The impact of aerosols on climate, the environment, and human health is determined, in part, by particle size and chemical composition. In many environments a large fraction (~50%) of the submicron aerosol mass in the troposphere is organic aerosol (OA), but the sources, composition and chemical processing of OA are not well understood [*Jimenez et al.*, 2009]. Generally, OA is comprised of thousands of individual compounds that are either directly emitted into the atmosphere (i.e. 'primary' OA or 'POA') or formed though chemical reactions involving gas phase precursors (i.e. 'secondary' OA or 'SOA'). The multiple sources and complexity of molecular composition represent major challenges for understanding and prediction of OA properties.

Elevated aerosol concentrations are often associated with megacities such as Los Angeles (LA). Particulate matter concentrations in LA are among the highest in the United States [American Lung Association, 2011], and multiple previous measurement campaigns have aimed to characterize aerosols in this region. These campaigns include the 1987 Southern California Air Quality Study (SCAQS) [*Lawson*, 1990], the 1997 Southern California Ozone Study (SCOS97-NARSTO) [*Croes and Fujita*, 2003], the Study of Organic Aerosol at Riverside, which took place in the Summer (SOAR-1) and Fall (SOAR-2) of 2005 [*Docherty et al.*, 2011], and the 2009 Pasadena Aerosol Characterization Observatory (PACO) [*Hersey et al.*, 2011]. In addition, several research flights were performed over California and LA during the Arctic Research of the Composition of the Troposphere from Aircraft and Satellites Campaign (ARCTAS-CARB) [*Jacob et al.*, 2010]. Using data from these campaigns it has been shown that SOA represents a majority of the total OA mass in both Riverside [*Docherty et al.*, 2008] and Pasadena, CA [*Hersey et al.*, 2011], which is similar to findings in other urban regions [*Jimenez et al.*, 2009]. Also, vehicle emissions, food cooking, biomass burning, and primary biogenics have all been identified as sources of POA in the Los Angeles Basin [*Williams et al.*, 2010; *Wonaschutz et al.*, 2011].

The California Research at the Nexus of Air Quality and Climate Change (CalNex) field campaign was conducted in Spring 2010, and was a multi-institution effort to address outstanding questions regarding atmospheric chemistry processes over the state of California and the adjacent Pacific coastal region. The CalNex campaign featured several research aircraft, the research ship R/V Atlantis off the California coast, and two ground-sites in Pasadena and Bakersfield. A major scientific goal for CalNex was to improve scientific understanding of atmospheric aerosols in California, and specifically, characterize important SOA precursors and formation pathways, as well as the impacts of aerosols on radiative forcing and cloud formation [NOAA, 2008]. For CalNex the Pasadena ground site was uniquely equipped to characterize aerosols, and especially, organic aerosols. In total approximately 70 gas and particle phase

measurements were taken at the site representing, to our knowledge, one of the largest studies of aerosols and their precursors. A full list of the instrumentation is available in the CalNex overview [*Ryerson et al.*, manuscript in preparation, 2012] and also at: http://tinyurl.com/CalNex. Additionally, the ground site featured many state-of-the-art aerosol instruments including several that had never been field-deployed previously.

Here we present a detailed analysis of aerosol measurements from multiple instruments, including on- and off-line bulk and single particle methods, deployed to the Pasadena ground site during CalNex. The goals of this work are to determine the contributions of various sources to aerosol mass loadings with a particular focus OA, as well as to quantitatively evaluate SOA formation for the Los Angeles Basin and compare it against other major urban regions. To achieve these goals the following approach is utilized: (1) Quantifying the aerosol composition including mass concentrations, size distributions, and diurnal cycles at the Pasadena ground site; (2) Identifying OA sources using positive matrix factorization (PMF), as well as examining OA component correlations with key tracers and the weekly cycles in OA component concentrations; (3) Comparing the time scales and efficiency of SOA formation against previous measurements conducted in Riverside, Mexico City, and the northeastern United States using the ratios of SOA to odd-oxygen (O_x, O_3 + NO_2) and SOA to CO enhancement; (4) Contrasting the different evolution of OA elemental composition for Pasadena and Riverside. Ultimately, this work aims to provide results that can be used to better evaluate and constrain representations of aerosols in atmospheric chemistry models.

2. Materials and Methods

I. CalNex ground site in Pasadena, California

The CalNex Pasadena ground site was located on the California Institute of Technology (Caltech) campus in Pasadena, California (34.1406 N, 118.1225 W, 236 m above mean sea level). The measurement period was May 15 2010 00:00 – June 16 2010 00:00 (local time). The Pasadena ground site was located 18 km northeast of downtown Los Angeles. Pasadena lies within the Los Angeles Basin, which is bordered on the north and east by the San Gabriel, San Bernardino, and San Jacinto mountains as well as on the southwest by the Pacific Ocean. Pasadena is part of the dense, urban Los Angeles metropolitan area. The prevailing wind direction during daytime in Pasadena was from the southwest due to the sea-breeze, which brought air masses from the Santa Monica and San Pedro Bays through central Los Angeles to Pasadena (FLEXPART back-trajectories are available in Appendix A). At nighttime winds were weaker and were most frequently from the southwest or southeast. Sunrise and sunset were approximately 5:30 and 20:00 (local time) during the sampling period. Boundary layer height, temperature, and relative humidity (RH) data are presented in Appendix A (Figure A-1) along with wind roses (Figure A-2).

II. AMS sampling and analysis

The concentrations of submicron non-refractory ($nrPM_1$) organic and inorganic (nitrate, sulfate, ammonium, chloride) aerosol particles were measured using an Aerodyne High Resolution Time-of-Flight Aerosol Mass Spectrometer (hereinafter referred to as 'AMS') [*DeCarlo et al.*, 2006]. The AMS sampled from an inlet equipped with a $PM_{2.5}$ cyclone located 2 m above the roof of the container housing the instrument. The sampled air passed through a 6.8 m insulated copper inlet line and a dryer prior to analysis by the AMS. The resulting data were averaged over 2.5 minute intervals. The ion paths through the time-of-flight chamber were alternated between "V" and "W" modes every 150 s, and the reported concentrations correspond to V-mode acquisition periods only. Size distributions were acquired in V-mode only by operating the AMS in particle time-of-flight (PToF) mode [*Jimenez et al.*, 2003]. All data were analyzed using standard AMS software (SQUIRREL v1.51 and PIKA v1.10) within Igor Pro 6.2.1 (WaveMetrics, Lake Oswego, OR) [*Sueper*, 2011].

It is well-known that for most ambient sampling conditions a collection efficiency (CE) correction must be applied to the AMS data to account for particle bounce from the AMS vaporizer [*Middlebrook et al.*, 2012]. Mass concentrations are typically calculated with a default CE of 0.5. The degree to which particles bounce, and hence collection efficiency, are a function of particle phase, which is influenced by the relative humidity of the sampling line, the acidity/neutralization of the sulfate content, the ammonium nitrate content, and the organic liquid content [*Middlebrook et al.*, 2012]. The sample flow was dried as described above, and the sulfate content was largely neutralized (see Section 3.I.B below). Thus, these experimental parameters are not expected to impact CE. Ammonium nitrate concentrations varied widely during the measurement period though, and accordingly a nitrate-dependent CE is applied following Nemitz et al. [2010]. Quantifying the organic liquid content is challenging for ambient samples, however the ratio of AMS mass to Scanning Mobility Particle Sizer (SMPS) mass exhibits no dependence on the amount OA oxidation as measured by O:C indicating that phase changes associated with organic material are either not occurring or are not influencing the CE.

In total, the aerosol mass concentrations measured by the AMS after applying the CE correction, which ranged from 0.5 to 0.7, are consistent with most other measurements from the Pasadena ground site. The relevant inter-comparisons are discussed in Appendix B including details regarding how mass concentrations are calculated from SMPS number distributions.

High-resolution (HR) analysis of the mass spectra, including application of the HR AMS fragmentation table, was carried out following previously published procedures [*Aiken et al.*, 2007, 2008]. The reported AMS mass concentrations were determined from the HR AMS spectra and are very similar to unit mass resolution (UMR) concentrations, within 5%, that are determined using the UMR fragmentation table of Allan et al [2004]. The HR fragmentation table was also used to obtain the OA mass spectral matrix for the PMF analysis described in the next paragraph.

The OA mass spectral matrix was deconvolved into components using PMF, a receptor-based factorization model [*Paatero and Tapper*, 1994]. The application of PMF to AMS spectra has been discussed in detail previously [*Ulbrich et al.*, 2009; *Q Zhang et al.*, 2011]. The same method is used here including the PMF2 algorithm, which is run in robust mode via the PMF Evaluation Tool panel (PET, v2.03). The high-resolution organic aerosol mass spectra for the entire CalNex campaign were analyzed, and the full range of the high-resolution spectra was utilized (*m/z* 12 – 204). Error matrices were calculated using the methods of Allan et al. [2003] and Ulbrich et al. [2009]. Weak variables (i.e. *m/z*'s) with lower signal-to-noise ratios ($0.2 < S/N < 2$) were down-weighted by a factor of three, and bad variables ($S/N \leq 0.2$) were down-weighted by a factor of 10 following the recommendations of Paatero and Hopke [2003]. For the results presented here the model error was set to zero.

A metastable atom bombardment (MAB)-AMS instrument [*Robinson et al*., 2011] was also deployed during CalNex-LA with the goal of obtaining more detailed spectra of organic aerosols using a softer ionization method. However due to technical problems with a new quadrupole filter and a vacuum accident due to power loss at the site the data quality from this instrument was not sufficient to warrant detailed analyses. More recently our group has shifted to chemical ionization mass spectrometry (CIMS) [*Yatavelli et al.,* 2012] as a more sensitive and softer technique for these objectives.

III. Co-located CalNex measurements utilized in this study

A SMPS (Model 3936, TSI Inc.) measured ambient number distributions between 7 and 690 nm mobility diameter. The SMPS was operated at a sampling frequency of 5 min and used the same inlet as the AMS except that the aerosol flow passed through an additional 2.1 m of copper inlet line (0.3 lpm flow). Ambient particle number distributions were also measured from 60 to 1000 nm using an Ultra-High Sensitivity Aerosol Spectrometer (UHSAS, Droplet Measurement Technologies), which also used the same inlet as the AMS, but the sample flow passed through an additional 2 m of inlet line (0.3 lpm flow). A White-Light Optical Particle Counter (WLOPC, Climet model 208 fitted with a multi-channel analyzer) measured size distributions from 500 to 4000 nm. Hourly $PM_{2.5}$ organic carbon (OC) and elemental carbon (EC) concentrations were measured using a Sunset Labs field OC/EC analyzer [*Peltier et al.*, 2007]. Blank-corrected optical OC and EC data from the Sunset field analyzer are reported here. Measurements of refractory black carbon (rBC) were performed with a Single Particle Soot Photometer (SP2, Droplet Measurement Technologies) [*Schwarz et al.*, 2006], as well as with a

Soot Particle Aerosol Mass Spectrometer (SP-AMS, Aerodyne Research & Droplet Measurement Technology) [*Onasch et al.*, 2012]. The concentrations of semi-volatile and particulate organic molecular tracers were measured by 2-D Thermal Desorption Aerosol Gas Chromatography Mass Spectrometry (2DTAG, UC-Berkeley & Aerosol Dynamics) [*Worton et al.*, 2012]. $PM_{2.5}$ nitrate and sulfate concentrations were measured with a Particle-into-Liquid Sampling and Ion Chromatography (PILS-IC) system [*Orsini et al.*, 2003]. The Particle Analysis by Laser Mass Spectrometry (PALMS) instrument provided number fractions for individual particle composition classes from 190 – 4000 nm [*Froyd et al.*, 2009; *Thomson et al.*, 2000]. The size-resolved PALMS number fractions were mapped onto volume distributions from SMPS and WLOPC measurements to determine the volume concentrations for the PALMS particle classes. Particle optical extinction for PM_1 was measured at 532 nm and 630 nm by a Cavity Attenuated Phase Shift (CAPS) instrument [*Kebabian et al.*, 2007; *Massoli et al.*, 2010]. All of the online measurements described in this paragraph were located at the CalNex ground site described above.

Data from offline particulate matter measurements are included in this paper as well. In particular, size-resolved elemental concentrations were determined by X-ray Fluorescence (XRF) analysis of Mylar substrates from a rotating drum impactor (RDI). The XRF analysis was performed at the Advanced Light Source at Lawrence Berkeley National Lab. Using the XRF results, the mineral dust concentration corresponding to oxides of Al, Si, Ca, K, Fe, and Ti is estimated from the elemental concentrations following the method of Simon et al. [2011] and Malm et al. [1994]. The particulate metal concentration is calculated as the sum of the mass concentrations of Mg, V, Cr, Mn, Co, Ni, Cu, Zn, Ga, As, Se, Rb, Sr, Y, Zr, Mo, and Pb. The Cl concentrations from XRF measurements are reported as refractory chloride (rCl), since the placement of samples under vacuum for analysis is expected to cause evaporation of non-refractory species such ammonium chloride. The time resolution of the XRF data was 1.5 h. Offline $PM_{2.5}$ OC measurements of high volume samples collected with quartz fiber filters were performed using three separate sets of filters and two laboratory-based Sunset Labs OC/EC analyzers (NIOSH TOT protocol). For clarity, the three sets of filters are named according to the institution that collected them: Georgia Institute of Technology (GIT), U.S. Environmental Protection Agency (EPA), and University of North Carolina (UNC). Following the technique of Russell et al. [2009a], Fourier Transform Infrared Spectroscopy (FTIR) analysis of Teflon filter samples provided total OA and organic functional group mass concentrations. All samples for offline analyses were collected at about 12 m above ground level on the roof of the Keck Building located on the Caltech campus approximately 0.3 km southwest of the ground site.

The concentration of O_3 was measured by UV differential absorption (49c Ozone Analyzer, Thermo Scientific), and CO concentrations were measured by two vacuum-UV resonance fluorescence instruments (AL5001 & AL5002, Aerolaser) [*Gerbig et al.*, 1999]. An in-situ Gas Chromatography Mass Spectrometry (GC-MS) instrument provided the mixing ratios for a variety of VOCs [*Gilman et al.*, 2009]. A Fluorescence Assay by Gas Expansion (FAGE) instrument was utilized to determine the OH concentration [*Dusanter et al.*, 2009]. The NO_x and NO_y concentrations were measured using chemiluminescence (42i-TL with Mo converter, Thermo Scientific), and NO_2 was measured with Cavity Enhanced Differential Optical Absorption Spectroscopy (CE-DOAS) [*Thalman and Volkamer*, 2010]. The CE-DOAS instrument was located on the Caltech Millikan Library roof, which is approximately 45 m tall and 0.5 km southwest of the Pasadena ground site.

Meteorological data were acquired by a station that included a temperature/RH sensor (Campbell Scientific Inc., HMP35C) and a wind monitor (R.M. Young, 05103). The boundary layer height was determined using a ceilometer (Vaisala, CL31) following the method described by Haman et al. [2012], and the ceilometer results have been shown to be consistent with boundary layer heights from Weather Research Forecasting (WRF) modeling [*Washenfelder et al.*, 2011]. To track the origins of the air masses sampled at the ground site, a modified version of the FLEXPART Lagrangian particle dispersion model [*Stohl et al.*, 2005] was used to calculate back trajectories of air masses based on advection and turbulent mixing processes. The main modification consists of using time-averaged winds from the WRF (version 3.3) meteorology model instead of instantaneous winds to improve uncertainties within the FLEXPART model [*Nehrkorn et al.*, 2010]. The WRF output has a spatial grid of 4 km x 4 km, with a temporal resolution of 30 min and 60 vertical levels. Lastly, all linear regressions in this paper are performed as orthogonal distance regressions using Igor Pro 6.2.1 software. The Glossary of Terms, Abbreviations, and Symbols defines the acronyms used in this paper.

3. Results and Discussion

I. Total submicron aerosol composition

I.A. Time series, diurnal cycles, and size distributions

The time series for $nrPM_1$ species and EC are shown in Figure 1B. In addition, the diurnal cycles of the different $nrPM_1$ species and EC are shown in Figure 2A. The time series for metals, mineral dust, and refractory chloride (rCl) are shown in Figure 1C, and for comparison the PALMS particle type time series are included in Figure 1 as well (Panels D and E). The fractional composition of the total submicron mass is determined by combining the AMS, XRF, and PALMS measurements (Figure 2B). In the interpretation of the data in Figures 1 and 2 it is important to consider some differences in size cuts of the measurements. First, the XRF measurements used in Figures 1 and 2 correspond to a size cut of 1150 nm aerodynamic diameter. By linearly interpolating the size-resolved XRF measurements the average overestimate relative to the actual PM_1 concentrations was found to be approximately 30%. Second, the online Sunset OC/EC analyzer was equipped with a $PM_{2.5}$ cyclone for most of the campaign. From 6/12 through 6/16 the EC measurement was performed while switching between a $PM_{2.5}$ and PM_1 cyclone, and the ratio of the PM_1 EC to the linearly interpolated $PM_{2.5}$ EC was 0.93 (±0.19 standard deviation). Thus, while the EC data in Figures 1 and 2 may overestimate the true PM_1 EC concentrations, it is expected that this error will be small (~7%). Despite these overestimates of refractory mass, the total PM_1 concentration is still dominated by non-refractory species (OA + sulfate + nitrate + ammonium + nrCl) that account for 93% of the measured mass. Similarly, particle types measured by the PALMS instrument that are predominately composed of non-refractory material comprised 90% of submicron aerosol volume (Figure 3).

A clear diurnal cycle is observed for most $nrPM_1$ species. As shown in Figure 2, the maxima in the EC and CO (commonly used combustion emission tracers) diurnal cycles are both observed between 12:00 and 13:00 PDT (local time). These maxima do not coincide with the Los Angeles County morning rush hour, which occurs between about 06:00 and 08:00 PDT [*Caltrans*, 2010]. Instead, they appear to result from polluted air masses that are initially emitted in the source-rich western LA Basin earlier in the day and are transported to Pasadena over several hours. The wind speed and wind direction measured at the ground site are consistent with this transport. In addition, FLEXPART back-trajectories show that the air masses over the Pasadena ground site when EC and CO concentrations are highest have significant footprint residence times over the western LA basin. In particular, downtown LA as well as the Ports of LA and Long Beach are regions with significant combustion emissions that are likely to impact Pasadena given the back-trajectories. In a previous publication, back-trajectory calculations run for 18 days during the CalNex campaign identified 8 days that were characterized by direct transport from the coast inland to the ground site [*Washenfelder et al.*, 2011], with an average transport time of 3.25 hours for air parcels arriving at 16:00 PDT. Other studies in the LA Basin have reached the same conclusion that Pasadena is a receptor site of pollution from the western basin [*Hersey et al.*, 2011; *Veres et al.*, 2011]. Compared to EC and CO, the OA concentrations peak later in the day, about 3 pm, which corresponds to the time-of-day when air masses over the Pasadena ground site were the most photochemically processed (Figure 2C). The photochemical age calculation is discussed further in Section 3.II.F below.

The submicron nitrate diurnal cycle is different from OA with a peak in the morning. The afternoon decrease in nitrate can be attributed to both vertical dilution due to the increase in boundary layer height as well as the higher temperatures and lower RH values that favor evaporation of ammonium nitrate [*Neuman et al.*, 2003]. In Pasadena both nitric acid and ammonia exhibit peaks around noon and elevated concentrations in the afternoon, which is consistent with volatilization of ammonium nitrate [*Veres et al.*, 2011; Ellis et al., Manuscript in Preparation, 2012]. The diurnal cycle of sulfate is not influenced by temperature because ammonium sulfate is non-volatile at atmospheric temperatures, and the sulfate maximum is observed in the afternoon, which may be due to advection to the Pasadena ground site from sources in the western LA Basin and/or photochemical production of sulfate.

In addition to the diurnal cycles, substantial additional variability is evident in Figure 1. In particular, from June 2nd through June 6th there appears to be a high pollution episode where a steady increase in organic aerosol concentrations occurs that is most evident during the nighttime and morning hours. A similar, second high pollution episode is observed at the end of the campaign (June 13th – June 16th). These episodes were likely the result of synoptic conditions that trapped pollution in the LA Basin overnight in the boundary layer and in residual layers aloft that tend to contain more aged air [*Lu and Turco*, 1995]. The aerosols and precursor species in the residual layer may then be entrained down into the mixed layer the next day as the boundary layer grows. These two high pollution episodes occurred during periods of lower boundary layer height (Figure A-1 in Appendix A), which suggests limited ventilation out of the LA Basin to the north and east past the San Gabriel, San Bernardino, and San Jacinto Mountains [*Duong et al.*, 2011]. During the first high pollution episode a build-up of EC and CO concentrations over several days is clearly seen. A similar but smaller build-up is seen during the second high pollution period at the end of the campaign. Given that EC and CO are primary pollutants, this observation provides further evidence for recirculation in the LA Basin during these periods. Contrastingly, a distinct period of greater marine influence is observed between May 20th and 25th. The highest concentrations of rCl are observed during this period, as well as a prominent rCl diurnal cycle (Figure 1C). Dimethyl sulfoxide concentrations, a well-known indicator of marine influence, are also elevated during this period and exhibit a similar diurnal pattern (data not shown).

Shown in Figure 2D is the relative contribution of each species to the submicron mass as a function of the total mass. A probability density distribution of the submicron mass is displayed as well (right axis). All data represent three hour averages. The relative composition does not vary greatly between low and high concentration periods. Nitrate becomes more important with increasing total concentrations (up to 29%). OA is important at all concentrations and is typically 40% of PM_1. The data in Figure 2D illustrate that OA and ammonium nitrate contribute substantially to the number of high PM_1 events.

In Table 1 the campaign average mass concentrations reported in Figure 2B are compared against those from two previous campaigns that took place in LA basin: SOAR-1 [*Docherty et al.*, 2011] and PACO [*Hersey et al.*, 2011]. It should be noted that the PACO campaign consisted of three periods, and for the purpose of this comparison the first and third periods were selected, since those portions of PACO took place at the same time of year as CalNex and SOAR-1, respectively. The fractional composition of $nrPM_1$ (and EC for CalNex and SOAR-1) is similar between the sites despite the different locations and years for the campaigns. The dominant

fraction is OA, which accounts for about half of the total mass. Sulfate and nitrate are the next largest fractions ranging between 16 – 30% and 15 – 22% of the total mass, respectively. The relative amount of ammonium is surprisingly consistent between the campaigns accounting for 12 – 13% of the total mass, while the chloride is a small percentage for all the studies. In Pasadena and Riverside EC accounted for 3% and 4% of the aerosol mass concentration, respectively.

As mentioned above, the volume concentration time series for particle composition types identified by the PALMS single-particle instrument are shown in Figures 1D and 1E. In addition, the campaign average volume concentrations are summarized in the pie charts shown in Figures 3A and 3B. The particle composition types were identified from PALMS mass spectra following the method described in Froyd et al. [2009]. For instance, biomass burning spectra are identified by a prominent K^+ peak along with organic peaks and a lack of other metals. Vanadium with organic species was used as a tracer to identify aerosol from heavy oil combustion (e.g. from ship engines), which allows for the definition of a new particle class termed 'Oil Combustion'. Since the PALMS is a single-particle instrument, it is capable of determining aerosol mixing state. One consideration when comparing the PALMS results against the AMS and other measurements is that the classification of particles typically follows the most abundant components in a particle, but the PALMS volume concentration for each particle type also includes secondary material that has condensed on the particle and may even dominate the particle volume at the time of detection. For the Pasadena ground site it was observed that all the particle types contained substantial amounts of nitrate, sulfate and organics, which indicates that condensation of secondary material is occurring on primary aerosols including sea salt and mineral dust. The nitrate observed on sea salt particles is also at least partially due to the heterogeneous reaction between sea salt and nitric acid as described below. As seen in Figure 3A the PM_1 aerosol volume concentration is dominated by Sulfate/OA/Nitrate type particles, while there are lesser contributions from biomass burning, oil combustion, EC, mineral/road dust, and sea salt particle types. In contrast, the coarse aerosol is dominated by sea salt particles. These findings are generally consistent with the mass concentration data from XRF and AMS measurements. The PALMS biomass burning results are discussed further in section 3.II.A.

Displayed in Figure 4 are the AMS size distributions (Panel A), XRF size distributions (Panel C), and the contribution of all species to the total aerosol mass as a function of particle size (Panel D). The rBC size distribution was measured by the SP-AMS and is normalized to the total EC concentration measured by the online Sunset analyzer. As seen in Figures 4A and 4D, the smaller particles, especially those below 200 nm are predominately composed of OA, and to lesser extent, rBC. In contrast, the larger particles have an increasing inorganic contribution due to nitrate, sulfate, ammonium, and the non-EC refractory components. The AMS size distributions have a gradual cut of approximately PM_1, and can have a tail due to slow evaporating particles [*M R Canagaratna et al.*, 2004] and should be interpreted accordingly. Also shown in Figure 4E are the PALMS size distributions, which feature a broad submicron mode that is dominated by the sulfate/organic/nitrate particle type as well as a supermicron mode composed primarily of sea salt. The PALMS distributions above 2.5 µm and below 200 nm underestimate concentrations due to instrument limitations associated with both the PALMS and WLOPC.

Further information about the OA, nitrate, and sulfate size distributions can be inferred from comparisons of various PM_1 and $PM_{2.5}$ measurements. For sulfate and OA the comparisons indicate that on average an overwhelming majority of the mass for these species is below 1 µm, but for nitrate there appears to be a substantial amount mass above 1 µm. Specifically, a regression analysis of OC concentrations from the AMS, a PM_1 instrument, and several $PM_{2.5}$ OC time series taken from the GIT, EPA, and UNC filter samples results in slopes greater than 0.81, when the AMS data is plotted on the y-axis. (Appendix B contains further details about the OA, sulfate, and nitrate comparisons.) This observation indicates that less than about 20% of the OC mass is above 1 µm. Similarly, a regression analysis of sulfate concentrations from the AMS and a $PM_{2.5}$ PILS-IC instrument results in slope of 1.01 leading to the conclusion that the sulfate mass above 1 µm is insignificant on average. The regression analysis of AMS and PILS-IC concentration data for nitrate results in a much different finding, and exhibits slope of 0.64 that is also dependent on sea salt concentrations measured by the PALMS instrument. These observations indicate that a substantial amount of nitrate mass is present above 1 µm, about 35%, and that the supermicron nitrate is at least partially comprised of sodium nitrate from chemical aging of sea salt by nitric acid although some supermicron ammonium nitrate may be present as well. The PILS-IC inlet was alternated between a PM_1 and $PM_{2.5}$ cyclone for a portion of the measurement period (6/12 – 6/16), which provides data that can also be used to assess the amount of sulfate and nitrate between 1 and 2.5 µm. The linear regression of the PM_1 and linearly interpolated $PM_{2.5}$ data indicate that 34% and 80% of the nitrate and sulfate mass was present below 1 µm. (Note: Interpolation of the $PM_{2.5}$ data is since only a single inlet and cyclone were used for a single PILS-IC measurement preventing simultaneous measurements with different size cuts.) Similar to the AMS versus PILS comparison, these percentages indicate that the supermicron mass represents a greater fraction of the $PM_{2.5}$ mass for nitrate relative to sulfate. When using the PILS data with alternating cyclones a larger percentage of supermicron mass is found than in the AMS versus PILS comparison. This difference may be due to the stronger influence of sea salt during the portion of the campaign when the cyclones were alternated, as clearly seen in the PALMS time series (Figure 1E), which is consistent with substantial amounts of sodium nitrate, and to a lesser extent sodium sulfate, above 1 µm. The aging of sea salt upon exposure to pollution is described further in the next section.

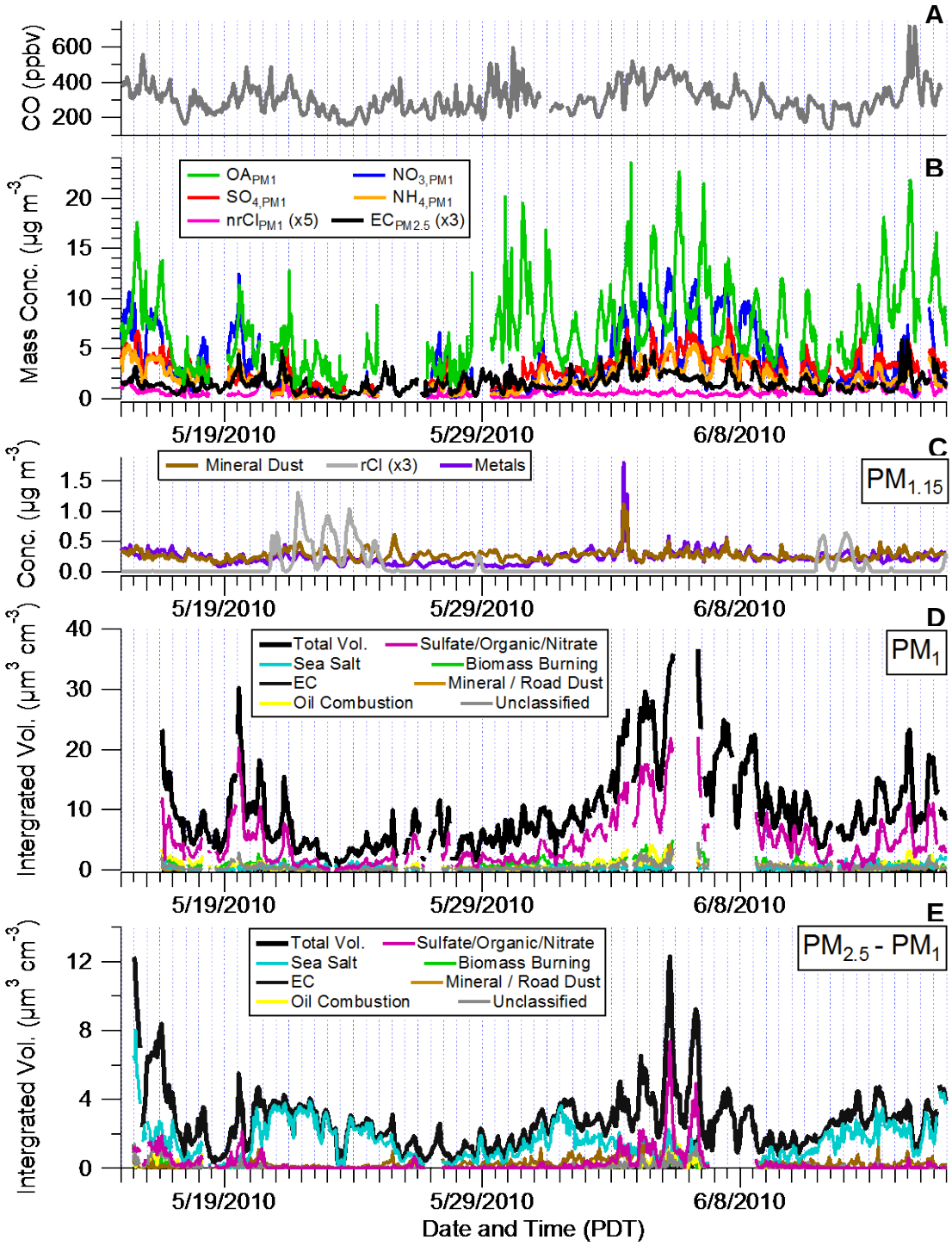

Figure 1: (A) Time series for CO concentrations. **(B)** Time series of the non-refractory PM_1 aerosol mass concentrations sampled by the AMS. The measured species are organics (OA), nitrate (NO_3), sulfate (SO_4), ammonium (NH_4), and non-refractory chloride (nrCl). The elemental carbon (EC) concentration was measured *in-situ* by a Sunset OC/EC Analyzer. **(C)** Time series of refractory $PM_{1.15}$ aerosol mass concentrations as measured by XRF (rCl: Refractory Chloride). **(D)** Time series of particle type volume concentrations as measured by the PALMS instrument for PM_1, and **(E)** for particles between 1 and 2.5 µm diameters. Note: All size cuts are for aerodynamic diameters.

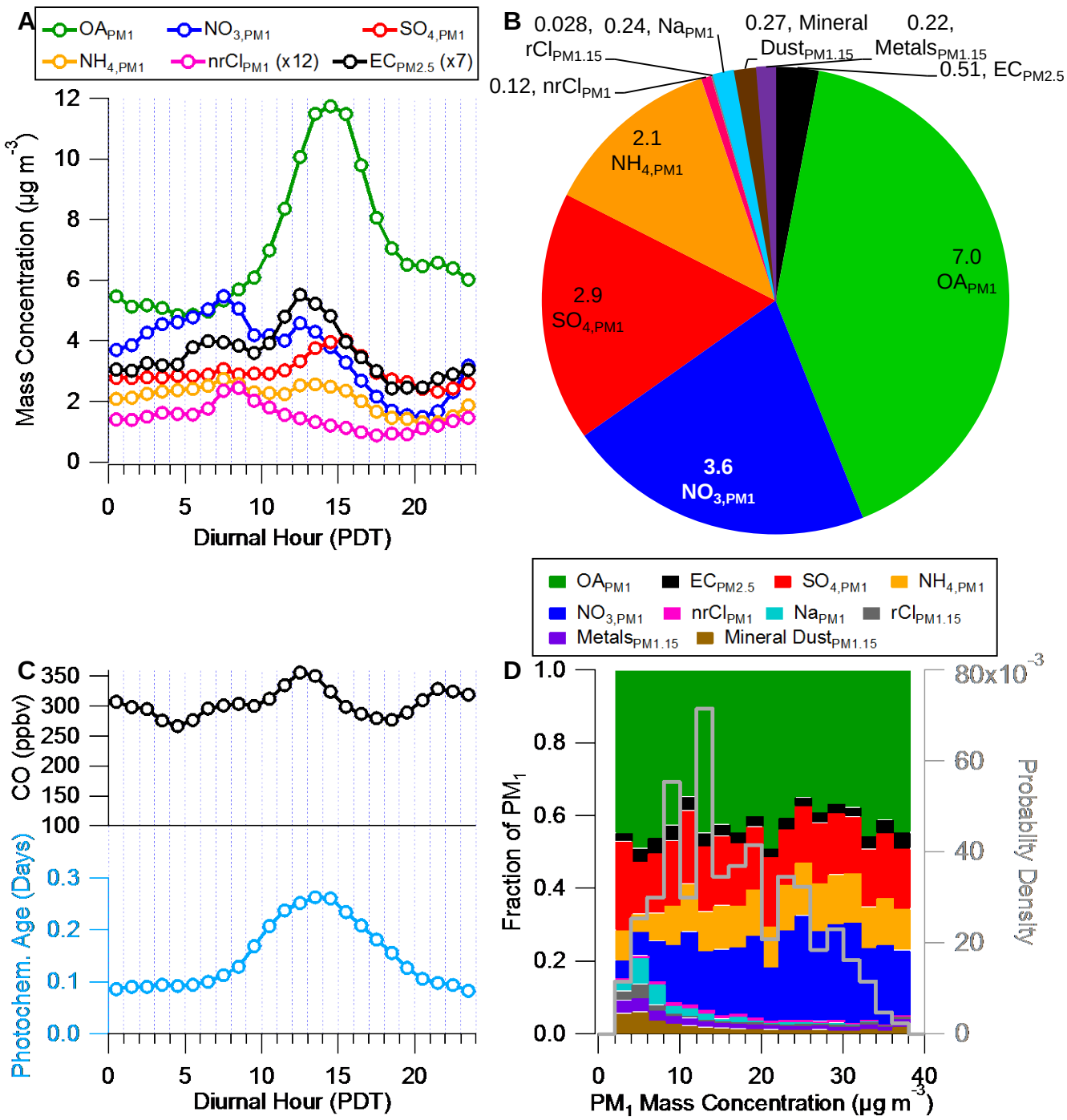

Figure 2: (A) Diurnal profiles for the non-refractory PM_1 mass concentrations and for EC. **(B)** Average PM_1 mass concentration for the ground site during the CalNex campaign including both refractory and non-refractory components. The sodium concentration is estimated from PLAMS sea salt volume concentrations using a $NaNO_3$ density of 2.1 g cm^{-3} [*Zelenyuk et al.*, 2005] and a sodium to sea salt mass ratio of 0.308 [*Hall and Wolff*, 1998]. **(C)** Diurnal cycles of CO and photochemical age for the Pasadena ground site. The photochemical age is determined using the method of Parrish et al. [2007] and the ratio of 1,2,4-trimethylbenzene to benzene. **(D)** The fraction of the total submicron aerosol mass contributed by different aerosol species as a function of the total mass. Also shown is a histogram of the total submicron aerosol mass (right axis).

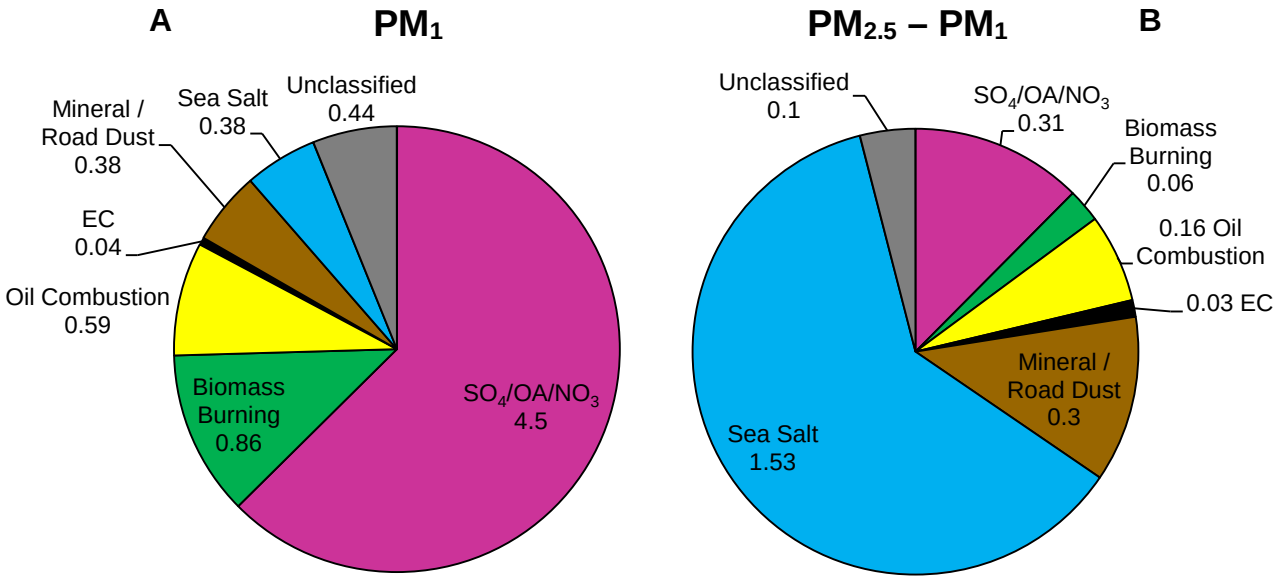

Figure 3: Average volume concentration (in $\mu m^3\ cm^{-3}$) of the different PALMS particle types for **(A)** PM_1 and **(B)** particles between 1 and 2.5 µm diameters at the Pasadena ground site during CalNex. Size ranges correspond to aerodynamic diameters.

Table 1: Summary of campaign average mass concentrations as a percent of the total $nrPM_1$ and EC during CalNex, SOAR-1, and PACO. (Note: Campaign average EC concentrations were not reported for PACO. Given the low concentrations of EC observed for selected days during PACO however, the impact on the calculated percentages is likely to be small.)

	CalNex[a]	**SOAR-1[b]**	**PACO (I)[c]**	**PACO (III)[d]**
Location	**Pasadena**	**Riverside**	**Pasadena**	**Pasadena**
OA	43	45	42	55
Nitrate	22	22	15	15
Sulfate	18	17	30	16
Ammonium	13	12	13	13
Chloride	<1	<1	<1	<1
EC	3	4	N/A	N/A

[a] May 15th to Jun 16th, 2010
[b] Jul 15th to Aug 15th, 2005
[c] May 22nd to Jun 12th, 2009
[d] Jul 10th to Aug 4th, 2009

I.B. Chemical aging of sea salt and particulate charge balance

Both the CalNex XRF and PALMS measurements provide quantitative information about non-EC refractory materials including sea salt. An important detail regarding the measurement of particulate chloride is that XRF is assumed to measure refractory chloride (rCl) since the XRF samples are placed under vacuum before measurements [*Johnson et al.*, 2008]. The non-refractory and refractory chloride fractions are thought to be predominately ammonium chloride [*Salcedo et al.*, 2006] and sodium chloride (from sea salt), respectively [*Malm et al.*, 1994; *Simon et al.*, 2011]. Sodium data is not available from XRF data due to measurement limitations, but the sodium mass concentration can be estimated from PALMS sea salt volume concentrations as described in the Figure 2 caption. For fresh sea salt the expected ratio of chloride to sodium mass concentrations is 1.8 [*Finlayson-Pitts and Pitts*, 2000]. However, a ratio of 0.12 is observed for rCl to sodium at the Pasadena ground site indicating that the sodium chloride in sea salt aerosol has undergone a substantial amount of chemical processing by nitric and sulfuric acid, which depletes the amount of chloride ions in the sea salt aerosol by converting sodium chloride to sodium nitrate and sodium sulfate [*Gard et al.*, 1998]. For Pasadena, a fractional chloride depletion of 94% is calculated using the following equation described by Zhuang et al. [1999]. (In Equation 1 all concentrations are in units of moles m^{-3}.)

$$\text{Depletion} = \frac{[\text{Cl}]_{\text{original}} - [\text{Cl}]}{[\text{Cl}]_{\text{original}}} \times 100\% = \frac{1.174[\text{Na}] - [\text{Cl}]}{1.174[\text{Na}]} \times 100\% \quad (1)$$

This agrees with qualitative results from the PALMS mass spectra, which show significant displacement of chloride and accumulation of nitrate on individual sea salt particles that correlated with nitric acid concentrations.

The acidity of the particles in Pasadena can be evaluated by comparing the measured ammonium mass concentration against the amount needed to fully neutralize the measured sulfate, nitrate, and chloride, which is termed here 'NH_4^+ predicted'. Particles are considered acidic if the measured ammonium concentration is substantially lower than the predicted values [*Q Zhang et al.*, 2007a]. As seen in Figure 5A, overall the particles appear to be bulk neutralized by ammonium with a majority of the data near the one-to-one line. There are some periods though when the measured ammonium concentrations are not sufficient to neutralize the anions, especially at lower concentrations. These periods are more easily observed in the histogram shown in Figure 5B. The low ammonium measured-to-predicted ratios may be due to more acidic particles, but the PALMS instrument observed essentially zero acidic sulfate. An alternative explanation then is the presence of sodium cations that are not accounted for in Figures 5A and 5B. Typically when using AMS data to evaluate particle acidity it must be assumed that ammonium is the only significant cation, and cations from sources such as sea salt are ignored [*Aiken et al.*, 2009; *Docherty et al.*, 2011; *Q Zhang et al.*, 2007a]. For Pasadena however, sodium concentration data can be estimated from PALMS measurements providing an opportunity to evaluate the role of sea salt in particle neutralization. In Figure 5C, there is a clear dependence of the ammonium measured-to-predicted ratios on the fraction of cations that are sodium (ratios are taken from molar units), which suggests that including sodium is important when calculating the charge balance. To test this hypothesis the ratio of measured ammonium *plus* sodium to the NH_4^+ predicted is plotted in a histogram in Figure 5D. Figure 5D is close to what would be expected for particles where the sulfate, nitrate, and chloride anions are

neutralized by ammonium and sodium cations. Thus, much of the apparent particle acidity observed in Figure 5A is due to the exclusion of sodium when calculating the charge balance.

An important consideration when evaluating particle neutralization is whether the sodium cations are present as sodium nitrate or sodium chloride, and if those species can be vaporized by the AMS heater for detection. From the charge balance calculations above it appears that anions associated with sodium are detected by the AMS indicating that at least a fraction of the sodium nitrate evaporates rapidly (~1 s) in the AMS. This conclusion is supported by the strong correlation between sodium concentrations estimated from PALMS measurements and from high-resolution AMS spectra (R=0.76). It should be noted that sodium concentrations from the AMS are only a relative measurement because of surface ionization rendering the measurement unreliable [*M Canagaratna et al.*, 2007]. Moreover, the chloride depletion results and size distribution analysis discussed above indicate that a large majority of the sodium is present as sodium nitrate, which is more volatile than sodium chloride, and thus, more readily detected by the AMS, in which the vaporizer temperature was operated at approximately 600°C. Therefore, it appears that sodium cations from sea salt impact the charge balance as measured by the AMS, and also play an important role in controlling the aerosol charge balance in Pasadena, which has important implications for thermodynamic modeling of aerosols.

Docherty et al. [2011] demonstrated that for Riverside during the SOAR-1 campaign organonitrates and organosulfates also impact the charge balance calculation. These species add to the nitrate and sulfate mass measured by the AMS [*Farmer et al.*, 2010], but do not contribute the expected amount of ionic charge, which leads to apparent particle acidity. An important contrast between Pasadena and Riverside is that the deviation between measured ammonium and NH_4^+ predicted occurs at low concentrations for Pasadena, but at high concentrations for Riverside. This contrast is consistent with attributing the deviation between measured-to-predicted ammonium ratios to different causes. Organosulfates and organonitrates are present in Pasadena, but their impact on particle neutralization does not appear to be as important as in Riverside due to the relatively low concentrations for these species. This conclusion is evident when comparing the slope of the measured versus predicted plot for Riverside (0.86) against the analogous slope for Pasadena after accounting for sodium (1.00). The lower slope in Riverside is due to the presence of organosulfates and organonitrates at that location, whereas the slope of one in Pasadena indicates little influence from these species. Furthermore, the PALMS instrument measured very low amounts of isoprene-derived organosulfates in Pasadena, which further supports the relatively small role of organosulfates in this location.

Combining the discussions of size distributions and sea salt aging from above, in Figure 4B the rCl to Mg ratio is shown as function of particle size for the period of high marine influence identified in Section 3.I.A. During this period the rCl and Mg are correlated in the larger XRF size bins (R > 0.62), and thus it is assumed that Mg is predominately from sea salt, which allows for calculating the amount chloride depletion following an approach analogous to that described for sodium. (Data is not shown for smaller particle diameters since a strong correlation between rCl and Mg is not observed.) The rCl to Mg ratio is fairly constant with particle size indicating similar amounts of chloride depletion. Additionally, the average rCl to Mg ratio (2.0) corresponds to 86% chloride depletion, which is similar to 94% chloride depletion calculated using the estimated sodium data from the PALMS instrument. In general, the sea salt measured in Pasadena appears to be very aged mostly from chemical reactions with nitric acid.

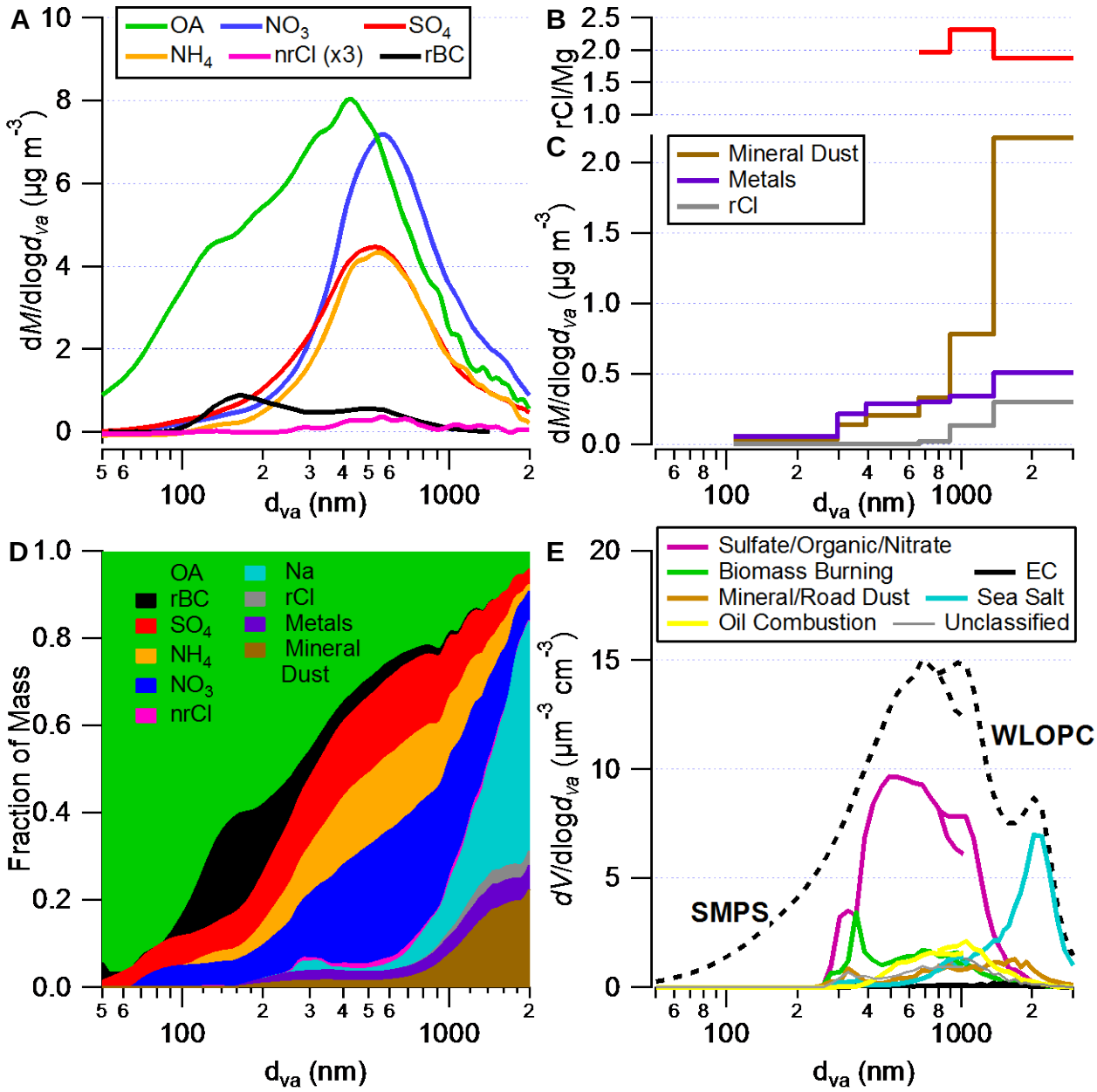

Figure 4: (A) Size distributions of the non-refractory PM measured by the AMS. Also shown is the rBC distribution measured by the SP-AMS. Note: The AMS size distributions have a gradual cut of approximately PM_1 and can have a tail due to slow evaporating particles and should be interpreted accordingly. **(B)** The ratio of rCl to Mg plotted versus particle size. Ratio is calculated using mass concentrations from XRF for the period of 5/20/2010 00:00:00 to 5/25/2010 00:00:00. **(C)** Size distribution for refractory components measured by XRF analysis. **(D)** Size distributions by percent mass. The XRF data are calculated by interpolating the original data using a cublic spline function to provide sufficient data points to create the stacked plot without reducing the resolution of the AMS and SP-AMS data. Note that rBC concentrations below 100 nm may be underestimated due to instrument limitations. Na is estimated from the PALMS data as described in Figure 2. **(E)** Size distributions of particle types measured by the PALMS instrument. Total size distributions calculated from the SMPS and WLOPC number distributions are shown. All diameters have been converted to vacuum aerodynamic (d_{va}) to compare with AMS and SP-AMS.

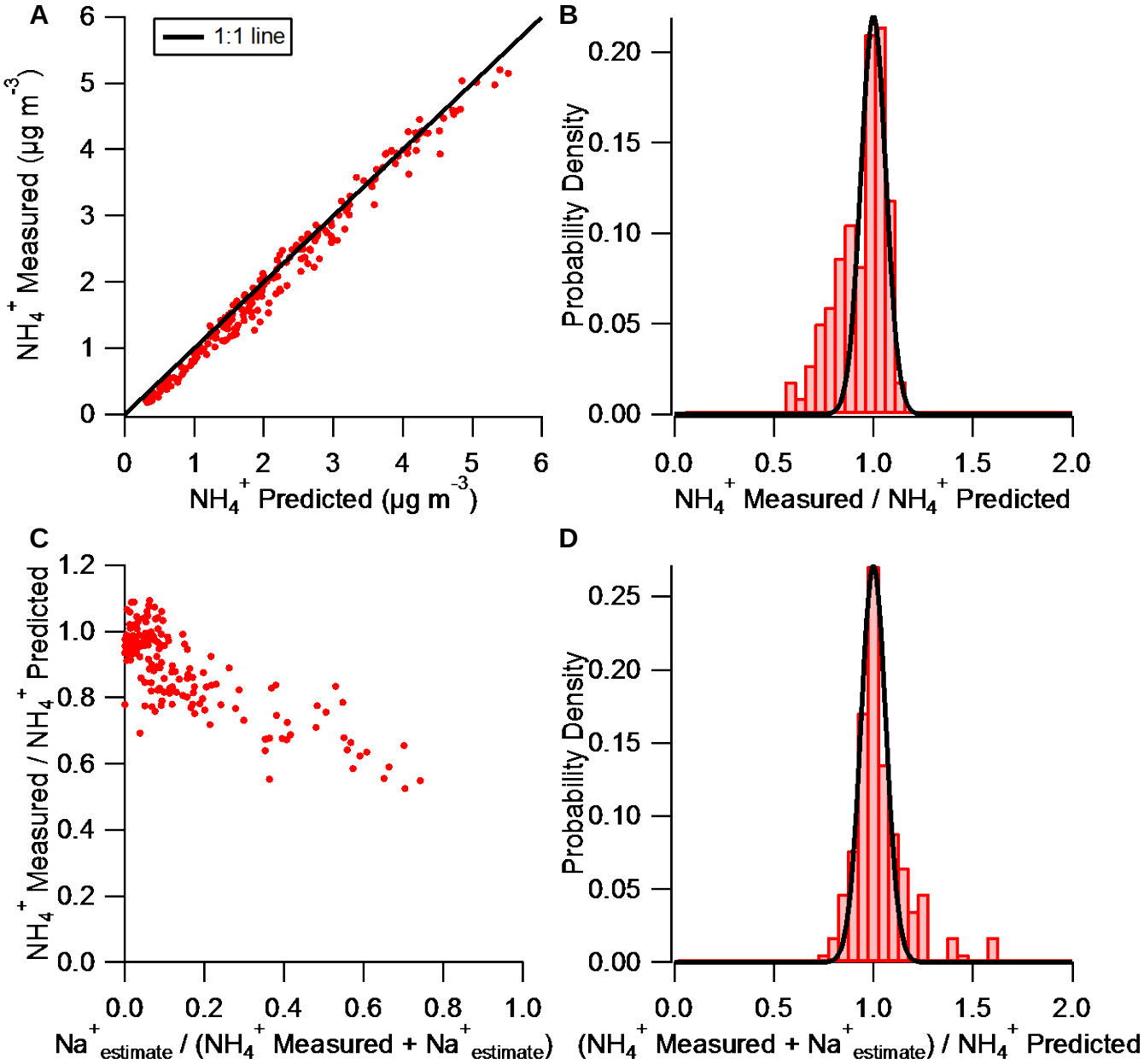

Figure 5: (A) Scatter plot of the measured ammonium versus 'NH_4^+ predicted', which is calculated using the concentrations of nitrate, sulfate, and chloride, as well as assuming full neutralization by ammonium. **(B)** Histogram for the ratios of the measured ammonium to the NH_4^+ predicted. **(C)** Scatter plot of the measured-to-predicted ratios versus the ratios of sodium to the total cations (ammonium plus sodium). Sodium is estimated from the PALMS sea salt concentrations as described in the Figure 2 caption. **(D)** Histogram for the ratio of the cationic species ammonium and sodium to the NH_4^+ predicted concentrations. Gaussian distributions are shown in the histograms for reference and are generated using the standard deviation of the data in Panel D. The mass concentrations are converted to molar units before calculating ratios, and all concentrations are PM_1.

II. Identification of OA components through Positive Matrix Factorization

II.A. PMF solution: mass spectra, time series, and diurnal averages

The PMF OA components were identified by their mass spectra, diurnal cycles, elemental composition, as well as by the concentration ratios and correlations of their time series with tracers. Figure 6 shows the mass spectra and time series for the five identified components. Additionally, Figure 7 shows the diurnal profiles of the OA components and the campaign-average fractional contribution of each component to the total OA concentration, as well as a stacked plot illustrating the fractional contributions to OA mass by time-of-day. The five PMF components identified are: (1) Hydrocarbon-like Organic Aerosol (HOA), (2) Cooking-Influenced Organic Aerosol (CIOA), (3) Local Organic Aerosol (LOA), (4) Semi-Volatile Oxygenated Organic Aerosol (SV-OOA), and (5) Low-Volatility Oxygenated Organic Aerosol (LV-OOA). The naming based on volatility is adopted according to several studies showing a relationship between high oxygenation and lower volatility for the OOA components [e.g. *Cappa and Jimenez*, 2010; *Huffman et al.*, 2009; *Jimenez et al.*, 2009; *Lanz et al.*, 2007; *Ulbrich et al.*, 2009]. The HOA component has been previously described as a surrogate for primary combustion OA, and the SV-OOA and LV-OOA components as surrogates for 'fresher' and 'aged' SOA, respectively. [*Aiken et al.*, 2008; *Jimenez et al.*, 2009; *Ulbrich et al.*, 2009; *Q Zhang et al.*, 2007b]. The identification of CIOA is consistent with previous research that has shown food cooking, which includes activities such as seed oil frying and meat charbroiling, is an important source of fine organic aerosol in urban environments [e.g. *Mohr et al.*, 2011; *Schauer et al.*, 2002b]. The precise source (or sources) of the LOA component is not known, however similar, highly variable, nitrogen-rich components have been identified in Mexico City [*Aiken et al.*, 2009], Riverside, CA [*Docherty et al.*, 2011], Crete [*Hildebrandt et al.*, 2011], and New York City [*Sun et al.*, 2011]. This component is termed 'local organic aerosol' because the LOA time series exhibits high-frequency fluctuations that indicate a relatively local source for this component. (Auto-correlation plots of the component time series are shown in Figure C-4 in Appendix C.) The LOA mass represents only a small portion of the total OA mass (5%). Still, the reoccurrence of LOA in different urban areas is an interesting finding. Additional details regarding how the PMF solution was selected are provided in Appendix C.

The mass spectra and elemental ratios of the five components displayed in Figure 6A are similar to those reported in previous studies [e.g. *Aiken et al.*, 2009; *Hersey et al.*, 2011; *Mohr et al.*, 2011]. For HOA, O:C is relatively high (0.14), but not out of the range of previously reported values. The diurnal cycle of HOA is similar to that of EC (and rBC) with a peak between 13:00 and 14:00 PDT (local time), and HOA and EC (and rBC) show high correlation (See Table 2, and Section 3.II.D below). Therefore, as discussed in Section 3.I.A for other primary emissions, it appears that a large portion of the HOA is transported to Pasadena over a period of several hours from the western LA Basin, which is consistent with the relatively high HOA oxidation. The CIOA component is more oxygenated than HOA, which is consistent with previous reports and the known presence of oxygenated compounds such as fatty acids and cholesterol in food cooking aerosol [*Mohr et al.*, 2011; *Robinson et al.*, 2006; *Sun et al.*, 2011]. The HOA and CIOA spectra are compared in detail in Appendix C. The diurnal cycle of CIOA exhibits peaks near mealtimes with a smaller peak between 14:00 and 15:00 PDT and a larger peak between 21:00 and 22:00 PDT similar to the cooking organic aerosol diurnal cycles observed for other field measurements [*Allan et al.*, 2010; *Mohr et al.*, 2011; *Sun et al.*, 2011]. The lunchtime and the

dinnertime peaks are both slightly delayed from traditional American mealtimes. The delays could be due to transport time from areas south and west of Pasadena. The delay in the dinner time peak may be also be the result of the convolution of the emission rates with the lower boundary layer in the evenings and thus reduced vertical dilution of CIOA.

Both SV-OOA and LV-OOA display higher O:C compared to the other OA components, and LV-OOA is the most oxygenated as expected for more aged SOA. The diurnal cycle of SV-OOA is very strong and peaks in the afternoon at the same time as estimated photochemical age, indicating that SV-OOA is closely linked to in-basin photochemical production of SOA. In contrast, LV-OOA does not show a strong diurnal variation on average, but the LV-OOA time series does vary substantially during the campaign measurement period. In particular, there is an increasing trend in LV-OOA concentrations during the June 2nd – June 6th period when there is evidence for recirculation of polluted air within the LA Basin impacting aerosol concentrations (see Section 3.I.A above). A build-up of LV-OOA concentrations during this period is consistent with describing this component as 'aged', since the OA is expected to be increasingly oxidized during periods of recirculation.

The mass spectrum of LOA is distinct from the other OA components and contains prominent ions that are characteristic of amines: CH_4N^+ (*m/z* 30), $C_2H_4N^+$ (*m/z* 42), $C_3H_6N^+$ (*m/z* 56), $C_3H_8N^+$ (*m/z* 58), $C_5H_{10}N^+$ (*m/z* 84), $C_5H_{12}N^+$ (*m/z* 86) [*McLafferty and Turecek*, 1993]. The large contribution of nitrogen to this factor (N:C = 0.05) is explained by the substantial presence of these ions. The contribution of LOA to the total mass for each listed amine fragment ranges from 4% for CH_4N^+ to 89% for $C_5H_{12}N^+$. Gas phase amines have a variety of biogenic and anthropogenic sources including animal husbandry, food processing, combustion, composting operations, automobiles, sewage, cooking, tobacco smoke, and pesticide application [*Ge et al.*, 2011]. As discussed later in Section 3.II.B, the correlations of LOA with other measured species (e.g. VOCs and metals) suggest that LOA sources are related to industrial or combustion processes, but the results are not conclusive.

Shown in Figure 7C is the relative contribution of each PMF component to the OA mass as a function of the total OA mass (similar to Figure 2D). A probability density of the OA mass is displayed as well (right axis). The relative OA composition is increasingly dominated by OOA, and in particular SV-OOA, during high concentration periods. As discussed previously, OA is an important contributor to the total submicron mass at all concentrations. Combining the data shown in Figures 2D and 7C, it can then be concluded that freshly formed SOA, likely from in-basin photochemical production, contributes substantially to the number of high PM_1 events.

From Figure 7D, if total OOA is taken as a surrogate for SOA, and the sum of HOA, CIOA, and LOA is taken as a surrogate for POA, then it can be concluded that SOA is dominant at the Pasadena ground site, which is consistent with earlier findings in Riverside, CA [*Docherty et al.*, 2008]. On average the total OA mass for the measurement period is composed of 66% OOA (SV-OOA + LV-OOA), and this percentage lies between that observed for a selection 'urban' and 'urban downwind' sites [*Q Zhang et al.*, 2007b].

An apparent discrepancy between combined AMS/PMF analysis and the PALMS measurements is that the latter classified 12% of the PM_1 aerosol volume as biomass burning, but the AMS does not show a significant amount of biomass burning influence as indicated by the ratio of the organic mass at *m/z* 60 to total organic mass (f_{60}) [*Cubison et al.*, 2011]. Also, a

Biomass Burning Organic Aerosol (BBOA) component is not identified in the PMF analysis, in which OA components accounting for about 5% or more of the OA mass are expected to be resolved (Ulbrich et al., 2009). Acetonitrile, a tracer for biomass burning, is generally near background concentrations (100 – 150 pptv) except for several high concentration events that are short in duration that do not correlate with the PALMS biomass burning particles, and could be related to nearby solvent use (e.g. in the Caltech campus). It is possible that potassium-containing particles from sources other than biomass burning such as meat cooking [*Hildemann et al.*, 1991; *Schauer et al.*, 1999b], which can represent a substantial fraction of the potassium in some urban regions [*Aiken et al.*, 2010; *X Zhang et al.*, 2010], may be classified as biomass burning by the PALMS algorithm due to the presence of potassium and abundant organic species. If cooking activities were the dominant source of the PALMS biomass burning particles however, then the PALMS biomass burning volume concentration would be expected to correlate with the CIOA mass concentration, which is not the case (R = -0.03). An alternative explanation is that the primary biomass burning OA mass is small, and there is a large amount of secondary mass that has condensed on the biomass burning particles. (Similarly, the primary biomass burning particles may have coagulated with secondary aerosol particles.) The particles would then be classified as biomass burning by the PALMS algorithm, but their measured volume would be significantly increased by secondary material (e.g. SOA, nitrate, sulfate, and ammonium). Finally, it is also possible that the biomass burning particles are very aged as the result of long-range transport, and due to aging they are difficult to identify with the AMS biomass burning tracers or PMF [*Cubison et al.*, 2011], although it seems unlikely that a long-range transport source could explain 12% of the submicron particulate volume in LA. (This percentage corresponds to a mass concentration of roughly 2 $\mu g\ m^{-3}$).

The approximate size distributions of HOA+CIOA, OOA, and LOA are shown in Figure 8A, along with rBC and OA. The PMF component size distributions are determined from the $C_4H_9^+$, CO_2^+, $C_3H_6N^+$ fragments measured with the AMS, which serve as tracers for POA, SOA, and LOA, respectively [*Ulbrich et al.*, 2012]. Within the OA fraction the contribution of HOA+CIOA becomes more prominent at the smallest particle sizes measured by the AMS, which is expected for aerosols directly emitted from combustion sources [*M R Canagaratna et al.*, 2004]. The organic size distribution in Figure 8A is bimodal with a peak at ~450 nm and a second mode at ~150 nm that is less distinct. The ~150 nm mode is also observed in the size distributions for rBC and HOA+CIOA, but is more prominent compared to OA. To explore this observation further, in Figure 8B the average organic size distribution for only mornings or afternoons is plotted, and in the afternoons the ~150 nm mode is relatively larger. The growth of the ~150 nm mode coincides with both the arrival of the plume from the western LA Basin and the time-of-day with the highest OOA concentrations. Therefore, it is proposed that the increase in the ~150 nm mode is due to particles that were emitted during the morning rush hour or nucleated upwind of Pasadena [*Fine et al.*, 2004], and have undergone particle growth due to condensation since OOA represents a large fraction of the OA mass in this mode. Regardless of the exact source of the ~150 nm mode particles, the lack of an inorganic mode at ~150 nm suggests that the growth of the particles in this mode is dominated by SOA. A similar finding was reported previously by Hersey et al. [2011] in Pasadena and by Ahlm et al. [2012] for Bakersfield, CA, but the additional size distributions reported here for rBC and HOA+CIOA provide further evidence that this mode is attributable to the condensation of SOA on BC/POA cores and potentially on new particles.

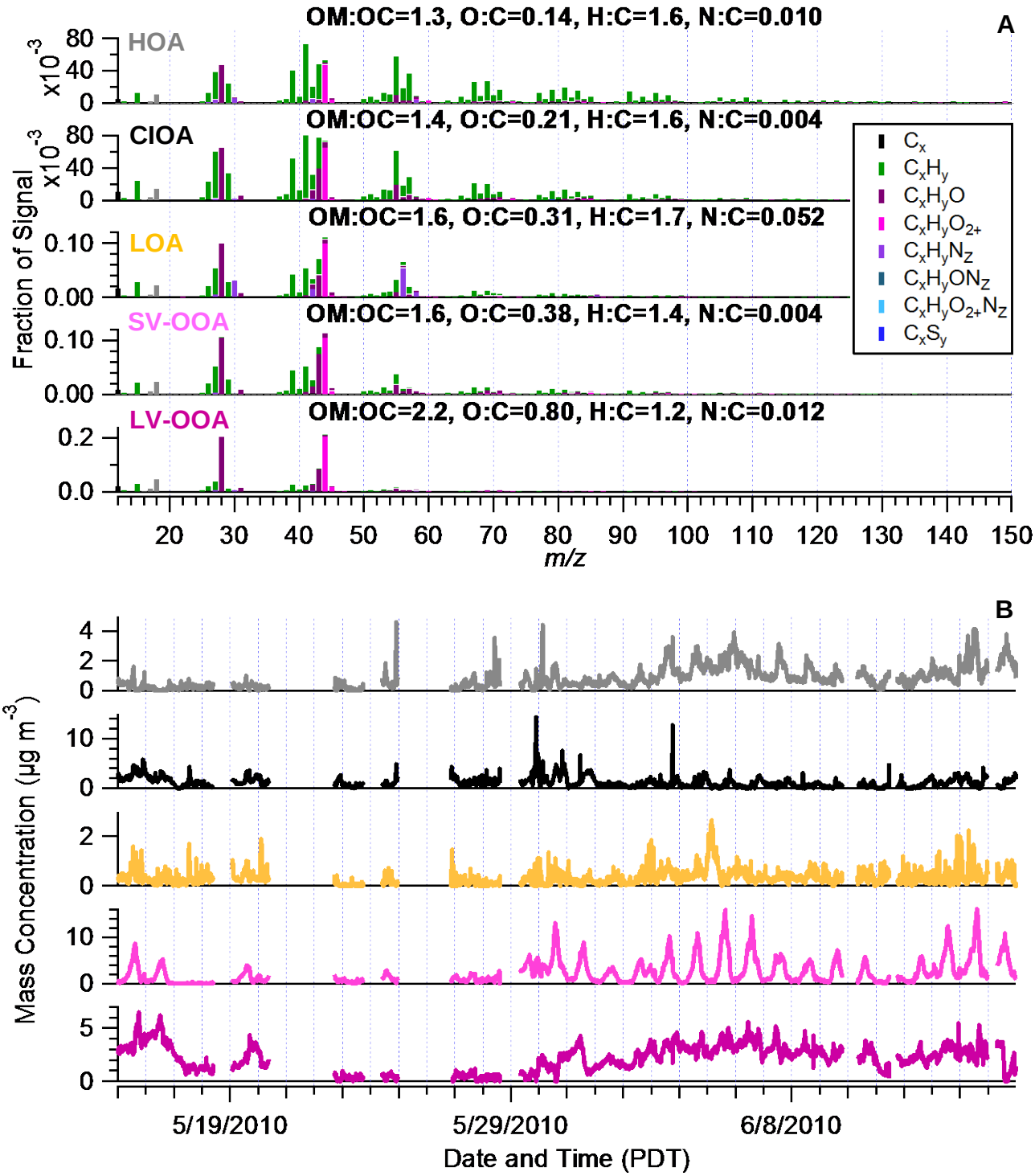

Figure 6: (A) Mass spectra for the five factors identified in the PMF analysis. The mass spectra are colored by the ion type to indicate the contribution of each ion type to the mass spectra. For clarity spectra are shown only to *m/z* 150, although spectra were measured up to *m/z* 204. **(B)** Time series of the PMF factors.

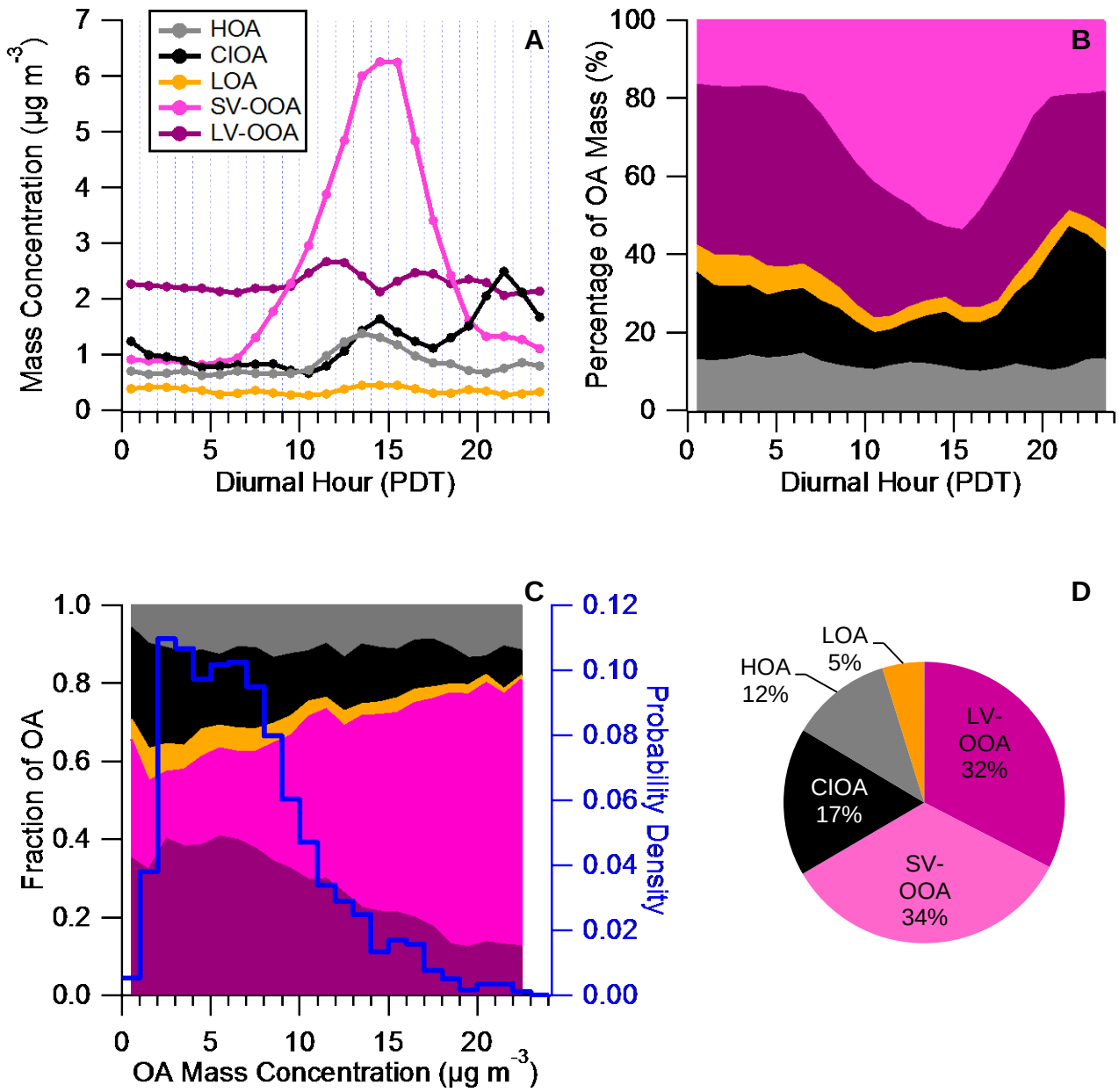

Figure 7: (A) Diurnal profiles for the PMF components. **(B)** Diurnal profiles of the PMF components by percent mass. **(C)** The fraction of the OA mass contributed by different components as a function of the total OA mass. Also shown is a histogram of the total OA mass for CalNex (blue, right axis). **(D)** The campaign average contribution of each PMF component to the PM_1 organic aerosol mass concentration.

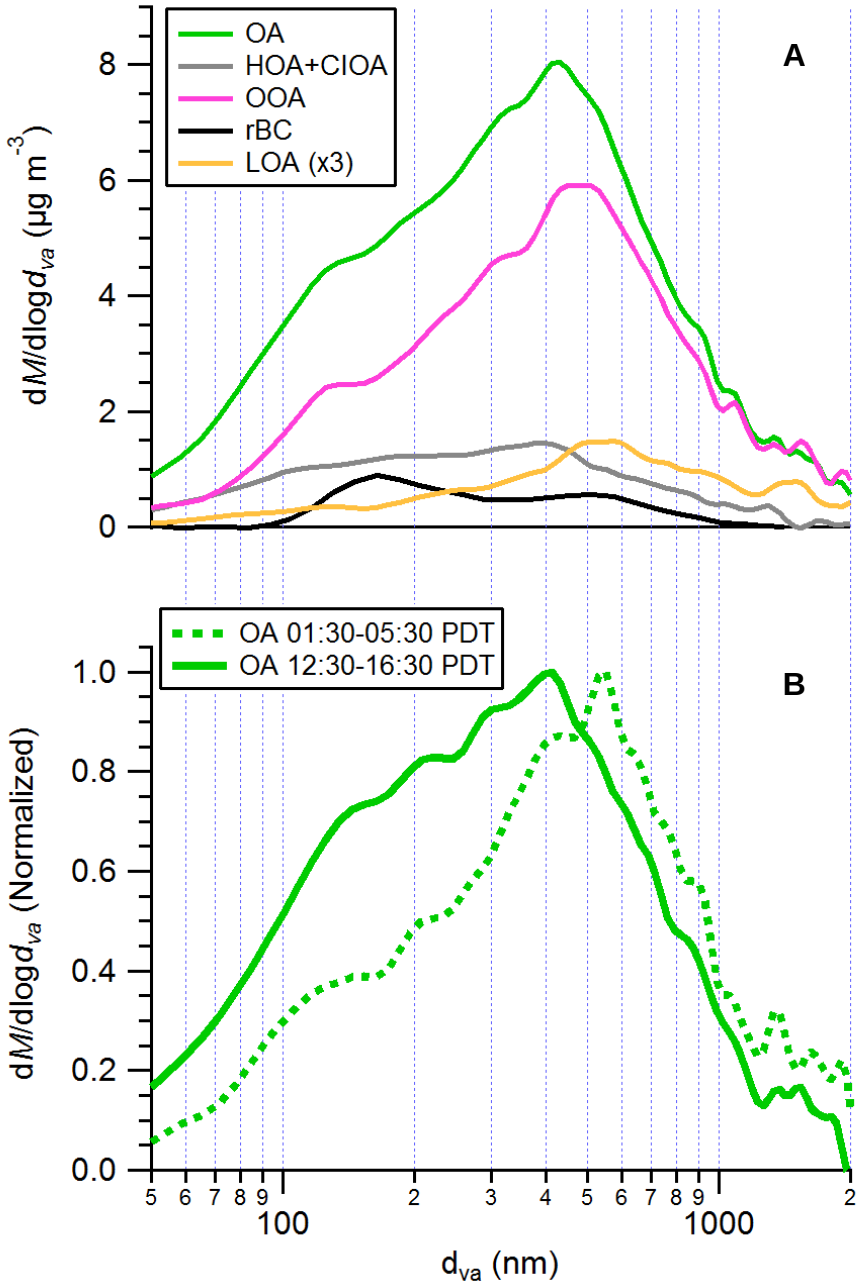

Figure 8: (A) The size distributions for OA and the components of OA. The HOA+CIOA size distribution is calculated by normalizing the $C_4H_9^+$ fragment distribution to the sum of the HOA and CIOA concentrations, the OOA size distribution is calculated by normalizing the CO_2^+ fragment distribution to the sum of the SV-OOA and LV-OOA concentrations, and the LOA size distribution is calculated by normalizing the $C_3H_6N^+$ fragment distribution to the LOA concentration. Also included is the rBC size distribution measured by SP-AMS, which is normalized to the *in-situ* Sunset Analyzer EC concentration. For rBC that is internally mixed with other compounds, the SP-AMS will measure the vacuum aerodynamic diameter of the entire ambient particle. **(B)** Average aerosol size distribution for organics during the early morning and afternoon.

II.B. Summary of correlations between PMF components and tracer species

The correlations of the PMF component time series with various other species measured at the Pasadena ground site are summarized in Table 2, and generally support the description of the components discussed above. For the readers convenience the correlations are also summarized in a bar graph in Appendix C (Figure C-5). The most notable correlations are summarized in this section. First, the primary combustion emissions tracers EC, rBC, NO_x, CO, and primary hydrocarbons correlate with HOA. A correlation is also observed between HOA and $PM_{1.15}$ Zn. The correlation with Zn may be explained by abrasion of tire-tread by road surfaces, which is thought to be a major source of Zn in urban atmospheres [*Adachi and Tainosho*, 2004; *Councell et al.*, 2004; *Hjortenkrans et al.*, 2007; *Salma and Maenhaut*, 2006], although a comparably strong correlation is not observed for other metals that have been linked to brake wear or road dust. NO_x does not exhibit as strong a correlation with HOA as the other primary combustion tracers, and this observation is probably due to the short lifetime of NO_x and the multi-hour transport time for advection of HOA from the more western portion of the LA basin to the Pasadena ground site. Moreover, NO_y correlates better with HOA than NO_x (R of 0.63 versus 0.45) likely because oxides of nitrogen emitted by vehicles have a longer atmospheric lifetime when measured as NO_y. Taken together, the correlations of the various species with HOA suggest that primary vehicular emissions are the dominant source for this component. The primary combustion tracers do not correlate with CIOA with the exception of the moderate correlation with CO (R = 0.43). The correlations of HOA and CIOA with CO, as well as the correlation of HOA with EC are discussed in further detail in section 3.II.D below. Previous work by Sun et al. [2011] reported that the AMS fragments $C_5H_8O^+$ and $C_6H_{10}O^+$ showed high correlations specific to cooking organic aerosols, and this correlation is also observed for the PMF results presented here. However, these oxygenated fragments show an even stronger correlation with SV-OOA, which suggests that these tracers are not highly specific to cooking OA.

The SV-OOA component correlates strongly with acetaldehyde and odd-oxygen. Acetaldehyde is a well-known secondary photochemical product with direct emissions that are quickly overwhelmed by secondary formation within hours of processing [*Sommariva et al.*, 2011; *Washenfelder et al.*, 2011], and odd-oxygen is a useful tracer for the oxidation of VOCs [*Herndon et al.*, 2008; *Wood et al.*, 2010]. Thus, the strong correlation of these species with SV-OOA is consistent with treating this component as a surrogate for 'fresh' SOA. Previous publications have reported a correlation between nitrate and SV-OOA at some locations [e.g. *DeCarlo et al.*, 2010; *Ulbrich et al.*, 2009], but a similar correlation is not observed at the Pasadena ground site. The lack of correlation is likely due to the higher temperatures and reduced RH in the afternoon at the ground site, which lead to the volatilization of ammonium nitrate at the same time SV-OOA concentrations are typically increasing. For LV-OOA a strong correlation with sulfate is observed that is consistent with other studies [*DeCarlo et al.*, 2010; *Sun et al.*, 2011; *Ulbrich et al.*, 2009] and has been previously attributed to the non-volatile nature of both sulfate and LV-OOA as well as the formation of these species from secondary sources. The correlation of OOA with odd-oxygen is discussed further in the next section.

$PM_{1.15}$ Ti exhibits a correlation with LOA (R = 0.63). A strong peak in LOA concentrations occurred on the morning of June 5th (PDT), and a similar event is seen in the $PM_{1.15}$ Ti time series. Paint-pigment has been identified as a source of titanium particles in the

atmosphere [*Alpert and Hopke*, 1981], but a lack of corroborating evidence prevents assigning LOA to any specific source based on this correlation.

Several other tracers are listed in Table 2. In particular, acetonitrile is a common tracer for biomass burning emissions, and a lack of correlation with acetonitrile is initially observed ($R \leq 0.1$). In contrast, after filtering out the acetonitrile data with concentrations above 1.5 ppmv to remove the possible influence of local solvent use (as discussed in the previous section), a moderately strong correlation is observed with CIOA ($R = 0.67$) despite the relatively low acetonitrile concentration that are near background levels. This correlation may be due to barbequing with biomass fuels such as charcoal. Dimethyl sulfide (DMS) and PALMS sea salt volume concentrations are indicators for marine influenced air masses [*Malm et al.*, 1994; *Zorn et al.*, 2008], but the low correlations observed between these species and all the PMF components provide little information about the role of marine sources.

In addition to the species listed in Table 2, the concentrations for a variety of organic species were quantified by 2DTAG measurements. The correlations between a selection of these species and the PMF components are summarized in Table 3. The correlations are also displayed in a bar graph in Appendix C (Figure C-6). For a variety of polycyclic aromatic hydrocarbons (PAHs), phytane, dibenzofuran, and the lowest-volatility measured Hopane the correlation with HOA is strongest, which is not surprising given that these compounds are characteristic of primary vehicle emissions [*Schauer et al.*, 1999a; 2002a; *Williams et al.*, 2010]. In addition, several ketones and undecylbenzene exhibit a higher correlation with HOA than the other PMF components, and it is known that ketones and aromatics are found in tailpipe emissions from gas and diesel vehicles [*Jakober et al.*, 2006; *Jakober et al.*, 2008]. Some species such as chrysene, a PAH, are clearly primary emissions, but show a similar level of correlation with both HOA and SV-OOA. This observation may be due to the similar time-of-day that HOA and SV-OOA concentrations peak (13:00 – 14:00 versus 14:00 – 15:00), and the lower time resolution of the 2DTAG, which averaged samples over 85 minutes. Thus, periods of high HOA and SV-OOA concentrations may appear to occur close to simultaneously on the time scale of the 2DTAG. Considering only the compounds that have the highest correlation with SV-OOA, this component tracks the concentrations of several phthalic acids and other compounds structurally similar to phthalates. This finding is consistent with the description of SV-OOA presented here since phthalic acids are well-known tracers for SOA from anthropogenic VOCs [*Williams et al.*, 2010]. In contrast, the LV-OOA component exhibits weaker correlations with 2DTAG compounds ($R < 0.5$), which is likely due to the poor transfer efficiency of highly oxidized compounds that is typical in GC systems [*Williams et al.*, 2006]. For CIOA, a weak correlation is observed with pentadecane. It should be noted that n-alkanes have been identified in emissions from meat charbroiling [*Schauer et al.*, 1999b], as well as from gasoline and diesel vehicle emissions [*Schauer et al.*, 1999a; 2002a]. Using one-dimensional TAG Williams et al. [2010] observed in Riverside that several alkanoic acids and alkylnitriles were the highest contributors to food cooking aerosols, although it is recognized that some of these compounds can have secondary sources. For CalNex, hexadecanoic acid correlates most strongly with SV-OOA rather than CIOA suggesting that secondary sources of alkanoic acids are influencing the air mass above the ground site. The alkylnitriles correlate more strongly with other PMF components than CIOA, which suggests that these compounds may not be good markers for cooking emissions in Pasadena. In general, the correlations with the 2DTAG compounds support the designations of the PMF components presented here.

Table 2: Correlations (R values) of PMF component time series with the time series of tracers measured at the Pasadena ground site during CalNex. Tracers have been grouped for clarity, and important correlations for each tracer are boldfaced and underlined. Campaign average mass concentrations for each PMF component are also shown in the second row.

Tracer	HOA	CIOA	LOA	SVOOA	LVOOA	
Campaign Avg. Conc. ($\mu g\ m^{-3}$)	0.82	1.21	0.34	2.43	2.26	
rBC	***0.70***	0.07	0.36	0.40	0.35	Primary
EC	***0.71***	0.03	0.43	0.46	0.33	Primary
NO_x	0.45	0.26	0.28	0.01	-0.07	Primary
Benzene	***0.71***	0.37	0.44	0.37	0.42	Primary
CO	***0.59***	0.43	0.41	0.49	0.41	Primary
Zn ($PM_{1.15}$)	***0.52***	-0.17	0.33	0.14	0.33	Primary
Acetonitrile[a]	0.47	***0.67***	0.47	0.03	0.48	Primary
Propane	***0.65***	0.17	0.49	0.44	0.42	Primary
n-Butane	***0.58***	0.13	0.48	0.36	0.38	Primary
Isobutane	***0.59***	0.21	0.51	0.37	0.42	Primary
n-Pentane	***0.66***	0.19	0.57	0.33	0.36	Primary
Isopentane	***0.72***	0.26	0.53	0.44	0.35	Primary
Ti ($PM_{1.15}$)	0.33	-0.08	***0.63***	0.05	0.11	Primary
NO_y	***0.63***	0.25	0.40	0.37	0.23	Primary + Secondary
O_x	0.28	0.10	0.04	***0.73***	0.17	Secondary
Acetaldehyde	0.64	0.19	0.26	***0.82***	0.39	Secondary
DMS	0.06	0.11	0.03	-0.08	-0.04	Marine
PALMS Sea Salt Vol. Conc. (PM_1)	0.17	0.08	0.04	-0.20	-0.06	Marine
Chloride	0.16	0.01	0.13	0.01	0.31	AMS
Nitrate	0.38	-0.03	0.44	0.12	***0.7***	AMS
Ammonium	0.40	0.00	0.43	0.19	***0.77***	AMS
Sulfate	0.49	0.02	0.36	0.39	***0.69***	AMS
$C_5H_8O^+$	0.58	0.47	0.23	***0.86***	0.44	AMS
$C_6H_{10}O^+$	0.56	0.60	0.24	***0.71***	0.36	AMS

[a] Correlations correspond to only acetonitrile concentrations below 1.5 ppbv to eliminate potential contributions from nearby solvent use.

Table 3: Correlations (R) of PMF components with 2DTAG compounds. The highest correlation for each tracer is boldfaced and indicated in the right-most column. 2DTAG data are only available from 6/11 - 6/16. Only compounds with R > 0.5 are shown.

2DTAG Compound	HOA	CIOA	LOA	SVOOA	LVOOA	
1H-Indene-1,3(2H)-dione	0.42	-0.05	0.06	***0.80***	0.24	SVOOA
1-Methylanthracene	***0.58***	0.41	0.26	0.46	-0.01	HOA
1-Methylphentanthrene	***0.54***	0.48	0.22	0.46	0.03	HOA
2-Methylphentanthrene	***0.56***	0.34	0.23	0.42	-0.10	HOA
2-Methylanthracene	***0.54***	0.35	0.25	0.47	0.03	HOA
2-Phenylnaphthalene	***0.58***	0.28	0.36	0.48	0.14	HOA
3-Methylphthalic Acid	0.51	0.03	0.12	***0.86***	0.20	SVOOA
4-Methylphthalic Acid	0.54	0.09	0.18	***0.81***	0.03	SVOOA
Benzophenone	0.66	0.37	0.36	***0.67***	0.43	SVOOA
Benzyl Benzoate	0.68	0.35	0.38	**0.73**	0.30	SVOOA
Chlorophthalic Acid	0.49	0.14	0.23	***0.74***	0.16	SVOOA
Chrysene	0.58	0.27	0.24	***0.61***	0.21	SVOOA
Decylbenzene	0.54	0.34	0.27	***0.58***	0.20	SVOOA
delta-Decalactone	0.47	0.05	0.12	***0.72***	0.13	SVOOA
delta-Hexadecalactone	0.53	0.20	0.28	***0.76***	0.35	SVOOA
Dibenzofuran	***0.64***	0.39	0.32	0.47	0.05	HOA
Dimethylphthalic Acids	0.53	0.03	0.13	***0.82***	0.13	SVOOA
Fluorenone	0.47	0.21	0.10	***0.57***	0.24	SVOOA
Hentriacontane	0.49	0.15	0.18	***0.61***	0.39	SVOOA
Heptadecanone	0.59	0.39	0.33	***0.64***	0.37	SVOOA
Hexadecanenitrile	0.46	0.34	0.28	***0.59***	0.47	SVOOA
Hexadecanone	0.58	0.31	0.26	***0.64***	0.31	SVOOA
Homophthalimide	0.50	-0.01	0.13	***0.84***	0.22	SVOOA
Lowest-Volatility Hopane	***0.59***	0.38	0.41	0.49	0.15	HOA
Hydroxyfluorenone	***0.54***	0.47	0.30	0.53	0.34	HOA
Isopropyl Myristate	***0.67***	0.00	0.62	0.45	0.15	HOA
Naphthalic Anhydride	0.49	0.11	0.17	***0.67***	0.17	SVOOA
Nonacosane	0.51	0.09	0.28	***0.71***	0.31	SVOOA
Nonadecanone	***0.50***	0.19	0.39	0.49	0.14	HOA
Octacosane	0.46	0.05	0.08	***0.51***	0.10	SVOOA
Octadecane	0.50	0.30	0.18	***0.51***	0.17	SVOOA
Octadecanenitrile	0.44	0.35	0.28	***0.62***	0.48	SVOOA
Octadecanone	***0.57***	0.21	0.31	0.54	0.07	HOA
Pentadecane	0.36	***0.52***	0.32	0.22	0.23	CIOA
Pentadecanone	0.52	0.37	0.38	***0.54***	0.23	SVOOA
Phenanthrene	***0.60***	0.47	0.29	0.39	-0.01	HOA
Phthalimide	0.56	0.23	0.22	***0.78***	0.36	SVOOA
Phytane	***0.59***	0.29	0.31	0.45	0.15	HOA
Tetradecanenitrile	0.55	0.23	0.48	***0.59***	0.36	SVOOA
Triacontane	0.52	0.05	0.22	***0.60***	0.25	SVOOA
Trimethylpentadecanone	***0.62***	0.22	0.39	0.59	0.36	HOA
Undecylbenzene	***0.54***	0.36	0.25	0.48	0.11	HOA

II.C. Correlation of OOA with odd-oxygen

Odd-oxygen, O_x, concentrations are closely linked to the extent of photochemical oxidation in an air mass because O_3 production results from OH reactions with VOCs and CO. Following the work of Herndon et al. [2008] and Wood et al. [2010], we examine the correlations of O_x instead of O_3 to account for the titration of O_3 by fresh NO emissions which produces NO_2. When comparing the time series of total OOA (SV-OOA + LV-OOA) versus O_x in Figure 9 similar temporal changes are observed ($R^2 = 0.53$), but the correlation is stronger during the more polluted periods of high OOA concentrations that occurred in June ($R^2 = 0.72$, for the June 2nd through 6th high pollution period). The regression slope for OOA versus O_x is 0.146 µg sm^{-3} ppbv^{-1} (Figure 9 inset). (Note: the unit 'sm' indicates that the aerosol mass concentrations have been converted to STP conditions: 273 K, 1 atm.) The data in the scatter plot is colored by time-of-day, and interestingly, the slope observed for the morning is steeper than the slope in the afternoon. This trend has also been observed in other field measurements [*Herndon et al.*, 2008; *Wood et al.*, 2010], and has been attributed to several factors including increased evaporation of SV-OOA, mixing with air aloft that contains residual OOA and O_x during boundary layer growth, and OOA production occurring on shorter timescales than O_x. The slopes of identical analyses for Riverside, CA and Mexico City are 0.142 and 0.156 µg sm^{-3} ppbv^{-1} [*Aiken et al.*, 2009; *Docherty et al.*, 2011], which are similar to the Pasadena ground site. This agreement indicates that the ratios of the SOA to O_x production rates are remarkably constant for the different sites suggesting similar SOA and O_x formation chemistries on average. As discussed by Wood et al. [2010], changes in the OOA/O_x ratio would be expected at locations where the relative concentrations of SOA and O_x precursors are different. In Houston for instance, ratios as low as 0.030 µg sm^{-3} ppbv^{-1} were found in correlation analyses during periods impacted by large petrochemical plant emissions. This observation was explained by very high concentrations of light alkenes that cause high ozone concentrations but are not expected to contribute greatly to SOA formation. Furthermore, for long-range transported air the correlation seems to be lost due to differing losses and ongoing chemistry of SOA and O_x [*Dunlea et al.*, 2009]. For LV-OOA, the diurnal cycle, time series, and highly oxidized composition all indicate this component is highly aged secondary mass. In addition, the high modern fraction of organic carbon at nighttime [*Bahreini et al.*, 2012] indicates that LV-OOA has a substantial contribution from biogenic sources. The aged and biogenic nature of this component is consistent with the lack of correlation between LV-OOA and O_x.

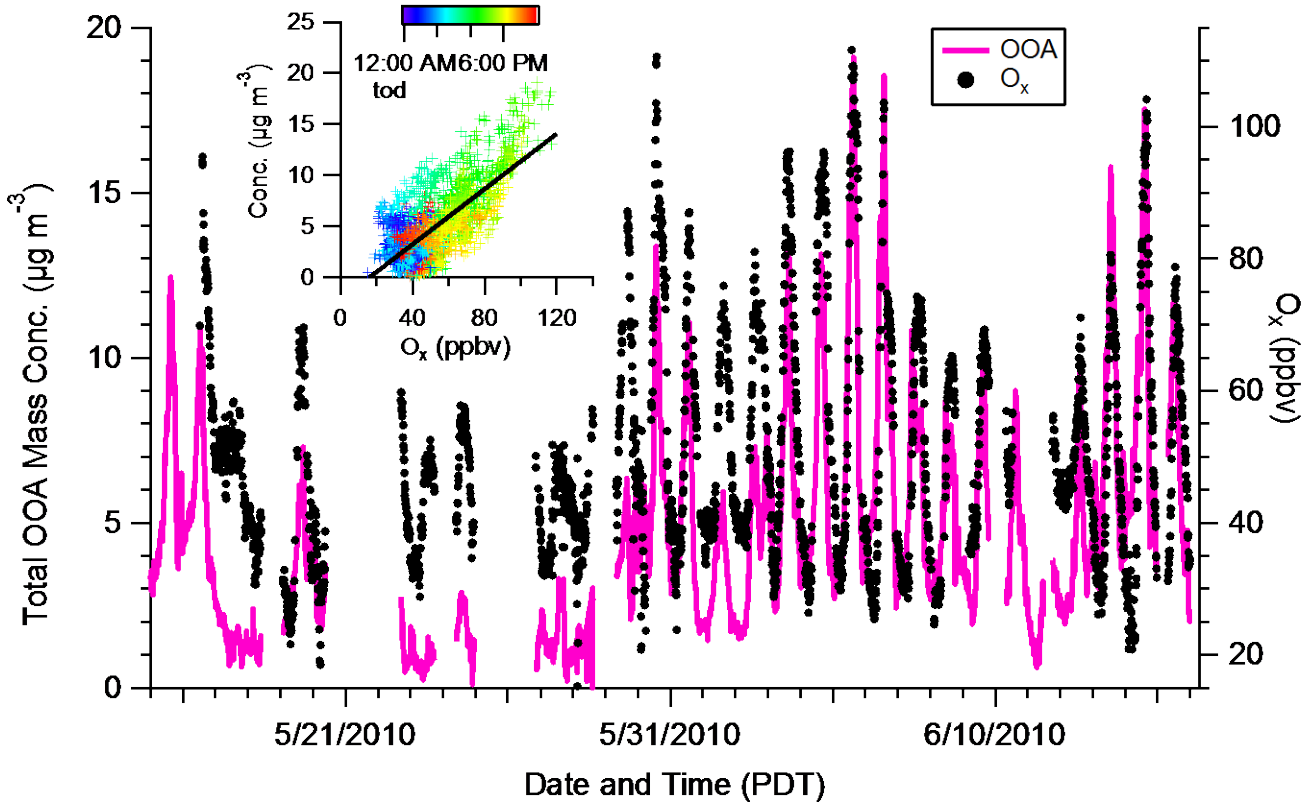

Figure 9: Time series for OOA (the sum of SV-OOA and LV-OOA), and O_x (the sum of O_3 and NO_2). **(Inset)** Scatter plot of OOA versus O_x with linear fit and colored by time-of-day. The best-fit slope is 0.146 (R^2 = 0.53). A fixed x-intercept of 15 ppbv O_x is used in the fitting procedure identical to previously published work.

II.D. HOA and CIOA: Correlations with EC and CO

As described above the HOA concentration correlates strongly with EC determined from the online Sunset analyzer (Table 2). To explore this correlation further a scatter plot of HOA versus EC mass concentration data is plotted Figure 10A. The data points in the plot are colored with the corresponding NO_y to ΔCO ratio where NO_y and ΔCO are used as qualitative indicators of diesel emissions and gasoline emissions, respectively. (ΔCO is the CO concentration enhancement over its background concentration; see Section 3.II.F below for details of how ΔCO is determined.) The ratio is not corrected for loses of nitric acid, and thus it cannot be treated as a quantitative metric. Periods with higher diesel influence are still expected to exhibit higher (NO_y/ΔCO) though [*Ban-Weiss et al.*, 2008a; *Parrish et al.*, 2007]. In addition, the grey shaded areas in Figure 10A indicate the range of POA to EC emission ratios for gasoline and diesel vehicles that were measured during summer 2006 at the Caldecott tunnel in California [*Ban-Weiss et al.*, 2008b]. The HOA to EC ratios at the Pasadena ground site overlap the range of POA to EC ratios from the Caldecott tunnel. A linear regression analysis of the Pasadena data yields a line with a slope of 1.82, which is close to the upper limit of the POA to EC ratios reported in the tunnel study. The Pasadena ratio is at times higher, but this difference could be due to the different methods used in the two studies, changes in the emission ratios of vehicles between 2006 and 2010, or the larger influence of cold starts for our dataset versus warm-running vehicles for the Caldecott tunnel. In Pasadena, for periods more influenced by diesel emissions, as indicated by high (NO_y/ΔCO), generally lower HOA to EC ratios are observed. Specifically, the best-fit slope is 1.51 for (NO_y/ΔCO) > 0.124, which corresponds to the highest 10th percentile of (NO_y/ΔCO) values. This finding is consistent with the emission ratios reported by Ban-Weiss et al. [2008b], and suggests that both diesel and gasoline vehicle emissions are contributing to the HOA mass. Accordingly, the correlation between HOA and EC improves if only periods more influenced by diesel emissions are selected for the analysis.

As also described previously in Section II.B., a correlation between HOA and CO is observed (R = 0.59). A stronger correlation is observed between CO and the sum of HOA and CIOA (R = 0.71) however. Shown in Figure 10B is a scatter plot of the CO and the HOA+CIOA data. The improved correlation when the CIOA mass concentration is added to the HOA mass concentration is surprising because cooking is not considered a major source of carbon monoxide, although it is a significant source of organic aerosol [*Allan et al.*, 2010; *CARB*, 2008; *Harley et al.*, 1997]. Emissions of CO have been measured from certain cooking activities [*Lee et al.*, 2001], but it is still a possibility that the CIOA component contains particulate mass from non-cooking sources that also emit CO (e.g. gasoline vehicles). Therefore, it is most reasonable to characterize this component as 'cooking-influenced', but not purely from cooking sources. It should be noted that different PMF solution rotations were explored using the FPeak parameter as discussed in Appendix C. There are rotations that exhibit lower correlations between CIOA and CO, but HOA+CIOA always displays a higher correlation than HOA with CO (within the constraint of not substantially diminishing the correlation between HOA and rBC). In addition, these alternative solutions exhibit lower correlations between HOA and rBC, as well as between HOA+CIOA and CO.

The data is Figure 10B is also colored by the relative amount of CIOA, so that the ratios of HOA to CO and CIOA to CO can be at least partially resolved. For periods when HOA concentrations are high (i.e. greater than 90% of the sum of HOA and CIOA) the correlation with CO is very strong (R = 0.9) and the linear slope is 6.4 μg m^{-3} $ppmv^{-1}$ when using a CO

background (x-intercept) of 105 ppbv, which is comparable to slopes found in previous studies [*Aiken et al.*, 2009]. In contrast, for periods when CIOA concentrations are high the linear slope is 13 µg m^{-3} $ppmv^{-1}$, more than twice that for HOA. The steeper slope for CIOA is indicative of significant cooking sources for CIOA that, as stated earlier, produce a larger amount of organic aerosol relative to CO [*McDonald et al.*, 2003]. A lower limit on the relative amount of CIOA mass from cooking sources can be estimated using the observation that the linear regression slope of CIOA is about twice that of HOA when the mass concentrations are plotted versus CO. Assuming that CO is overwhelmingly from vehicle emissions and no CO is emitted from cooking sources then CIOA would be 50% from cooking sources *on average* with the remainder from vehicle emissions (i.e. the additional cooking organic aerosol mass would double the mass concentration versus CO slope relative to HOA). This percentage is a lower limit because if some CO is co-emitted with cooking organic aerosol that would raise the percentage from cooking above 50%. This approach is a simplistic approximation, but the lower limit appears to be reasonable given that the diurnal cycles and spectral characteristics of CIOA are consistent with previous studies.

An alternative approach for analyzing the correlation with CO is to use a multi-linear regression instead of filtering the data for periods of high HOA or CIOA influence. For completeness, a multi-linear regression was performed and emission ratios of 8.0 and 16 µg m^{-3} $ppmv^{-1}$ were obtained for HOA and CIOA, respectively (using 105 ppbv background CO as above). This result is similar to that described in the preceding paragraph, which indicates both approaches for treating the data are robust.

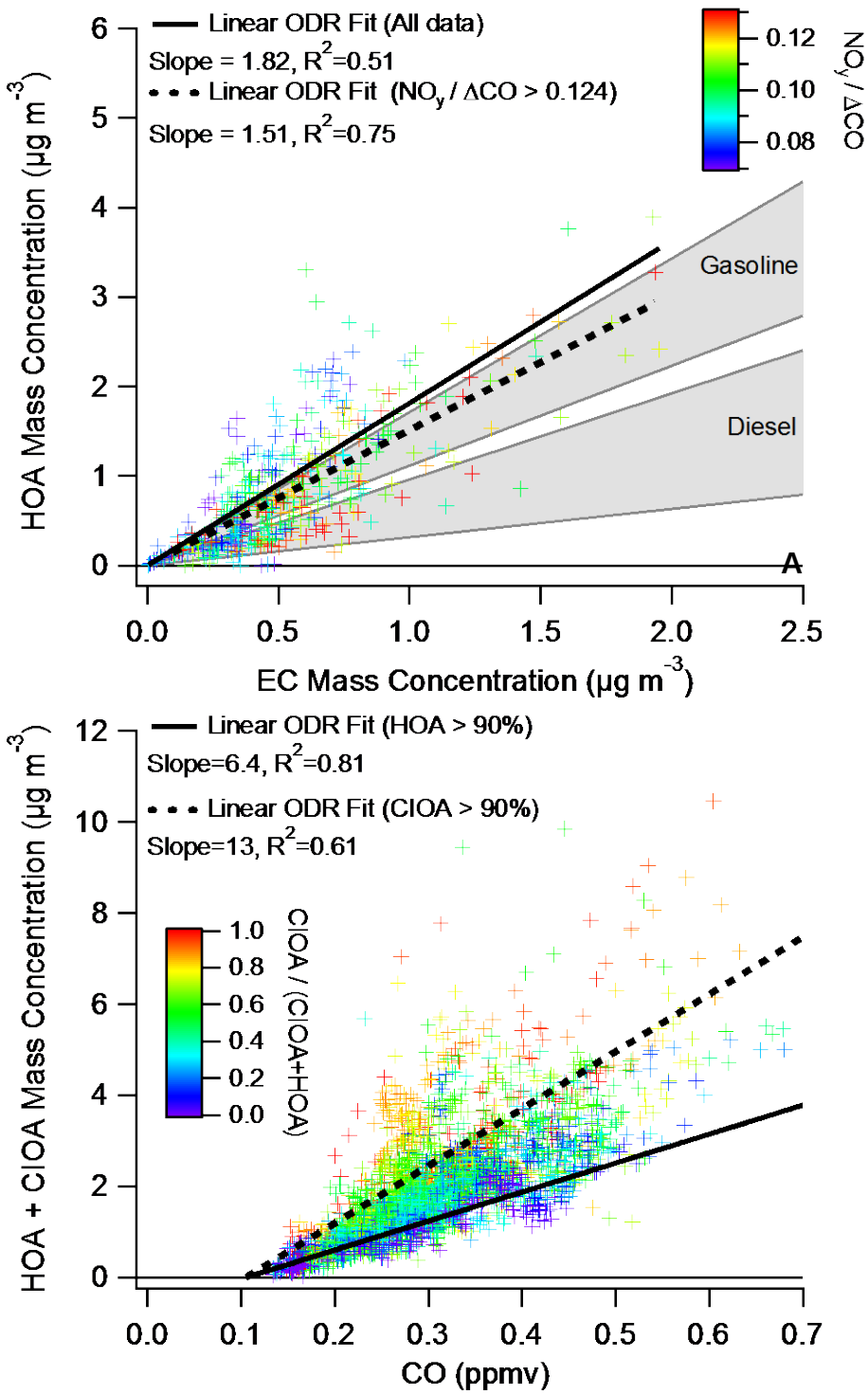

Figure 10: (A) Scatter plot of HOA vs. EC. The data is colored by $NO_y/\Delta CO$. Linear fits are shown for the entire scatter plot (solid line) and for only data corresponding to high $NO_y/\Delta CO$ (dashed line). The gray shaded regions indicate the range of expected slopes for gasoline and diesel vehicles based on emission ratios from Ban-Weiss et al. [2008b] and a 1.34 OM:OC. **(B)** Scatter plot HOA plus CIOA vs. CO. The data is colored by the relative amount of CIOA. Linear fits are shown for data corresponding to high HOA concentrations (solid line) and for data points corresponding to high CIOA concentrations (dashed line).

II.E. The weekday/weekend effect

It is well-known that in California and the Los Angeles Basin a large decrease in on-road diesel vehicle activity occurs on weekends, which leads to significant reductions in atmospheric species associated with diesel vehicles such as NO_x, EC, specific VOCs, and particulate nitrate [*Marr and Harley*, 2002; *Millstein et al.*, 2008; *Pollack et al.*, 2012]. To explore if primary organic aerosols show an analogous weekend effect in Pasadena during CalNex, the diurnal cycles for HOA, EC, rBC, CIOA, CO and benzene are plotted for weekdays and Sundays separately in Figure 11. Included in the Sunday diurnal cycle is data from the Memorial Day holiday, which occurred on a Monday and exhibited traffic patterns typical of Sundays [*Caltrans*, 2010]. Thus, the 'Sunday' diurnal cycle combines data from six days. Saturday data is not included in Figure 11 to avoid carryover effects from the preceding Friday. Carryover effects on Mondays appear to have little impact on the weekday diurnal cycle with less than a 3% change in the average daily concentrations when Mondays are omitted from averaging and no qualitative change in the diurnal cycles. Thus, Monday data are included with the other weekday data in Figure 11.

The EC (and rBC) concentration decreases on Sundays and has a very different diurnal cycle. A similar change is observed for HOA. The decrease in concentrations is consistent with the weekend effect and the importance of diesel vehicle emissions as a source for HOA and EC (and rBC). In contrast, CO and benzene concentrations when integrated over the entire day are not significantly different on Sundays versus weekdays, although their diurnal cycles are dissimilar probably due to changes in traffic patterns. Since gasoline vehicles are an important source of CO and benzene [*Fruin et al.*, 2001; *Schauer et al.*, 2002a], the lack of a weekend effect for these compounds is consistent with previous studies that demonstrated similar overall activity for gasoline vehicles on weekends compared to weekdays [*Marr and Harley*, 2002; *Pollack et al.*, 2012]. The CIOA concentrations are elevated on Sundays displaying a weekly cycle distinctly different from the other species in Figure 11. An increase in barbecuing on weekends has been reported previously for the Los Angeles Basin [*Chinkin et al.*, 2003], which is consistent with elevated CIOA concentrations on weekends. However, given the limited corroborating evidence and lack of previous long term observations of cooking emissions (to our knowledge), further studies are needed to make a confident conclusion regarding the weekly variations in cooking organic aerosol.

The observed decreases in HOA and EC concentrations on Sundays can be compared against the expected decreases in their emissions, estimated from a combination of data on fuel sales [*BOE*, 2011], emission ratios [*Ban-Weiss et al.*, 2008b], and traffic volume [*Caltrans*, 2010]. The first step to obtain the estimates is calculating the percentage of weekday EC and HOA attributable to diesel emissions using Equation 2 below.

$$\frac{\mathrm{EC_{Diesel}}}{\mathrm{EC_{Total}}} = \frac{\mathrm{ER_{Diesel}} \times \mathrm{FS_{Diesel}}}{(\mathrm{ER_{Diesel}} \times \mathrm{FS_{Diesel}}) + (\mathrm{ER_{Gas}} \times \mathrm{FS_{Gas}})} \qquad (2)$$

In Equation 2, *ER* is the emission ratio for diesel and gasoline vehicles taken from Ban-Weiss et al. [2008b], and *FS* is the gasoline and diesel fuel sales reported for the State of California during May and June 2010 [*BOE*, 2011]. An analogous equation is used for HOA. The *ER* is defined as the amount of EC (or HOA) emitted per unit fuel burned, and the values used in this work are: 0.022 (gasoline EC), 0.86 (diesel EC), 0.031 (gasoline HOA), 0.41 (diesel HOA) g kg^{-1} fuel. For this analysis we have assumed the POA *ER* is equivalent to HOA *ER*, which follows from the

observation that HOA is dominated by primary combustion sources as discussed in Section II.D above. It also is assumed that the monthly fuel sales are representative of weekday fuel use in the Los Angeles Basin. Following this method it is estimated that diesel emissions account for 87(±3)% of EC and 70(±10)% of HOA. The second step utilizes daily vehicle miles traveled (VMT) data for Los Angeles County to calculate that during the campaign truck traffic decreased 44% on Sundays relative to weekdays [*Caltrans*, 2010]. This figure lies within the range of other estimates for weekend reductions of heavy-duty vehicle traffic [*Chinkin et al.*, 2003]. Finally, an estimate of EC concentrations on Sunday relative to weekdays, ΔEC_{sun} (%), can be calculated as follows (an analogous equation can be used for HOA).

$$\Delta \mathrm{EC}_{\mathrm{Sun}} = \frac{\mathrm{EC}_{\mathrm{Diesel}}}{\mathrm{EC}_{\mathrm{Total}}} \times \frac{(\mathrm{Truck\ VMT})_{\mathrm{Sun}}}{(\mathrm{Truck\ VMT})_{\mathrm{WD}}} + \frac{\mathrm{EC}_{\mathrm{gas}}}{\mathrm{EC}_{\mathrm{Total}}} \times \frac{(\mathrm{Non\text{-}Truck\ VMT})_{\mathrm{Sun}}}{(\mathrm{Non\text{-}Truck\ VMT})_{\mathrm{WD}}} \quad (3)$$

Using Equation 3 the Sunday concentrations of EC and HOA are estimated to be 62(±1)% and 69(±4)% of their weekday concentrations, respectively. To estimate these values the non-truck VMT on Sundays versus weekdays was taken to be equal because of the similarity in the average daily CO and benzene concentrations. For comparison, the observed average Sunday EC and HOA concentrations at the Pasadena ground site are 71% and 82% of the weekday averages, respectively. The agreement between the estimated and observed values is good, given the need for several approximations to obtain the estimate. The reduction in HOA is less than the reduction in EC for both the estimated and the observed values, due to the greater portion of HOA emitted from gasoline vehicles. Lastly, it is noted that in contrast to HOA, the CIOA concentration is higher on Sundays as discussed above, and the combination of the two opposite trends leads to a net increase of POA on the weekends.

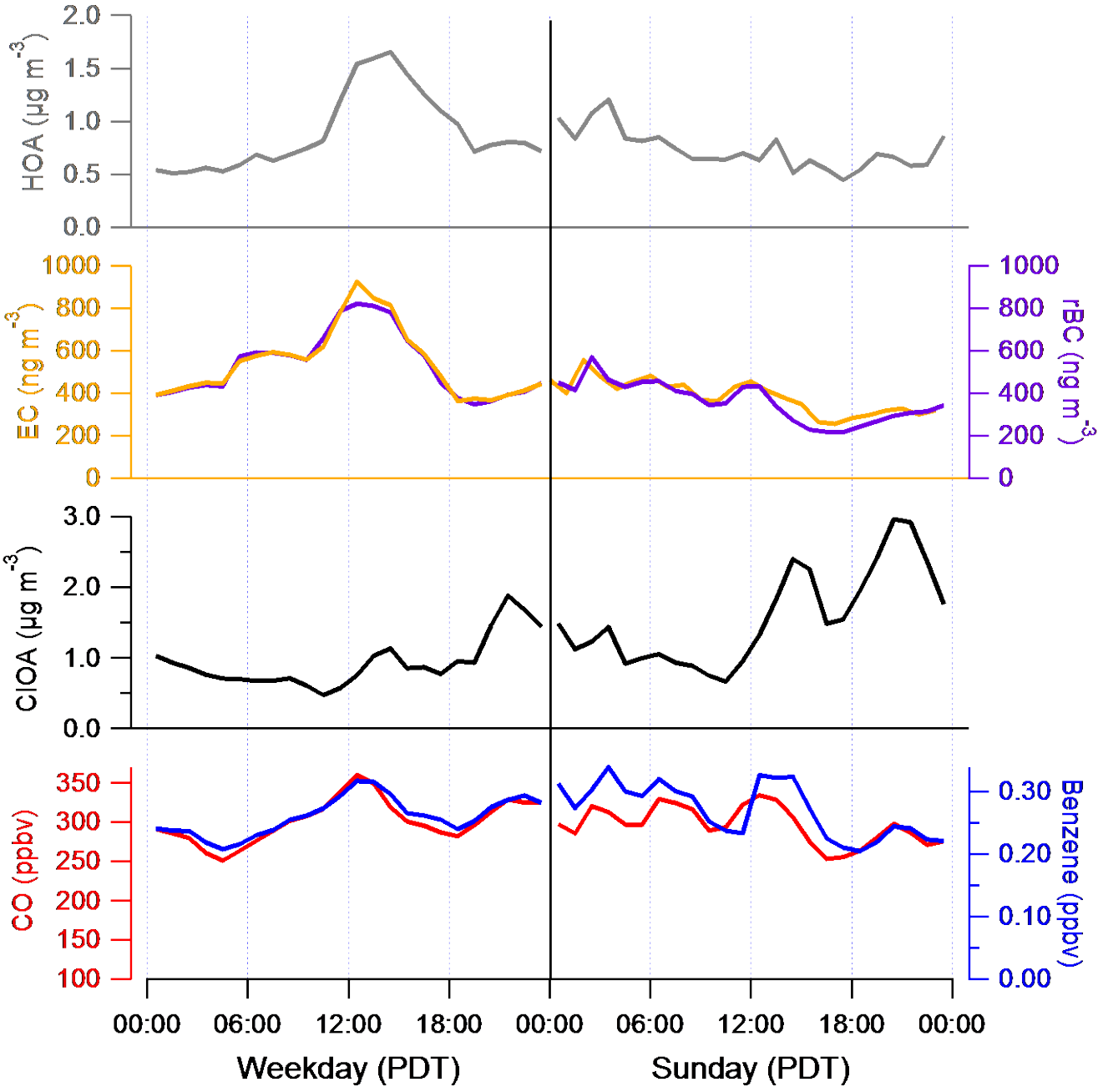

Figure 11: Diurnal profiles, calculated using means, of HOA, EC, rBC, CIOA, CO, and Benzene for weekdays and Sundays during CalNex.

II.F. Ratio of OA to carbon monoxide enhancement

To evaluate if the timescales and efficiency of SOA formation observed in Pasadena are similar to other urban regions the evolution of (OA/ΔCO) as a function of photochemical age is plotted in Figure 12, where ΔCO is the CO concentration enhancement over its background concentration. The background CO is estimated to be between 85 – 125 ppbv using CO measurements taken aboard the NOAA WP-3D aircraft off the LA coastline at altitudes less than 200 m (Latitude range: 32 to 35, Longitude range: -117 to -120). A concentration of 102 ppbv was the minimum observed and concentrations below 110 ppbv were regularly observed. Accordingly, the background CO was taken to be 105 ppb when calculating (OA/ΔCO), and the error bars in Figure 12 represent the variability in the data if the background CO is taken to be either 85 or 125 ppb. Given the observed CO values off the LA coastline this range represents a conservative estimate of the uncertainty in background CO. The photochemical age for the air mass over the Pasadena site was calculated with two different methods. First, using the ratio of 1,2,4-trimethylbenzene to benzene, as described in Parrish et al. [2007]. Second, by defining the photochemical age as $-\log_{10}(NO_x/NO_y)$ similar to Kleinman et al. [2008]. All photochemical ages were calculated using a standard OH radical concentration of 1.5×10^6 molecules cm^{-3}. For reference, the daily OH radical concentrations averaged for the whole campaign at the Pasadena site were 1.3×10^6 molecules cm^{-3}. The two photochemical age calculations give virtually identical results despite the high deposition velocity of nitric acid. The match is therefore consistent with the short photochemical ages determined. It also suggests that recirculation of aged air masses is not significantly perturbing the photochemical age calculation due to the deposition of nitric acid. The grey region in Figure 12 represents (OA/ΔCO) versus photochemical age observations from previous campaigns in Mexico City and the northeastern United States as summarized by DeCarlo et al. [2010]. The CO enhancement is assumed to be a conservative tracer of urban combustion emissions that are also the source of aerosols and aerosol precursors, and thus, normalizing the OA concentration to CO will remove the effect of dilution. Photochemical formation of CO from VOCs or destruction of CO by OH reaction were estimated to perturb CO concentrations minimally over these time and spatial scales [*Griffin et al.*, 2007]. All the data sets display an increase in the OA/ΔCO ratios with photochemical age due to secondary organic aerosol formation. The Pasadena OA/ΔCO versus photochemical age plot follows the upper limit of the range of previously reported values, although the differences should not be over interpreted given the uncertainties associated with the background CO determination (indicated by the error bars) and the photochemical age calculations. The photochemical age uncertainty has been discussed extensively in previous papers and is due to, in part, the presence of mixed sources with different emission profiles and spatial distributions [e.g. *Kleinman et al.*, 2007; *Parrish et al.*, 2007]. Thus, it appears that SOA production per unit CO is similar or slightly more efficient in the Los Angeles Basin compared to the other locations. This observation suggests that similar precursors are responsible for SOA production at these locations and they are emitted proportionally to CO. Recent results from CalNex indicated that gasoline vehicle emissions may be responsible for a large fraction of the SOA production, and gasoline vehicles are also thought to be the major source of CO in these urban areas [*Bahreini et al.*, 2012]. The association of SOA precursors and CO with a common source would explain the similar evolution of OA/ΔCO with photochemical age observed at the different locations.

The observed long-term decrease of CO concentrations in the United States [*Parrish et al.*, 2002] could potentially influence OA/ΔCO values, but there is evidence that SOA precursors

have decreased in proportion to CO in the LA Basin and thus changes in OA/ΔCO due to CO reductions may not occur. The enhancement ratios of aromatic, alkyne, and alkene VOCs with CO (ΔVOC/ΔCO) have remained constant between 2002 and 2010, as has the ratio for acetaldehyde [Warneke et al., submitted manuscript, 2012], a species that correlates strongly with OOA (R=0.81) and is dominated by secondary sources after sufficient photochemical processing of emissions. The similarity of OA/ΔCO values described here for campaigns spanning several years is consistent with the lack of change in ΔVOC/ΔCO. Two caveats should be highlighted though. First, there may be unidentified SOA precursors that are not decreasing in proportion to CO. As an example the ΔVOC/ΔCO for the lighter alkanes increased for the LA basin, although these species are not expected to contribute substantially to SOA formation. Second, it is uncertain if the constancy of ΔVOC/ΔCO holds true for other locations outside the LA basin including the northeastern United States and Mexico City.

Marked in Figure 12 is the sum of HOA, CIOA, and background LV-OOA ($LVOOA_{PCA=0}$) divided by CO. The ratio of HOA+CIOA to CO is determined from the linear regression analysis of the data in Figure 10B, and the background LV-OOA to CO ratio is the average of LV-OOA divided by CO at photochemical ages less than 0.05 days (Figure 13). Several explanations are possible for the source of background LV-OOA. First, some very aged SOA may be present due to recirculation in the LA basin, for which the photochemical tracers have mostly decayed away. A second plausible explanation is 'dark' SOA production from ozone or nitrate radicals that will react with alkenes and PAHs. An important piece of evidence to support this possibility would be an increase in OA/ΔCO at low photochemical ages as the time-of-day approached sunrise, since the increase in morning traffic would lead to fresh emissions that decrease photochemical age and react with ozone or nitrate radical. This phenomenon is not observed however, which indicates that 'dark' SOA is not an important source of the background LV-OOA, consistent with the expected minor contribution of alkenes to SOA in urban areas [*Dzepina et al.*, 2009; *Wood et al.*, 2010]. A third explanation is the influence of a non-combustion source (or sources) that emits SOA precursors but relatively small amounts of 1,2,4-trimethylbenzene, benzene, and NO_x, as well as CO. If the air mass above Pasadena was influenced by such a source an increase in OA/ΔCO would be observed, but the photochemical age as measured by the ratio of (1,2,4-trimethylbenzne/benzene) or (NO_x/NO_y) would not be significantly altered. Thus, a regional biogenic SOA source could explain the background LV-OOA observed in Pasadena at low photochemical ages since biogenic sources exhibit the necessary properties described here. Back-trajectories for air reaching Pasadena during CalNex often travel over the coastal California mountain ranges where biogenic VOC emissions are large (see Figures A-3 through A-5 in Appendix A). Biogenic SOA also has been associated with high OA/ΔCO ratios [*Slowik et al.*, 2010]. Further investigation including regional SOA modeling is required though before the influence of biogenic sources on the OA/ΔCO ratio can be clearly determined. An alternative source which also has the necessary properties listed here is marine OA. However the very low OA concentrations, less than 0.2 μg m^{-3}, over the open ocean west of California for periods with low pollution influence [P. K. Quinn, NOAA, personal communication, 2012] make this possibility unlikely. In addition, low marine OA concentrations, 0.5 μg m^{-3}, have been measured by an AMS in La Jolla, CA (located on the California coast 170 km southeast of Pasadena) [*Liu et al.*, 2011], which is an amount similar to other marine studies [*Russell et al.*, 2010] and is not sufficient mass to explain the background LV-OOA.

Figure 13A shows the OA/ΔCO versus photochemical age plot corresponding to weekdays, Saturdays, and Sundays. Also shown is the analogous plot for total OOA (Figure 13B) and SV-OOA (Figure 13C). The plots are similar on weekdays versus Sundays, which is in agreement with recent results from Bahreini et al. [2012], although in this previous work PMF results were not available for separating the contribution of HOA and OOA. The average ratio of weekday to Sunday OOA/ΔCO determined for Pasadena is 1.1 (±0.1), and thus, no weekly cycle is observed within experimental uncertainties. This ratio is determined by binning the data according to photochemical age, then performing orthogonal distance regressions on both the weekday and Sunday data, and dividing the resulting slopes. (Note: the linear fits were weighted by the standard errors of the mean OOA/ΔCO and mean photochemical age.) The findings reported here are consistent with the conclusion reported by Bahreini et al. [2012] that gasoline emissions are substantially more important than diesel emissions in the formation of secondary organic aerosol mass within the LA Basin, since a large decrease in the OOA/ΔCO ratio is not observed on weekends when there is less diesel traffic. Following the method described by Bahreini et al. [2012], and using a 44% decrease in diesel traffic on Sundays as determined above, it is estimated that precursors from diesel emissions account for 0 – 35% of SOA mass. Also, a consistently higher photochemical age is observed on Sunday versus weekdays due to the higher oxidant concentrations resulting from reduced NO_x emissions. These results are in good agreement with the other CalNex papers that address weekday/weekend effects [*Bahreini et al.*, 2012; *Pollack et al.*, 2012].

In Figure 13D, the organic mass to ΔCO ratio is plotted for each PMF component. The ratio increases for SV-OOA and LV-OOA with photochemical age consistent with both components being dominated by secondary sources. In contrast, the ratios for HOA, CIOA, and LOA do not vary substantially with photochemical age, which strongly supports that these three components are dominated by primary sources.

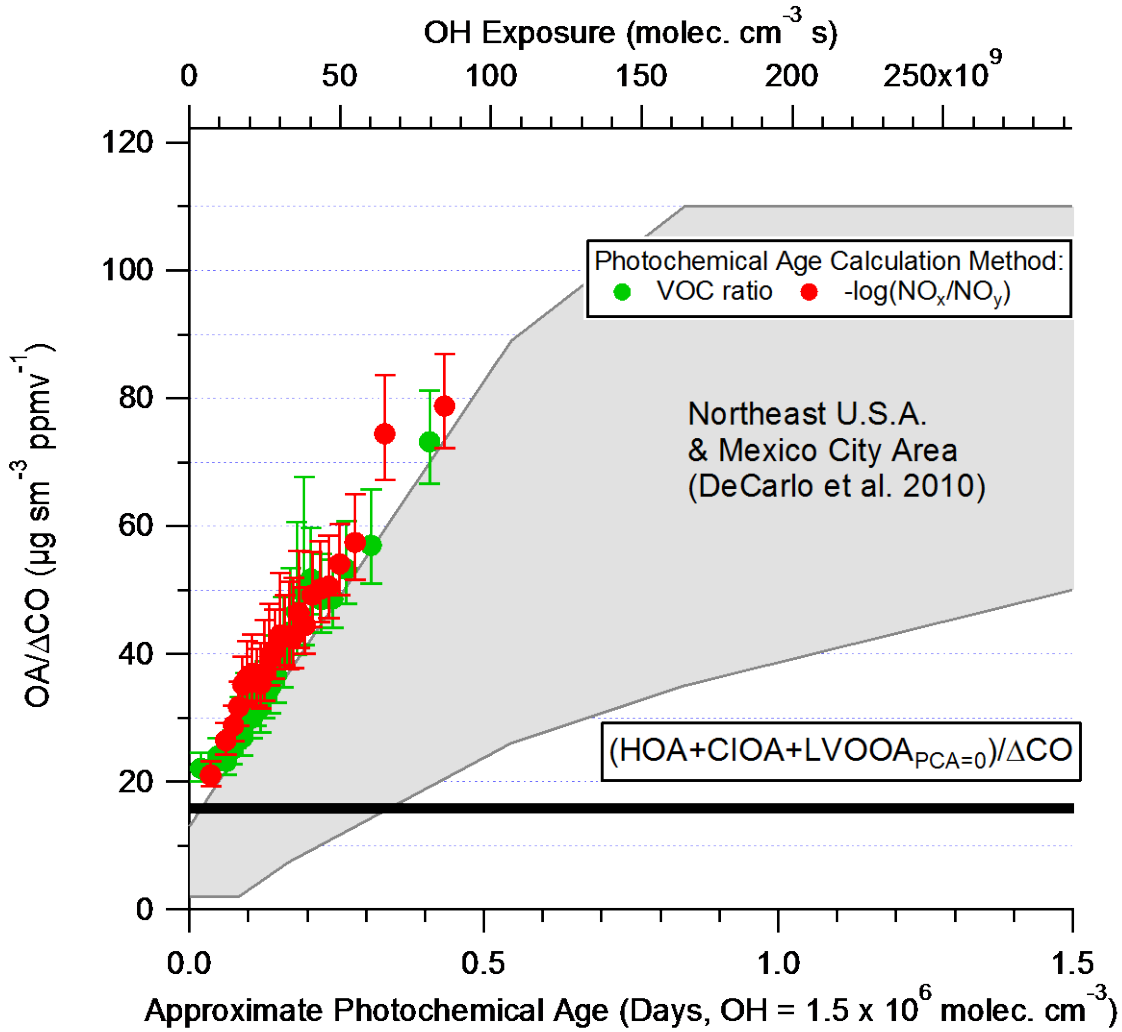

Figure 12: The evolution of OA/ΔCO versus photochemical age for Pasadena during CalNex. The measured ratios are averaged into 25 bins according to photochemical age. The enhanced CO (ΔCO) is the ambient CO minus the estimated background CO (105 ppb). The standard error of OA/ΔCO is smaller than the size of the data point, and therefore is not plotted. Instead error bars representing the uncertainty in the ratio due to an uncertainty of ±20 ppbv in background CO are shown. Photochemical age is determined by two methods: (1) Following Parrish et al. [2007] and using the ratio of 1,2,4-trimethylbenzene to benzene (green); (2) Following Kleinman et al. [2008] and defining the photochemical age as $-\log_{10}(NO_x/NO_y)$ (red). All photochemical ages have been standardized to an OH radical concentration 1.5 x 10^6 molec. cm^{-3}, and the corresponding OH exposure for a given photochemical age is shown on the top axis. The gray region is adapted from DeCarlo et al. [2010] and represents the evolution of OA/ΔCO observed in the northeastern United States and the Mexico City area. The black horizontal line is the ratio of (HOA + CIOA + 'background LVOOA') to ΔCO.

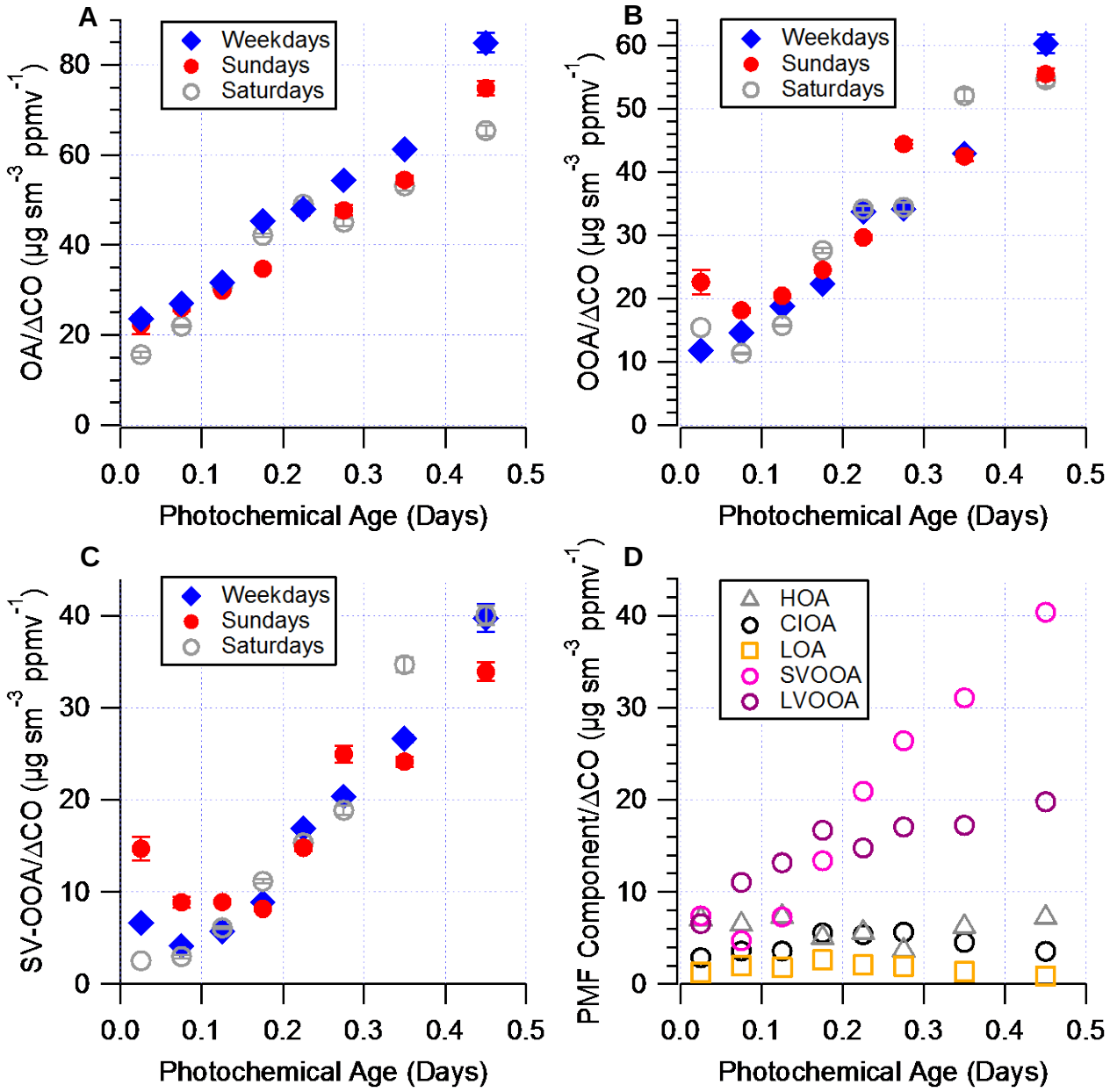

Figure 13: (A) The evolution of OA/ΔCO versus photochemical age for Pasadena during CalNex separated by day of the week. The enhanced CO (ΔCO) is the ambient CO minus the estimated background CO (105 ppb). Error bars indicate the standard errors. Photochemical age is determined using the method of Parrish et al. [2007]. Also shown are the analogous plots for **(B)** OOA and **(C)** SV-OOA. **(D)** Evolution of the PMF component concentrations normalized to ΔCO versus photochemical age.

II.G. OA elemental composition and Van Krevelen diagrams for Pasadena and Riverside

High resolution mass spectra from the AMS were analyzed to obtain bulk H:C and O:C values for OA at the Pasadena ground site. Similar data have been reported previously for the SOAR-1 campaign in Riverside, CA [*Heald et al.*, 2010]. The data for both campaigns is plotted in a Van Krevelen diagram (H:C versus O:C) along with the corresponding linear regression analyses and PMF components for the two data sets (Figure 14). The slope of the Van Krevelen diagram for bulk OA is different when comparing the data from Pasadena and Riverside. The regression analysis for Pasadena results in a best-fit slope of –0.64 whereas a slope of –1.1 is obtained for Riverside. As discussed below the differences in the evolution of H:C versus O:C for the bulk OA measured at the two sites can be attributed to the relative oxidation of HOA when it is mixed with other aerosol.

While the Van Krevelen diagram was originally developed to illustrate the chemical maturation of coal, recent work by Heald et al. [2010] demonstrated it is also a useful tool for interpreting the evolution of organic aerosols in the atmosphere. Within the Van Krevelen diagram the most oxidized species lie at the lower right, and different oxidation reactions fall along individual straight lines. For instance, oxidation of a methylene group (–CH_2–) to a carbonyl group (–C(=O)–) corresponds to a slope of –2, oxidation of a methylene to an alcohol (–C(–OH)–) group corresponds to a slope of zero, and fragmentation of a methylene chain to produce two carboxylic acid groups corresponds to a –½ slope. Numerous other reactions or combinations of reactions relevant to OA may lead to a variety of slopes in the Van Krevelen diagram, which makes attributing a particular slope to a specific chemical reaction difficult in the case of ambient field measurements. Despite this complexity the Van Krevelen diagram is still useful for constraining the reactions that are responsible for chemical aging of OA, and for comparing results from laboratory and field studies.

The slope for Riverside is consistent with the work of Heald et al. [2010], which reported that for OA from a variety of environments H:C versus O:C plots generally follow a line with a slope of –1. However, Ng et al. [2011] recently showed that deconvolving OA into HOA and OOA components allows for examination of the aging of OOA without the influence of HOA and OOA mixing on the H:C and O:C ratios. Ng et al. also demonstrated that the OOA components from a variety of studies generally follow a slope of –0.5 instead of the steeper slope described by Heald et al. [2010] for total bulk OA. For Pasadena and Riverside the SV-OOA and LV-OOA components correspond to a best-fit line with a slope of –0.55 similar to the slope found by Ng et al. [2011]. Thus, the composition and chemical evolution of OOA in Pasadena and Riverside are similar within this analysis, and do not appear to be driving the difference in slopes for bulk OA in the Van Krevelen diagram. The composition of the HOA measured at the two locations is dissimilar, however. The HOA in Riverside exhibits a very low O:C ratio (0.02), while in Pasadena HOA is more oxidized with an O:C ratio of 0.14. It is proposed that the difference in slopes for Riverside versus Pasadena in the Van Krevelen diagram is due to the physical mixing of HOA with differing oxygen content into an air mass already containing OOA. In other words, the mixing of less oxidized HOA with OOA in Riverside may explain the steeper slope observed in that location, but in Pasadena the more oxidized HOA will not influence the slope as strongly when mixing occurs because the Pasadena HOA falls near the line defined by the two Pasadena OOA components in the Van Krevelen diagram. Similar logic applies for the CIOA component at the Pasadena site as well. Based on the diurnal cycles of HOA for the two sites, it seems that that the Pasadena HOA is more oxidized because it has undergone more

photochemical aging relative to the Riverside HOA. In Riverside, the HOA concentration peaks in the morning as expected for fresh emissions from the local morning rush hour traffic, consistent with the location of the Riverside site downwind and nearby large highways. In contrast, in Pasadena the HOA concentration peaks around 13:30 due to advection over several hours from other regions in the LA Basin.

It was also observed by Ng et al. [2011] that HOA components occupy a different space of the Van Krevelen diagram relative to OOA and display variability that can be approximated by a line with a –2 slope. The HOA components for Riverside and Pasadena shown in the Van Krevelen diagram presented here follow a similar line, which is indicative of HOA aging. As described already, a slope of –2 is consistent with functionalization of a methylene chain with carbonyls. For Pasadena, the HOA component also correlated with several ketones (see 2DTAG data discussed in Section 3.II.B), which provides further evidence that carbonyl groups may be an important oxygen-containing functional group for more oxidized HOA.

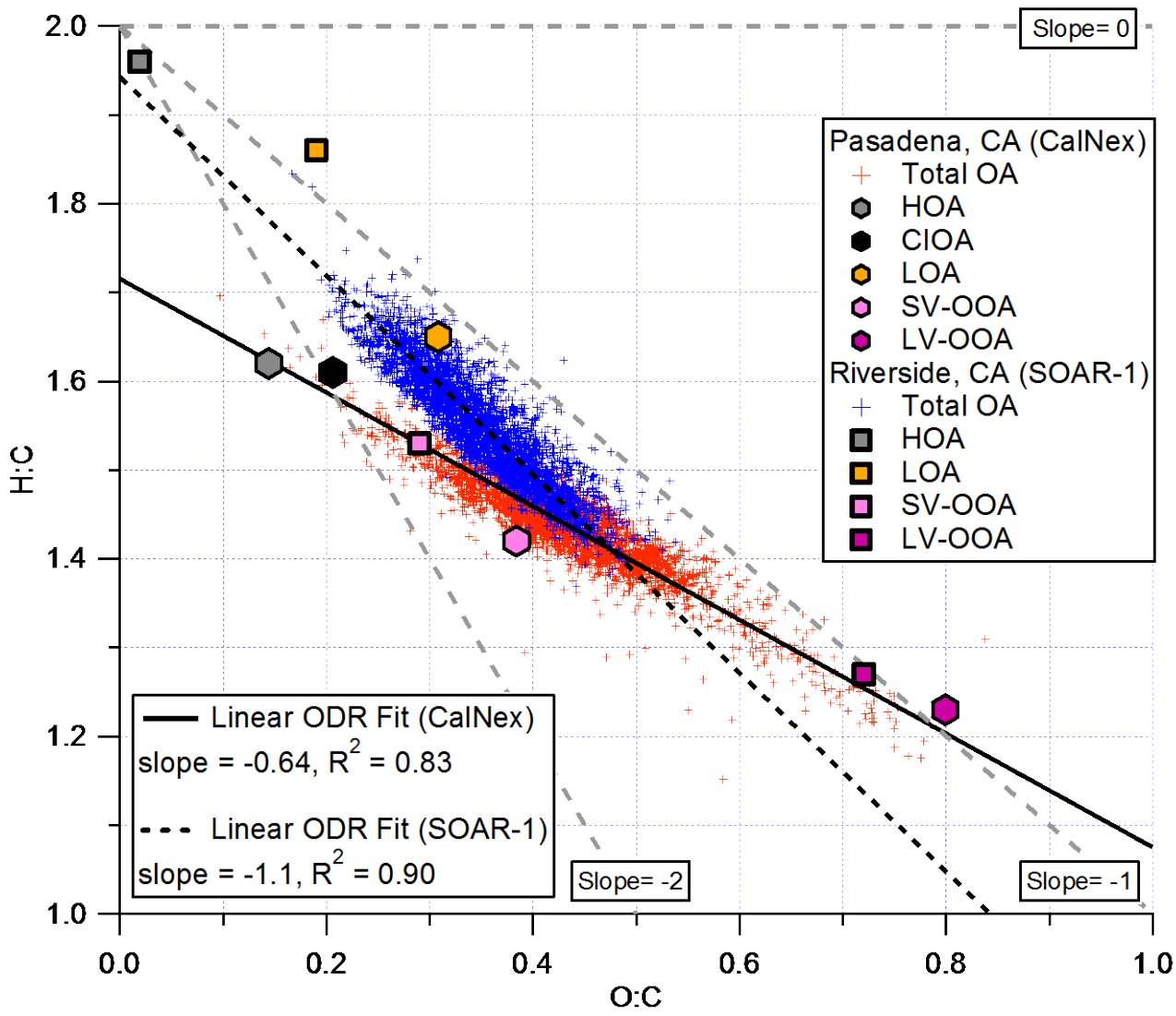

Figure 14: Van Krevelen diagram for Pasadena during the CalNex campaign (red crosses) and for Riverside, CA during the SOAR-1 campaign (blue crosses). The PMF factors identified for Pasadena (hexagons) and Riverside (squares) are shown as well. The linear regression analyses correspond to the total OA data.

4. Summary and Conclusions

Ambient aerosol measurements were made using a suite of aerosol composition instruments, including on- and off-line bulk and single particle methods at the Pasadena ground site during May and June 2010 as part of the CalNex campaign. Organic aerosols account for 41% of the total submicron aerosol mass, and the relative amounts of the organic and inorganic components for CalNex are similar to those measured during the PACO and SOAR-1 campaigns that took place previously in the Los Angeles Basin. The concentrations of sea salt and chloride are quantified for the ground site. Substantial chloride depletion is observed indicating that sodium chloride from sea salt has undergone chemical processing by pollutants before reaching Pasadena and leading to a significant fraction of $PM_{2.5}$ nitrate, with about 35% in particles larger than 1 µm in diameter. In addition, sodium from sea salt plays an important role in balancing the ionic charge of the anions in aerosol particles. The aerosol size distributions from the AMS, XRF, and SP-AMS measurements are combined to show that OA dominates at small diameters (i.e. less than ~200 nm), whereas the inorganic contribution is dominant at larger diameters (i.e. greater than ~600 nm) due to nitrate, sulfate, ammonium, and the non-EC refractory components. An in-depth analysis of OA in Pasadena was carried out including a comparison to measurements from previous field campaigns. Positive Matrix Factorization analysis of measured mass spectra resolved five OA components. The identified components are hydrocarbon-like organic aerosol (HOA, primary combustion), cooking-influenced organic aerosol (CIOA), semi-volatile oxygenated organic aerosol (SV-OOA, fresh secondary), low volatility oxygenated organic aerosol (LV-OOA, aged secondary), and amine-rich local organic aerosol (LOA) that accounts for a small amount of the OA mass. A large majority of the OA mass is classified as oxygenated / secondary (66%), but there are contributions from the primary components with HOA and CIOA accounting for 12% and 17% of the total OA mass, respectively. HOA correlates with EC, and the ratio of HOA to EC varies with the relative importance of diesel vs. gasoline vehicle emissions. Both HOA and EC exhibit weekly cycles with lower concentrations on Sundays versus weekdays consistent with the well-known weekday/weekend effect in the Los Angeles Basin. The decreases in HOA and EC concentrations are quantitatively similar to those predicted for their emissions using fuel sales, traffic counts, and literature gasoline and diesel vehicle emission ratios. The OOA to odd-oxygen ratio for Pasadena is similar to those observed in Riverside and Mexico City, which suggests that the ratios of SOA to odd-oxygen production rates are comparable at the different sites and that similar SOA and odd-oxygen formation chemistries dominate at all these locations. In addition, OA/ΔCO for Pasadena increases with photochemical age and resembles the upper limit of analogous data from Mexico City and the northeastern United States. Thus, within experimental error, the OA production per unit CO is similar or slightly more efficient in Pasadena compared to other locations. To provide an elemental and molecular-level view of OA in the Los Angeles Basin, the Van Krevelen diagrams for Pasadena and Riverside are analyzed. The Riverside Van Krevelen diagram exhibits a slope of -1.1 whereas a slope of -0.64 is observed for Pasadena. The steeper slope for Riverside may be attributable to the physical mixing of fresh HOA into the Riverside air mass. In contrast, the relatively oxidized HOA observed in Pasadena does not have the same impact on the slope. Thus, our study confirms that the aging of OOA in Riverside and Pasadena proceeds with slopes lower than -1 and close to -0.5, consistent with the results of Ng et al. [2011]. The findings reported here highlight several quantitative similarities in SOA properties observed across multiple locations including the ratios of SOA to odd-oxygen, the increases in OA/ΔCO with photochemical age, and the evolution of elemental compositions.

5. Recommendations

1) Future work should include SOA modeling studies of LA and California using box and 3-D models. Current SOA models are not well constrained, and the CalNex data set provides a unique opportunity to test these SOA models as well as other aspects of air quality models (e.g., emission inventories). In addition, improved SOA models will lead to a more detailed understanding of the important precursors and chemical pathways for SOA formation.

2) Comprehensive measurements of aerosols and their precursors, similar in scope to CalNex, should be conducted periodically (i.e., about every 5 years) in key areas of California to characterize year to year trends in emissions and the resulting impact on secondary species. Increased scope and sophistication of air quality monitoring programs will assist in this goal as well, for instance, through the deployment of Aerodyne Aerosol Chemical Speciation Monitors or similar instrumentation, as well as by time-resolved monitoring of anthropogenic and biogenic VOCs.

3) Weekly cycle studies, similar to those described in Sections II.E and II.F as well as in Bahreini et al. [2012], should be carried out in other regions of California and over longer time periods. This method is very promising for apportioning POA and SOA between diesel and gasoline emissions. While in Los Angeles it appears that SOA formation is dominated by gasoline emission, whether or not this result is true for different regions and seasons in California remains an open question. In addition, direct measurements of semi-volatile and intermediate volatility organic compounds (S/IVOCs), which have recently become available (e.g., [*Worton et al.*, 2012]), would be very useful in future studies.

References

Adachi, K., and Y. Tainosho (2004), Characterization of heavy metal particles embedded in tire dust, *Environ. Int.*, *30*(8), 1009-1017.

Ahlm, L., et al. (2012), Formation and growth of ultrafine particles from secondary sources in Bakersfield, California, *J. Geophys. Res.*, *117*, D00V08.

Aiken, A. C., P. F. DeCarlo, and J. L. Jimenez (2007), Elemental analysis of organic species with electron ionization high-resolution mass spectrometry, *Anal. Chem.*, *79*(21), 8350-8358.

Aiken, A. C., et al. (2010), Mexico city aerosol analysis during MILAGRO using high resolution aerosol mass spectrometry at the urban supersite (T0) - Part 2: Analysis of the biomass burning contribution and the non-fossil carbon fraction, *Atmos. Chem. Phys.*, *10*(12), 5315-5341.

Aiken, A. C., et al. (2008), O/C and OM/OC ratios of primary, secondary, and ambient organic aerosols with high-resolution time-of-flight aerosol mass spectrometry, *Environ. Sci. Technol.*, *42*(12), 4478-4485.

Aiken, A. C., et al. (2009), Mexico City aerosol analysis during MILAGRO using high resolution aerosol mass spectrometry at the urban supersite (T0) - Part 1: Fine particle composition and organic source apportionment, *Atmos. Chem. Phys.*, *9*(17), 6633-6653.

Allan, J. D., P. I. Williams, W. T. Morgan, C. L. Martin, M. J. Flynn, J. Lee, E. Nemitz, G. J. Phillips, M. W. Gallagher, and H. Coe (2010), Contributions from transport, solid fuel burning and cooking to primary organic aerosols in two UK cities, *Atmos. Chem. Phys.*, *10*(2), 647-668.

Allan, J. D., et al. (2003), Quantitative sampling using an Aerodyne aerosol mass spectrometer: 2. Measurements of fine particulate chemical composition in two UK cities, *J. Geophys. Res.-Atmos.*, *108*(D3), 4091.

Allan, J. D., et al. (2004), A generalised method for the extraction of chemically resolved mass spectra from Aerodyne aerosol mass spectrometer data, *J. Aerosol. Sci.*, *35*(7), 909-922.

Alpert, D. J., and P. K. Hopke (1981), A determination of the sources of airborne particles collected during the regional air-pollution study, *Atmos. Environ.*, *15*(5), 675-687.

American Lung Association (2011), State of the Air, http://www.stateoftheair.org/

Bahreini, R., et al. (2012), Gasoline emissions dominate over diesel in formation of secondary organic aerosol mass, *Geophys. Res. Lett.*, *39*(6), L06805.

Ban-Weiss, G. A., J. P. McLaughlin, R. A. Harley, A. J. Kean, E. Grosjean, and D. Grosjean (2008a), Carbonyl and nitrogen dioxide emissions from gasoline- and diesel-powered motor vehicles, *Environ. Sci. Technol.*, *42*(11), 3944-3950.

Ban-Weiss, G. A., J. P. McLaughlin, R. A. Harley, M. M. Lunden, T. W. Kirchstetter, A. J. Kean, A. W. Strawa, E. D. Stevenson, and G. R. Kendall (2008b), Long-term changes in emissions of nitrogen oxides and particulate matter from on-road gasoline and diesel vehicles, *Atmos. Environ.*, *42*(2), 220-232.

BOE: California State Board of Equalization (2011), Fuel Taxes Statistics & Reports, http://www.boe.ca.gov/sptaxprog/spftrpts.htm

Caltrans: California Department of Transportation (2010), Caltrans Performance Measurement System, http://pems.dot.ca.gov/

Canagaratna, M., et al. (2007), Chemical and Microphysical Characterization of Ambient Aerosols with the Aerodyne Aerosol Mass Spectrometer, *Mass Spectrom. Rev.*, *26*, 185-222.

Canagaratna, M. R., et al. (2004), Chase studies of particulate emissions from in-use New York City vehicles, *Aerosol Sci. Technol.*, *38*(6), 555-573.

Cappa, C. D., and J. L. Jimenez (2010), Quantitative estimates of the volatility of ambient organic aerosol, *Atmos. Chem. Phys.*, *10*(12), 5409-5424.

CARB: California Air Resources Board (2008), California Emission Inventory Data, http://www.arb.ca.gov/ei/emsmain/emsmain.htm

Chinkin, L. R., D. L. Coe, T. H. Funk, H. R. Hafner, P. T. Roberts, P. A. Ryan, and D. R. Lawson (2003), Weekday versus weekend activity patterns for ozone precursor emissions in California's South Coast Air Basin, *J. Air Waste Manage. Assoc.*, *53*(7), 829-843.

Councell, T. B., K. U. Duckenfield, E. R. Landa, and E. Callender (2004), Tire-wear particles as a source of zinc to the environment, *Environ. Sci. Technol.*, *38*(15), 4206-4214.

Croes, B. E., and E. M. Fujita (2003), Overview of the 1997 Southern California Ozone Study (SCOS97-NARSTO), *Atmos. Environ.*, *37*, S3-S26.

Cubison, M. J., et al. (2011), Effects of aging on organic aerosol from open biomass burning smoke in aircraft and laboratory studies, *Atmos. Chem. Phys.*, *11*(23), 12049-12064.

DeCarlo, P. F., et al. (2010), Investigation of the sources and processing of organic aerosol over the Central Mexican Plateau from aircraft measurements during MILAGRO, *Atmos. Chem. Phys.*, *10*(12), 5257-5280.

DeCarlo, P. F., et al. (2006), Field-Deployable, High-Resolution, Time-of-Flight Aerosol Mass Spectrometer, *Anal. Chem.*, *78*, 8281-8289.

Dick, W. D., P. J. Ziemann, and P. H. McMurry (2007), Multiangle light-scattering measurements of refractive index of submicron atmospheric particles, *Aerosol Sci. Technol.*, *41*(5), 549-569.

Docherty, K. S., et al. (2008), Apportionment of Primary and Secondary Organic Aerosols in Southern California during the 2005 Study of Organic Aerosols in Riverside (SOAR-1), *Environ. Sci. Technol.*, *42*(20), 7655-7662.

Docherty, K. S., et al. (2011), The 2005 Study of Organic Aerosols at Riverside (SOAR-1): instrumental intercomparisons and fine particle composition, *Atmos. Chem. Phys.*, *11*(23), 12387-12420.

Dockery, D. W., and C. A. Pope (1994), Acute respiratory effects of particulate air-pollution, *Annual Review of Public Health*, *15*, 107-132.

Dockery, D. W., C. A. Pope, X. P. Xu, J. D. Spengler, J. H. Ware, M. E. Fay, B. G. Ferris, and F. E. Speizer (1993), An association between air-pollution and mortality in 6 united-states cities, *New England Journal of Medicine*, *329*(24), 1753-1759.

Dunlea, E. J., et al. (2009), Evolution of Asian aerosols during transpacific transport in INTEX-B, *Atmos. Chem. Phys.*, *9*(19), 7257-7287.

Duong, H. T., A. Sorooshian, J. S. Craven, S. P. Hersey, A. R. Metcalf, X. L. Zhang, R. J. Weber, H. Jonsson, R. C. Flagan, and J. H. Seinfeld (2011), Water-soluble organic aerosol in the Los Angeles Basin and outflow regions: Airborne and ground measurements during the 2010 CalNex field campaign, *J. Geophys. Res.-Atmos.*, *116*.

Dusanter, S., D. Vimal, P. S. Stevens, R. Volkamer, and L. T. Molina (2009), Measurements of OH and HO2 concentrations during the MCMA-2006 field campaign – Part 1: Deployment of the Indiana University laser-induced fluorescence instrument, *Atmos. Chem. Phys.*, *9*(5), 1665-1685.

Dzepina, K., R. M. Volkamer, S. Madronich, P. Tulet, I. M. Ulbrich, Q. Zhang, C. D. Cappa, P. J. Ziemann, and J. L. Jimenez (2009), Evaluation of recently-proposed secondary organic aerosol models for a case study in Mexico City, *Atmos. Chem. Phys.*, *9*(15), 5681-5709.

Farmer, D. K., A. Matsunaga, K. S. Docherty, J. D. Surratt, J. H. Seinfeld, P. J. Ziemann, and J. L. Jimenez (2010), Response of an aerosol mass spectrometer to organonitrates and organosulfates and implications for atmospheric chemistry, *Proceedings of the National Academy of Sciences of the United States of America*, *107*(15), 6670-6675.

Fine, P. M., S. Shen, and C. Sioutas (2004), Inferring the sources of fine and ultrafine particulate matter at downwind receptor sites in the Los Angeles basin using multiple continuous measurements, *Aerosol Sci. Technol.*, *38*, 182-195.

Finlayson-Pitts, B. J., and J. N. Pitts (2000), *Chemistry of the Upper and Lower Atmosphere*, Academic Press, San Diego.

Froyd, K. D., D. M. Murphy, T. J. Sanford, D. S. Thomson, J. C. Wilson, L. Pfister, and L. Lait (2009), Aerosol composition of the tropical upper troposphere, *Atmos. Chem. Phys.*, *9*(13), 4363-4385.

Fruin, S. A., M. J. St Denis, A. M. Winer, S. D. Colome, and F. W. Lurmann (2001), Reductions in human benzene exposure in the California South Coast Air Basin, *Atmos. Environ.*, *35*(6), 1069-1077.

Gard, E. E., et al. (1998), Direct observation of heterogeneous chemistry in the atmosphere, *Science*, *279*(5354), 1184-1187.

Ge, X. L., A. S. Wexler, and S. L. Clegg (2011), Atmospheric amines - Part I. A review, *Atmos. Environ.*, *45*(3), 524-546.

Gerbig, C., S. Schmitgen, D. Kley, A. Volz-Thomas, K. Dewey, and D. Haaks (1999), An improved fast-response vacuum-UV resonance fluorescence CO instrument, *J. Geophys. Res.-Atmos.*, *104*(D1), 1699-1704.

Gilman, J. B., et al. (2009), Measurements of volatile organic compounds during the 2006 TexAQS/GoMACCS campaign: Industrial influences, regional characteristics, and diurnal dependencies of the OH reactivity, *J. Geophys. Res.*, *114*, D00F06.

Griffin, R. J., J. J. Chen, K. Carmody, S. Vutukuru, and D. Dabdub (2007), Contribution of gas phase oxidation of volatile organic compounds to atmospheric carbon monoxide levels in two areas of the United States, *J. Geophys. Res.-Atmos.*, *112*(D10), D10S17.

Grover, B. D., M. Kleinman, N. L. Eatough, D. J. Eatough, R. A. Cary, P. K. Hopke, and W. E. Wilson (2008), Measurement of fine particulate matter nonvolatile and semi-volatile organic material with the Sunset Laboratory Carbon Aerosol Monitor, *J. Air Waste Manage. Assoc.*, *58*(1), 72-77.

Hall, J. S., and E. W. Wolff (1998), Causes of seasonal and daily variations in aerosol sea-salt concentrations at a coastal Antarctic station, *Atmos. Environ.*, *32*(21), 3669-3677.

Haman, C. L., B. Lefer, and G. A. Morris (2012), Seasonal Variability in the Diurnal Evolution of the Boundary Layer in a Near Coastal Urban Environment, *Journal of Atmospheric and Oceanic Technology*.

Harley, R. A., R. F. Sawyer, and J. B. Milford (1997), Updated photochemical modeling for California's South Coast Air Basin: Comparison of chemical mechanisms and motor vehicle emission inventories, *Environ. Sci. Technol.*, *31*(10), 2829-2839.

Heald, C. L., J. H. Kroll, J. L. Jimenez, K. S. Docherty, P. F. DeCarlo, A. C. Aiken, Q. Chen, S. T. Martin, D. K. Farmer, and P. Artaxo (2010), A simplified description of the evolution of organic aerosol composition in the atmosphere, *Geophys. Res. Lett.*, *37*, L08803.

Herndon, S. C., et al. (2008), Correlation of secondary organic aerosol with odd oxygen in Mexico City, *Geophys. Res. Lett.*, *35*(15), L15804.

Hersey, S. P., J. S. Craven, K. A. Schilling, A. R. Metcalf, A. Sorooshian, M. N. Chan, R. C. Flagan, and J. H. Seinfeld (2011), The Pasadena Aerosol Characterization Observatory (PACO): chemical and physical analysis of the Western Los Angeles basin aerosol, *Atmos. Chem. Phys.*, *11*(15), 7417-7443.

Hildebrandt, L., E. Kostenidou, V. A. Lanz, A. S. H. Prevot, U. Baltensperger, N. Mihalopoulos, A. Laaksonen, N. M. Donahue, and S. N. Pandis (2011), Sources and atmospheric processing of organic aerosol in the Mediterranean: insights from aerosol mass spectrometer factor analysis, *Atmos. Chem. Phys.*, *11*(23), 12499-12515.

Hildemann, L. M., G. R. Markowski, and G. R. Cass (1991), Chemical-composition of emissions from urban sources of fine organic aerosol, *Environ. Sci. Technol.*, *25*(4), 744-759.

Hjortenkrans, D. S. T., B. G. Bergback, and A. V. Haggerud (2007), Metal emissions from brake linings and tires: Case studies of Stockholm, Sweden 1995/1998 and 2005, *Environ. Sci. Technol.*, *41*(15), 5224-5230.

Huffman, J. A., et al. (2009), Chemically-resolved aerosol volatility measurements from two megacity field studies, *Atmos. Chem. Phys.*, *9*(18), 7161-7182.

IPCC (2007), Climate Change 2007: The Physical Scientific Basis*Rep.*, Cambridge University Press, Cambridge England.

Jacob, D. J., et al. (2010), The Arctic Research of the Composition of the Troposphere from Aircraft and Satellites (ARCTAS) mission: design, execution, and first results, *Atmos. Chem. Phys.*, *10*(11), 5191-5212.

Jakober, C. A., M. J. Charles, M. J. Kleeman, and P. G. Green (2006), LC-MS analysis of carbonyl compounds and their occurrence in diesel emissions, *Anal. Chem.*, *78*(14), 5086-5093.

Jakober, C. A., M. A. Robert, S. G. Riddle, H. Destaillats, M. J. Charles, P. G. Green, and M. J. Kleeman (2008), Carbonyl emissions from gasoline and diesel motor vehicles, *Environ. Sci. Technol.*, *42*(13), 4697-4703.

Jimenez, J. L., et al. (2003), Ambient aerosol sampling using the Aerodyne Aerosol Mass Spectrometer, *J. Geophys. Res.-Atmos.*, *108*(D7), 8425.

Jimenez, J. L., et al. (2009), Evolution of Organic Aerosols in the Atmosphere, *Science*, *326*(5959), 1525-1529.

Johnson, K. S., A. Laskin, J. L. Jimenez, V. Shutthanandan, L. T. Molina, D. Salcedo, K. Dzepina, and M. J. Molina (2008), Comparative analysis of urban atmospheric aerosol by particle-induced X-ray emission (PIXE), proton elastic scattering analysis (PESA), and aerosol mass spectrometry (AMS), *Environ. Sci. Technol.*, *42*(17), 6619-6624.

Kang, E., D. W. Toohey, and W. H. Brune (2011), Dependence of SOA oxidation on organic aerosol mass concentration and OH exposure: experimental PAM chamber studies, *Atmos. Chem. Phys.*, *11*(4), 1837-1852.

Kang, E., M. J. Root, D. W. Toohey, and W. H. Brune (2007), Introducing the concept of Potential Aerosol Mass (PAM), *Atmos. Chem. Phys.*, *7*(22), 5727-5744.

Kebabian, P. L., W. A. Robinson, and A. Freedman (2007), Optical extinction monitor using cw cavity enhanced detection, *Rev. Sci. Instrum.*, *78*(6), 063102.

Kleinman, L. I., et al. (2007), Aircraft observations of aerosol composition and ageing in New England and Mid-Atlantic States during the summer 2002 New England Air Quality Study field campaign, *J. Geophys. Res.-Atmos.*, *112*(D9), D09310.

Kleinman, L. I., et al. (2008), The time evolution of aerosol composition over the Mexico City plateau, *Atmos. Chem. Phys.*, *8*(6), 1559-1575.

Lambe, A. T., et al. (2012), Transitions from Functionalization to Fragmentation Reactions of Laboratory Secondary Organic Aerosol (SOA) Generated from the OH Oxidation of Alkane Precursors, *Environ. Sci. Technol.*

Lanz, V. A., M. R. Alfarra, U. Baltensperger, B. Buchmann, C. Hueglin, and A. S. H. Prevot (2007), Source apportionment of submicron organic aerosols at an urban site by factor analytical modelling of aerosol mass spectra, *Atmos. Chem. Phys.*, *7*(6), 1503-1522.

Lanz, V. A., et al. (2008), Source attribution of submicron organic aerosols during wintertime inversions by advanced factor analysis of aerosol mass spectra, *Environ. Sci. Technol.*, *42*(1), 214-220.

Lawson, D. R. (1990), The southern california air-quality study, *J. Air Waste Manage. Assoc.*, *40*(2), 156-165.

Lee, S. C., W. M. Li, and L. Y. Chan (2001), Indoor air quality at restaurants with different styles of cooking in metropolitan Hong Kong, *Sci. Total Environ.*, *279*(1-3), 181-193.

Liu, S., D. A. Day, J. E. Shields, and L. M. Russell (2011), Ozone-driven daytime formation of secondary organic aerosol containing carboxylic acid groups and alkane groups, *Atmos. Chem. Phys.*, *11*(16), 8321-8341.

Lu, R., and R. P. Turco (1995), Air pollutant transport in a coastal environment .2. 3-dimensional simulations over los-angeles basin, *Atmos. Environ.*, *29*(13), 1499-1518.

Malm, W. C., J. F. Sisler, D. Huffman, R. A. Eldred, and T. A. Cahill (1994), Spatial and seasonal trends in particle concentration and optical extinction in the united-states, *J. Geophys. Res.-Atmos.*, *99*(D1), 1347-1370.

Marr, L. C., and R. A. Harley (2002), Spectral analysis of weekday-weekend differences in ambient ozone, nitrogen oxide, and non-methane hydrocarbon time series in California, *Atmos. Environ.*, *36*(14), 2327-2335.

Massoli, P., P. L. Kebabian, T. B. Onasch, F. B. Hills, and A. Freedman (2010), Aerosol Light Extinction Measurements by Cavity Attenuated Phase Shift (CAPS) Spectroscopy: Laboratory Validation and Field Deployment of a Compact Aerosol Particle Extinction Monitor, *Aerosol Sci. Technol.*, *44*(6), 428-435.

McDonald, J. D., B. Zielinska, E. M. Fujita, J. C. Sagebiel, J. C. Chow, and J. G. Watson (2003), Emissions from charbroiling and grilling of chicken and beef, *J. Air Waste Manage. Assoc.*, *53*(2), 185-194.

McLafferty, F. W., and F. Turecek (1993), *Interpretation of Mass Spectra*, 4th ed., University Science Books, Sausalito, CA.

Middlebrook, A. M., R. Bahreini, J. L. Jimenez, and M. R. Canagaratna (2012), Evaluation of Composition-Dependent Collection Efficiencies for the Aerodyne Aerosol Mass Spectrometer using Field Data, *Aerosol Sci. Technol.*, *46*(3), 258-271.

Millstein, D. E., R. A. Harley, and S. V. Hering (2008), Weekly cycles in fine particulate nitrate, *Atmos. Environ.*, *42*(4), 632-641.

Mohr, C., et al. (2011), Identification and quantification of organic aerosol from cooking and other sources in Barcelona using aerosol mass spectrometer data, *Atmos. Chem. Phys.*, *11*(10), 1649-1665.

Nehrkorn, T., J. Eluszkiewicz, S. C. Wofsy, J. C. Lin, C. Gerbig, M. Longo, and S. Freitas (2010), Coupled weather research and forecasting-stochastic time-inverted lagrangian transport (WRF-STILT) model, *Meteorol. Atmos. Phys.*, *107*(1-2), 51-64.

Nemitz, E. (2010), Aerosol Mass Spectrometer Network Measurements during the EUCAARI/EMEP Intensive Measurement Campaigns, paper presented at Aerodyne Aerosol Mass Spectrometer Users Meeting, Hyytiala, Finland, 4 - 6 Sept.

Neuman, J. A., et al. (2003), Variability in ammonium nitrate formation and nitric acid depletion with altitude and location over California, *J. Geophys. Res.-Atmos.*, *108*(D17), 4557.

Ng, N. L., M. R. Canagaratna, J. L. Jimenez, P. S. Chhabra, J. H. Seinfeld, and D. R. Worsnop (2011), Changes in organic aerosol composition with aging inferred from aerosol mass spectra, *Atmos. Chem. Phys.*, *11*(13), 6465-6474.

NOAA: National Oceanic and Atmospheric Administration (2008), 2010 CalNex White Paper: Research at the Nexus of Air Quality and Climate Change, http://www.esrl.noaa.gov/csd/projects/calnex/whitepaper.pdf

Onasch, T. B., A. Trimborn, E. C. Fortner, J. T. Jayne, G. L. Kok, L. R. Williams, P. Davidovits, and D. R. Worsnop (2012), Soot Particle Aerosol Mass Spectrometer: Development, Validation, and Initial Application, *Aerosol Sci. Technol.*, *46*(7), 804-817.

Orsini, D. A., Y. L. Ma, A. Sullivan, B. Sierau, K. Baumann, and R. J. Weber (2003), Refinements to the particle-into-liquid sampler (PILS) for ground and airborne measurements of water soluble aerosol composition, *Atmos. Environ.*, *37*(9-10), 1243-1259.

Paatero, P., and U. Tapper (1994), Positive matrix factorization - a nonnegative factor model with optimal utilization of error-estimates of data values, *Environmetrics*, *5*(2), 111-126.

Paatero, P., and P. K. Hopke (2003), Discarding or downweighting high-noise variables in factor analytic models, *Analytica Chimica Acta*, *490*(1–2), 277-289.

Parrish, D. D., M. Trainer, D. Hereid, E. J. Williams, K. J. Olszyna, R. A. Harley, J. F. Meagher, and F. C. Fehsenfeld (2002), Decadal change in carbon monoxide to nitrogen oxide ratio in US vehicular emissions, *J. Geophys. Res.-Atmos.*, *107*(D12), 4140.

Parrish, D. D., A. Stohl, C. Forster, E. L. Atlas, D. R. Blake, P. D. Goldan, W. C. Kuster, and J. A. de Gouw (2007), Effects of mixing on evolution of hydrocarbon ratios in the troposphere, *J. Geophys. Res.-Atmos.*, *112*(D10), D10S34.

Peltier, R. E., R. J. Weber, and A. P. Sullivan (2007), Investigating a liquid-based method for online organic carbon detection in atmospheric particles, *Aerosol Sci. Technol.*, *41*(12), 1117-1127.

Pollack, I. B., et al. (2012), Airborne and ground-based observations of a weekend effect in ozone, precursors, and oxidation products in the California South Coast Air Basin, *J. Geophys. Res.*, *117*, D00V05.

Robinson, A. L., R. Subramanian, N. M. Donahue, A. Bernardo-Bricker, and W. F. Rogge (2006), Source apportionment of molecular markers and organic aerosol. 3. Food cooking emissions, *Environ. Sci. Technol.*, *40*(24), 7820-7827.

Robinson, C.B., J.R. Kimmel, D.E. David, J.T. Jayne, A. Trimborn, D.R. Worsnop, and J.L. Jimenez. Thermal Desorption Metastable Atom Bombardment Aerosol Mass Spectrometry. *Int. J. Mass. Spec.*, 303, 164–172, DOI: 10.1016/j.ijms.2011.01.027, 2011.

Russell, L. M., L. N. Hawkins, A. A. Frossard, P. K. Quinn, and T. S. Bates (2010), Carbohydrate-like composition of submicron atmospheric particles and their production from ocean bubble bursting, *Proceedings of the National Academy of Sciences of the United States of America*, *107*(15), 6652-6657.

Russell, L. M., S. Takahama, S. Liu, L. N. Hawkins, D. S. Covert, P. K. Quinn, and T. S. Bates (2009a), Oxygenated fraction and mass of organic aerosol from direct emission and atmospheric processing measured on the R/V Ronald Brown during TEXAQS/GoMACCS 2006, *J. Geophys. Res.-Atmos.*, *114*, D00F05.

Russell, L. M., R. Bahadur, L. N. Hawkins, J. Allan, D. Baumgardner, P. K. Quinn, and T. S. Bates (2009b), Organic aerosol characterization by complementary measurements of chemical bonds and molecular fragments, *Atmos. Environ.*, *43*(38), 6100-6105.

Salcedo, D., et al. (2006), Characterization of ambient aerosols in Mexico City during the MCMA-2003 campaign with Aerosol Mass Spectrometry: results from the CENICA Supersite, *Atmos. Chem. Phys.*, *6*, 925-946.

Salma, I., and W. Maenhaut (2006), Changes in elemental composition and mass of atmospheric aerosol pollution between 1996 and 2002 in a Central European city, *Environmental Pollution*, *143*(3), 479-488.

Schauer, J. J., M. J. Kleeman, G. R. Cass, and B. R. T. Simoneit (1999a), Measurement of emissions from air pollution sources. 2. C-1 through C-30 organic compounds from medium duty diesel trucks, *Environ. Sci. Technol.*, *33*(10), 1578-1587.

Schauer, J. J., M. J. Kleeman, G. R. Cass, and B. R. T. Simoneit (1999b), Measurement of emissions from air pollution sources. 1. C-1 through C-29 organic compounds from meat charbroiling, *Environ. Sci. Technol.*, *33*(10), 1566-1577.

Schauer, J. J., M. J. Kleeman, G. R. Cass, and B. R. T. Simoneit (2002a), Measurement of emissions from air pollution sources. 5. C-1-C-32 organic compounds from gasoline-powered motor vehicles, *Environ. Sci. Technol.*, *36*(6), 1169-1180.

Schauer, J. J., M. J. Kleeman, G. R. Cass, and B. R. T. Simoneit (2002b), Measurement of emissions from air pollution sources. 4. C-1-C-27 organic compounds from cooking with seed oils, *Environ. Sci. Technol.*, *36*(4), 567-575.

Schwarz, J. P., et al. (2006), Single-particle measurements of midlatitude black carbon and light-scattering aerosols from the boundary layer to the lower stratosphere, *J. Geophys. Res.-Atmos.*, *111*(D16), D16207.

Simon, H., P. V. Bhave, J. L. Swall, N. H. Frank, and W. C. Malm (2011), Determining the spatial and seasonal variability in OM/OC ratios across the US using multiple regression, *Atmos. Chem. Phys.*, *11*(6), 2933-2949.

Slowik, J. G., et al. (2010), Characterization of a large biogenic secondary organic aerosol event from eastern Canadian forests, *Atmos. Chem. Phys.*, *10*(6), 2825-2845.

Sommariva, R., J. A. de Gouw, M. Trainer, E. Atlas, P. D. Goldan, W. C. Kuster, C. Warneke, and F. C. Fehsenfeld (2011), Emissions and photochemistry of oxygenated VOCs in urban plumes in the Northeastern United States, *Atmos. Chem. Phys.*, *11*(14), 7081-7096.

Stohl, A., C. Forster, A. Frank, P. Seibert, and G. Wotawa (2005), Technical note: The Lagrangian particle dispersion model FLEXPART version 6.2, *Atmos. Chem. Phys.*, *5*, 2461-2474.

Sueper, D. (2011), "ToF-AMS Analysis Software", http://cires.colorado.edu/jimenez-group/wiki/index.php/ToF-AMS_Analysis_Software

Sun, Y. L., et al. (2011), Characterization of the sources and processes of organic and inorganic aerosols in New York city with a high-resolution time-of-flight aerosol mass apectrometer, *Atmos. Chem. Phys.*, *11*(4), 1581-1602.

Thalman, R., and R. Volkamer (2010), Inherent calibration of a blue LED-CE-DOAS instrument to measure iodine oxide, glyoxal, methyl glyoxal, nitrogen dioxide, water vapour and aerosol extinction in open cavity mode, *Atmos. Meas. Tech.*, *3*(6), 1797-1814.

Thompson, J., P. L. Hayes, J. L. Jimenez, K. Adachi, X. Zhang, J. Liu, R. J. Weber, and P. R. Buseck (2012), Aerosol Optical Properties at Pasadena, CA During CalNex 2010, *Atmos. Environ.*, *55*, 190.

Thomson, D. S., M. E. Schein, and D. M. Murphy (2000), Particle analysis by laser mass spectrometry WB-57F instrument overview, *Aerosol Sci. Technol.*, *33*(1-2), 153-169.

Turpin, B. J., and H. J. Lim (2001), Species contributions to PM2.5 mass concentrations: Revisiting common assumptions for estimating organic mass, *Aerosol Sci. Technol.*, *35*(1), 602-610.

Ulbrich, I. M., M. R. Canagaratna, Q. Zhang, D. R. Worsnop, and J. L. Jimenez (2009), Interpretation of organic components from Positive Matrix Factorization of aerosol mass spectrometric data, *Atmos. Chem. Phys.*, *9*(9), 2891-2918.

Ulbrich, I. M., M. R. Canagaratna, M. J. Cubison, Q. Zhang, N. L. Ng, A. C. Aiken, and J. L. Jimenez (2012), Three-dimensional factorization of size-resolved organic aerosol mass spectra from Mexico City, *Atmos. Meas. Tech.*, *5*(1), 195-224.

Veres, P. R., et al. (2011), Evidence of rapid production of organic acids in an urban air mass, *Geophys. Res. Lett.*, *38*, L17807.

Washenfelder, R. A., et al. (2011), The glyoxal budget and its contribution to organic aerosol for Los Angeles, California, during CalNex 2010, *J. Geophys. Res.-Atmos.*, *116*, D00V02.

Watson, J. G. (2002), Visibility: Science and regulation, *J. Air Waste Manage. Assoc.*, *52*(6), 628-713.

Williams, B. J., A. H. Goldstein, N. M. Kreisberg, and S. V. Hering (2006), An in-situ instrument for speciated organic composition of atmospheric aerosols: Thermal Desorption Aerosol GC/MS-FID (TAG), *Aerosol Sci. Technol.*, *40*(8), 627-638.

Williams, B. J., A. H. Goldstein, N. M. Kreisberg, S. V. Hering, D. R. Worsnop, I. M. Ulbrich, K. S. Docherty, and J. L. Jimenez (2010), Major components of atmospheric organic aerosol in southern California as determined by hourly measurements of source marker compounds, *Atmos. Chem. Phys.*, *10*(23), 11577-11603.

Wonaschutz, A., S. P. Hersey, A. Sorooshian, J. S. Craven, A. R. Metcalf, R. C. Flagan, and J. H. Seinfeld (2011), Impact of a large wildfire on water-soluble organic aerosol in a major urban area: the 2009 Station Fire in Los Angeles County, *Atmos. Chem. Phys.*, *11*(16), 8257-8270.

Wood, E. C., et al. (2010), Investigation of the correlation between odd oxygen and secondary organic aerosol in Mexico City and Houston, *Atmos. Chem. Phys.*, *10*(18), 8947-8968.

Worton, D. R., N. M. Kreisberg, G. Isaacman, A. P. Teng, C. McNeish, T. Górecki, S. V. Hering, and A. H. Goldstein (2012), Thermal Desorption Comprehensive Two-Dimensional Gas Chromatography: An Improved Instrument for In-Situ Speciated Measurements of Organic Aerosols, *Aerosol Sci. Technol.*, *46*(4), 380-393.

Yatavelli, R.L.N., F. Lopez-Hilfiker, J.D. Wargo, J.R. Kimmel, M.J. Cubison, T.H. Bertram, J.L. Jimenez, M. Gonin, D.R. Worsnop, J.A. Thornton. A Chemical Ionization High-Resolution Time-of-Flight Mass Spectrometer Coupled to a Micro Orifice Volatilization Impactor (MOVI-HRToF-CIMS) for Analysis of Gas and Particle-Phase Organic Species. *Aerosol Sci. Technol.*, 46, 1313–1327, 2012.

Zelenyuk, A., Y. Cai, L. Chieffo, and D. Imre (2005), High precision density measurements of single particles: The density of metastable phases, *Aerosol Sci. Technol.*, *39*(10), 972-986.

Zhang, Q., D. R. Worsnop, M. R. Canagaratna, and J. L. Jimenez (2005), Hydrocarbon-like and oxygenated organic aerosols in Pittsburgh: insights into sources and processes of organic aerosols, *Atmos. Chem. Phys.*, *5*, 3289-3311.

Zhang, Q., J. L. Jimenez, D. R. Worsnop, and M. Canagaratna (2007a), A case study of urban particle acidity and its influence on secondary organic aerosol, *Environ. Sci. Technol.*, *41*(9), 3213-3219.

Zhang, Q., J. L. Jimenez, M. R. Canagaratna, I. M. Ulbrich, N. L. Ng, D. R. Worsnop, and Y. L. Sun (2011), Understanding atmospheric organic aerosols via factor analysis of aerosol mass spectrometry: a review, *Anal. Bioanal. Chem.*, *401*(10), 3045-3067.

Zhang, Q., et al. (2007b), Ubiquity and Dominance of Oxygenated Species in Organic Aerosols in Anthropogenically—Influenced Northern Hemisphere Mid-latitudes. , *Geophys. Res. Lett.*, *34*, L13801.

Zhang, X., A. Hecobian, M. Zheng, N. H. Frank, and R. J. Weber (2010), Biomass burning impact on PM(2.5) over the southeastern US during 2007: integrating chemically speciated FRM filter measurements, MODIS fire counts and PMF analysis, *Atmos. Chem. Phys.*, *10*(14), 6839-6853.

Zhuang, H., C. K. Chan, M. Fang, and A. S. Wexler (1999), Formation of nitrate and non-sea-salt sulfate on coarse particles, *Atmos. Environ.*, *33*(26), 4223-4233.

Zorn, S. R., F. Drewnick, M. Schott, T. Hoffmann, and S. Borrmann (2008), Characterization of the South Atlantic marine boundary layer aerosol using an aerodyne aerosol mass spectrometer, *Atmos. Chem. Phys.*, *8*(16), 4711-4728.

List of Publications Produced

(13) Mielke, L.H., J. Stutz, C. Tsai, S. C. Hurlock, J. M. Roberts, P. R. Veres, K. D. Froyd, P. L. Hayes, M. J. Cubison, J. L. Jimenez, R. A.Washenfelder, C. J. Young, J. B. Gilman, J. A. de Gouw, J.H. Flynn, N. Grossberg, B.L. Lefer, J. Liu, R.J. Weber, and H.D. Osthoff. Heterogeneous formation of nitryl chloride and its role as a nocturnal NOx reservoir species during CalNex-LA 2010. *J. Geophys. Res.-Atmos.*, submitted, Jan. 2013.

(12) Chan, A.W.H., G. Isaacman, K.R. Wilson, D.R. Worton, C.R. Ruehl, T. Nah, D.R. Gentner, T.R. Dallman, T.W. Kirchstetter, R.A. Harley, J.B. Gilman, W.C. Kuster, J.A. de Gouw, J.H. Offenberg, T.E. Kleindienst, Y.H. Lin, C.L. Rubitschun, J.D. Surratt, P.L. Hayes, J.L. Jimenez, and A.H. Goldstein. Detailed Chemical Characterization of Unresolved Complex Mixtures (UCM) in Atmospheric Organics: Insights into Emission Sources, Atmospheric Processing and Secondary Organic Aerosol Formation. *J. Geophys. Res.-Atmos.*, submitted, May 2012.

(11) Massoli, P., T.B. Onasch, P.L. Hayes, J.W. Taylor, J.D. Allan, P. Kebabian, J. Brioude, W. Angevine, H. Coe, J.L. Jimenez, and A. Freedman. Effect of Particle Size and Chemical Composition on Aerosol Optical Properties measured in Pasadena, CA during the CalNex-LA 2010 campaign. *J. Geophys. Res.-Atmos*, submitted, July 2012.

(10) Ryerson, T.B., A.E. Andrews, W.M. Angevine, T.S. Bates, C.A. Brock, B. Cairns, R.C. Cohen, O.R. Cooper, J.A. de Gouw, F.C. Fehsenfeld, R.A. Ferrare, M.L. Fischer, R.C. Flagan, A.H. Goldstein, J.W. Hair, R.M. Hardesty, C.A. Hostetler, J.L. Jimenez, A.O. Langford, E. McCauley, S.A. McKeen, L.T. Molina, A. Nenes, S.J. Oltmans, D.D. Parrish, J.R. Pederson, R.B. Pierce, K. Prather, P.K. Quinn, J.H. Seinfeld, C.J. Senff, A. Sorooshian, J. Stutz, J.D. Surratt, M. Trainer, R. Volkamer, E.J. Williams, and S.C. Wofsy. The 2010 California Research at the Nexus of Air Quality and Climate Change (CalNex) field study. *J. Geophys. Res.-Atmos.*, , revised, Jan. 2013.

(9) Mei, F., Hayes, P.L., Ortega, A., Taylor, J.W., Allan, J.D., Gilman, J., Kuster, W., de Gouw, J., Jimenez, J.L., Wang, J. Droplet activation properties of organic aerosols observed at an urban site during CalNex-LA. *J. Geophys. Res.-Atmos.*, submitted, July 2012.

(8) Hayes, P.L., Ortega, A.M., Cubison, M.J., Froyd, K.D., Zhao, Y., Cliff, S.S., Hu, W.W., Toohey, D.W., Flynn, J.H., Lefer, B.L., Grossberg, N., Alvarez, S., Rappenglück, B., Taylor, J.W., Allan, J.D., Holloway, J.S., Gilman, J.B., Kuster, W.C., de Gouw, J.A., Massoli, P., Zhang, X., Liu, J., Weber, R.J., Corrigan, A.L., Russell, L.M., Isaacman, G., Worton, D.R., Kreisberg, N.M., Hering, S.V., Goldstein, A.H., Thalman, R., Waxman, E.M., Volkamer, R., Lin, Y.H., Surratt, J.D., Kleindienst, T.E., Offenberg, J.H., Dusanter, S., Griffith, S., Stevens, P.S., Brioude, J., Angevine, W.M., Jimenez, J.L. "Aerosol Composition and Sources in Los Angeles During the 2010 CalNex Campaign" *J. Geophys. Res.-Atmos.*, submitted, May 2012.

(7) R.E. O'Brien, T.B. Nguyen, A. Laskin, J. Laskin, P.L. Hayes, S. Liu, J.L. Jimenez, L.M. Russell, S.A. Nizkorodov, A.H. Goldstein. Probing Molecular Associations of Field-Collected and Laboratory-Generated SOA with Nano-DESI High-Resolution Mass Spectrometry. *J. Geophys. Res.-Atmos*, in press, Dec. 2012.

(6) Ensberg, J.J., Craven, J.S., Metcalf, A.R., Angevine, W.M., Bahreini, R., Brioude, J., Cai, C., de Gouw, J.A., Ellis, R., Flynn, J.H., Haman, C.L., Hayes, P.L., Jimenez, J.L., Lefer, B.L., Middlebrook, A.M., Murphy, J.G., Neuman, J.A., Nowak, J.B., Roberts, J.M., Stutz, J., Veres, P.R., Walker, J.M., Seinfeld, J.H. "Inorganic and black carbon aerosols in the Los Angeles Basin during CalNex" *J. Geophys. Res.-Atmos.*, in press, May 2012.

(5) Zhang, X., Liu, J., Parker, E.T., Hayes, P.L., Jimenez, J.L., de Gouw, J.A., Flynn, J.H., Grossberg, N., Lefer, B.L., Weber, R.J. "On the Gas-Particle Partitioning of Soluble Organic Aerosol in Two Urban Atmospheres with Contrasting Emissions: Part 1. Bulk Water-Soluble Organic Carbon." *J. Geophys. Res.-Atmos.*, **2012,** *117,* D00V16.

(4) Liu, J., Zhang, X., Parker, E.T., Veres, P.R., Roberts, J.M., de Gouw, J.A., Hayes, P.L**.,** Jimenez, J.L., Murphy, J., Ellis, R., Huey, L.G., Weber., R.J. "On the Gas-Particle Partitioning of Soluble Organic Aerosol in Two Urban Atmospheres with Contrasting Emissions: Part 2. Gas and Particle Phase Formic Acid." *J. Geophys. Res.-Atmos.*, **2012,** *117,* D00V21.

(3) Thompson, J.E., Hayes, P.L**.,** Jimenez, J.L., Adachi, K., Zhang, X., Liu, J., Weber, R.J., Buseck, P.R. "Aerosol optical properties at Pasadena, CA during CalNex 2010" *Atmos. Environ.*, **2012**, 55, 190.

(2) Cubison, M.J., Ortega, A.M., Hayes, P.L., Farmer, D.K., Day, D., Lechner, M.J., Brune, W.H., Apel, E., Diskin, G.S., Fisher, J.A., Fuelberg, H.E., Hecobian, A., Knapp, D.J., Mikoviny, T., Riemer, D., Sachse, G.W., Sessions, W., Weber, R.J., Weinheimer, A.J., Wisthaler, A., Jimenez, J.L. "Effects of Aging on Organic Aerosol from Open Biomass Burning Smoke in Aircraft and Laboratory Studies"*Atmos. Chem. Phys.*, **2011**, 11, 12049.

(1) Washenfelder, R.A., Young, C.J., Brown, S.S., Angevine, W.M., Atlas, E.L., Blake, D.R., Bon, D.M., Cubison, M.J., de Gouw, J.A., Dusanter, S., Flynn, J., Gilman, J.B., Graus, M., Griffith, S., Grossberg, N., Hayes, P.L**.,** Jimenez, J.L., Kuster, W.C., Lefer, B.L., Pollack, I.B., Ryerson, T.B., Stark, H., Stevens, P.S., Trainer, M.K. "The glyoxal budget and its contribution to organic aerosol for Los Angeles, California during CalNex 2010" *J. Geophys. Res.-Atmos.* **2011**, 116, D00V02.

Glossary of Terms, Abbreviations, and Symbols

ΔCO	Enhanced CO concentration over background concentration
2DTAG	2-Dimensional Thermal Desorption Aerosol Gas Chromatography Mass Spectrometry
AMS	High Resolution Time-of-Flight Aerosol Mass Spectrometer
BBOA	Biomass Burning Organic Aerosol
Caltech	California Institute of Technology
CalNex	California Research at the Nexus of Air Quality and Climate Change field campaign
CAPS	Cavity Attenuated Phase Shift
CE-DOAS	Cavity Enhanced Differential Optical Absorption Spectroscopy
CIOA	Cooking-Influenced Organic Aerosol
EC	Elemental Carbon
f_{55}, f_{57}, f_{60}	Fraction of the total organic signal at m/z 55, m/z 57, and m/z 60, respectively
GC-MS	Gas Chromatography Mass Spectrometry
HOA	Hydrocarbon-like Organic Aerosol
LA	Los Angeles
LOA	Local Organic Aerosol
LV-OOA	Low Volatility Oxygenated Organic Aerosol
nr	Non-Refractory
nrCl	Non-refractory Chloride
OA	Organic Aerosol
OC	Organic Carbon
O_x	Odd-Oxygen (O_3 + NO_2)
PACO	Pasadena Aerosol Characterization Observatory
PALMS	Particle Analysis by Laser Mass Spectrometry
PILS-IC	Particle-into-Liquid Sampling and Ion Chromatography
PM_1, $PM_{2.5}$	Particulate matter below 1 μm and 2.5 μm size cuts, respectively.
PMF	Positive Matrix Factorization
POA	Primary Organic Aerosol
PToF	Particle Time-of-Flight
RDI	Rotating Drum Impactor
RH	Relative Humidity
rBC	Refractory Black Carbon
rCl	Refractory Chloride (as measured by XRF)
SMPS	Scanning Mobility Particle Sizer
SOA	Secondary Organic Aerosol
SOAR	Study of Organic Aerosol at Riverside Campaign
SP2	Single Particle Soot Photometer
SP-AMS	Soot Particle Aerosol Mass Spectrometer
SV-OOA	Semi-Volatile Oxygenated Organic Aerosol
UHSAS	Ultra-High Sensitivity Aerosol Spectrometer
VMT	Vehicle Miles Traveled
WSOC	Water-Soluble Organic Carbon
XRF	X-ray Fluorescence

Appendix A: CalNex Pasadena Ground Site Meteorology & Back-Trajectories

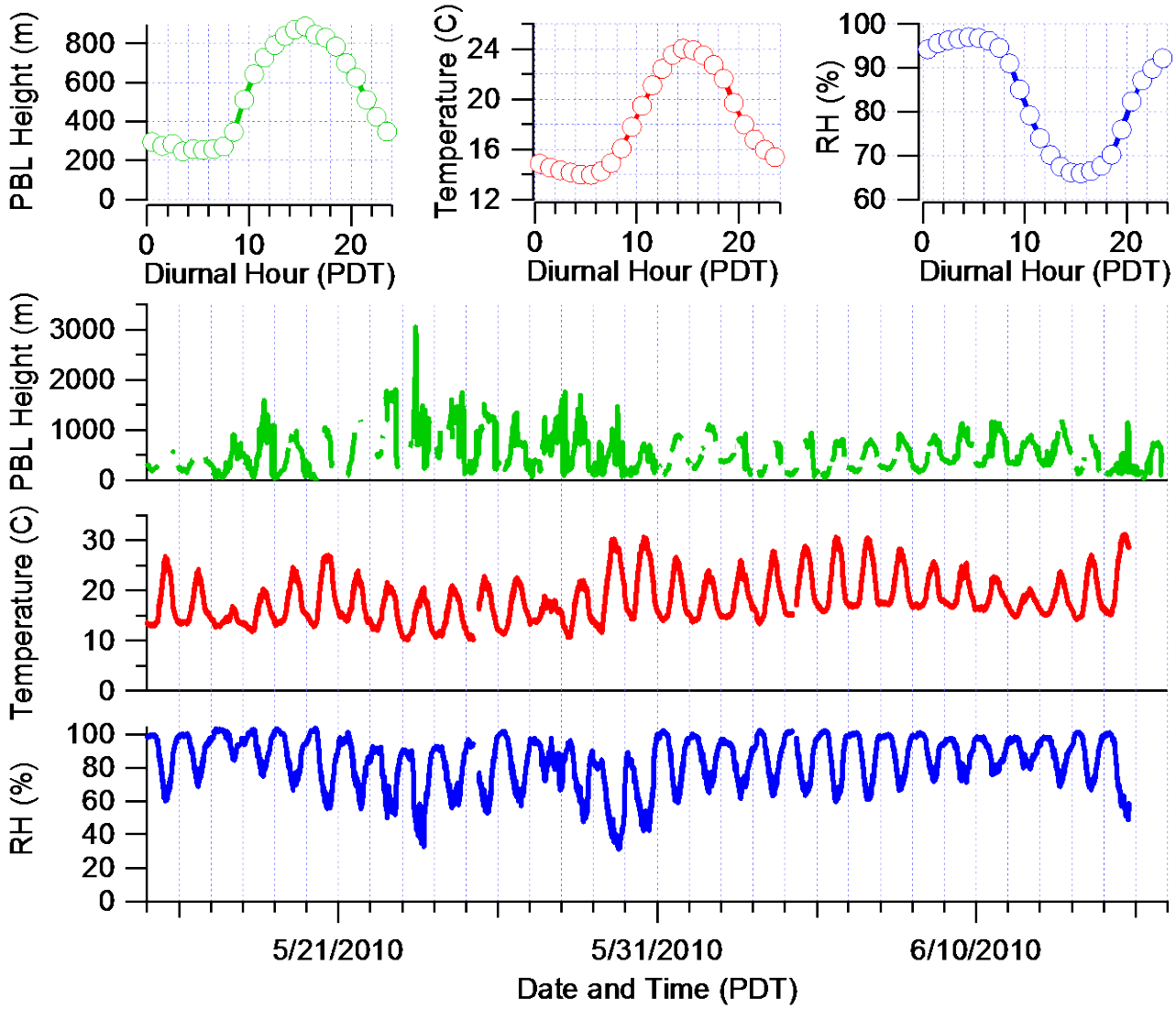

Figure A-1: Time series and diurnal profiles for planetary boundary layer height (PBL), temperature and relative humidity at the Pasadena ground site during CalNex.

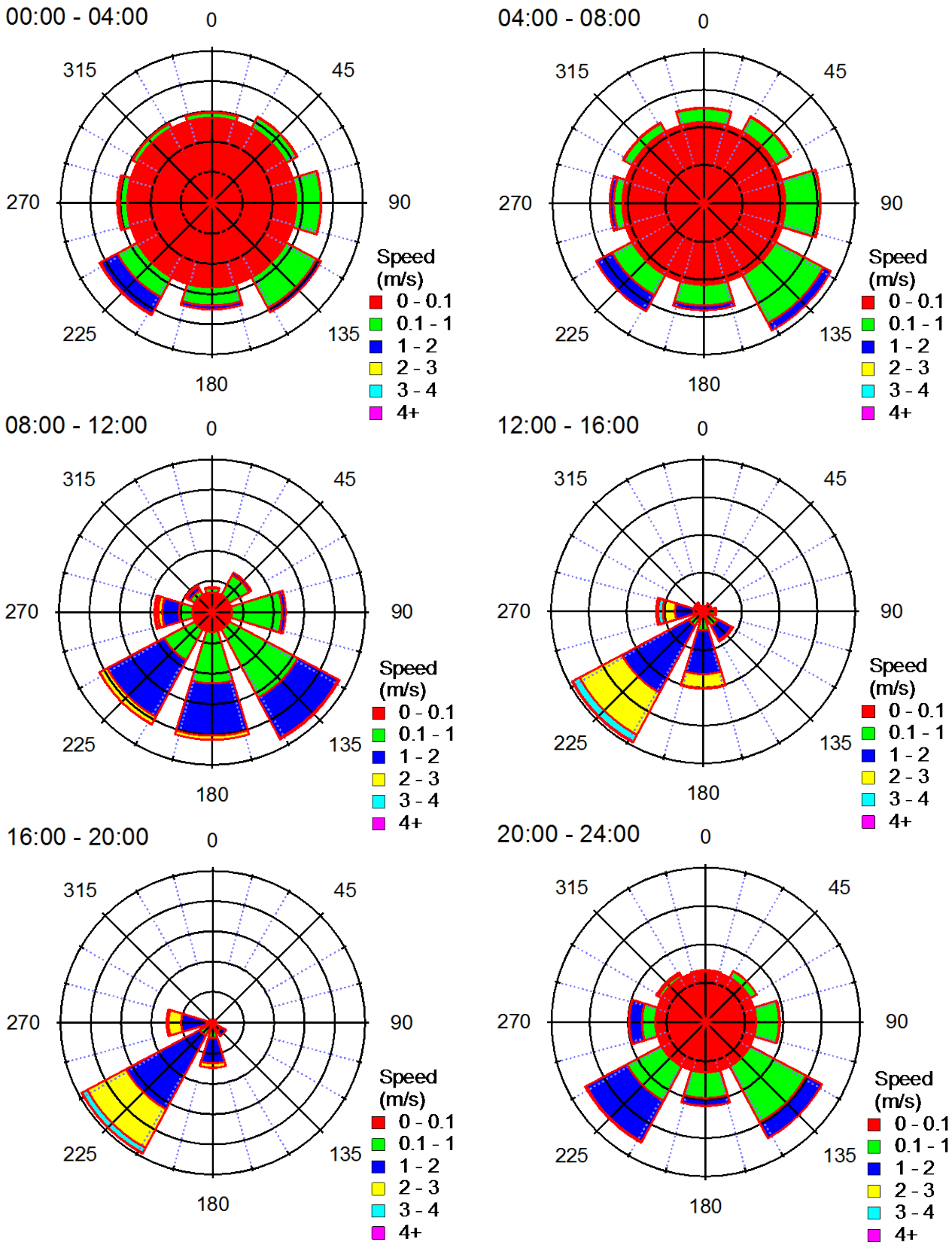

Figure A-2: Wind roses for the Pasadena ground site during CalNex organized by time of day (PDT). Zero on the polar coordinate is north and radial distance indicates relative frequency.

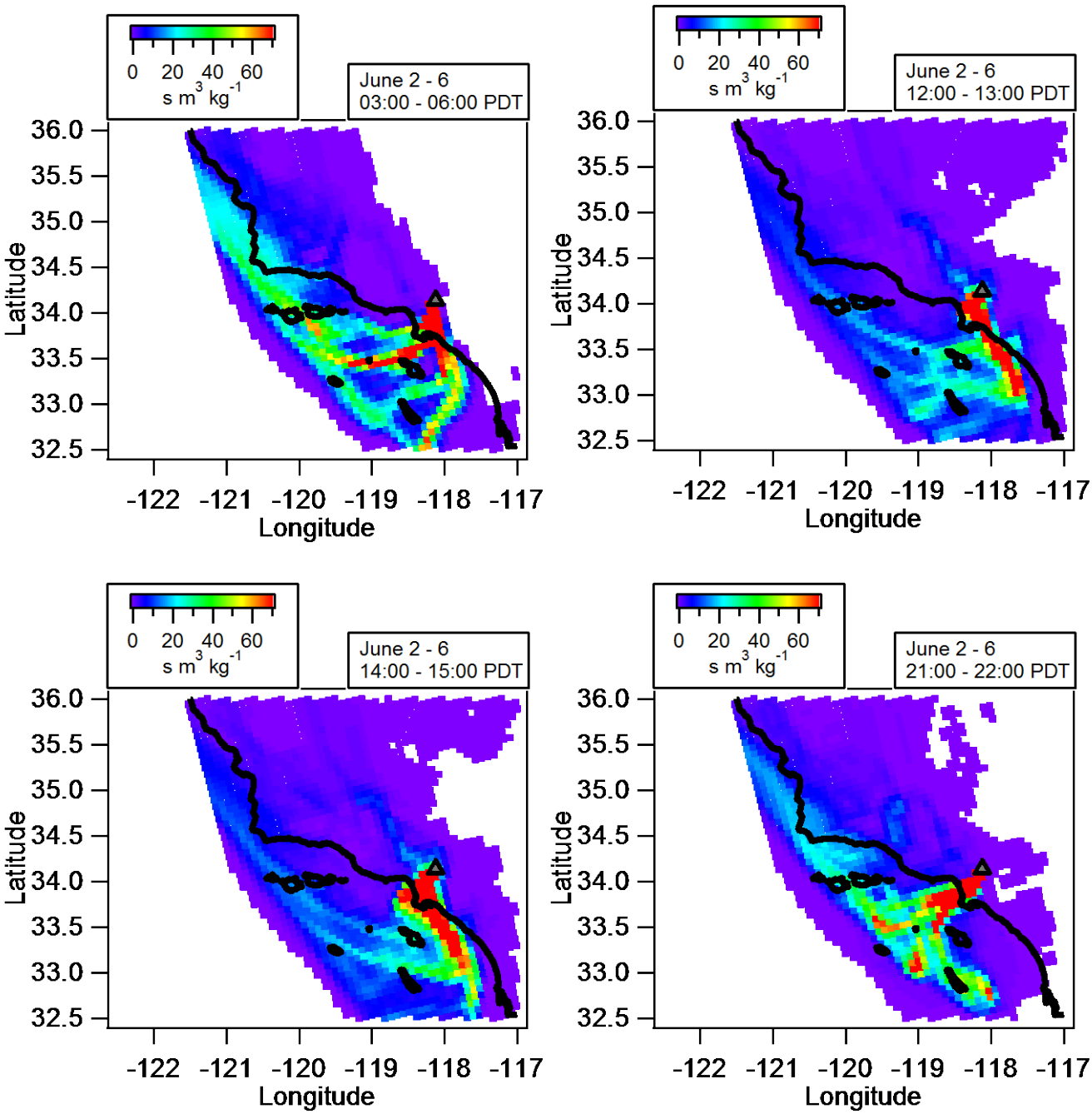

Figure A-3: Average 48 h FLEXPART back-trajectories for air masses arriving at the Pasadena ground site. Colors represent the footprint residence times. Each panel corresponds to a different time-of-day and is the average for June 2nd through June 6th. The grey triangle indicates the location of the Pasadena ground site.

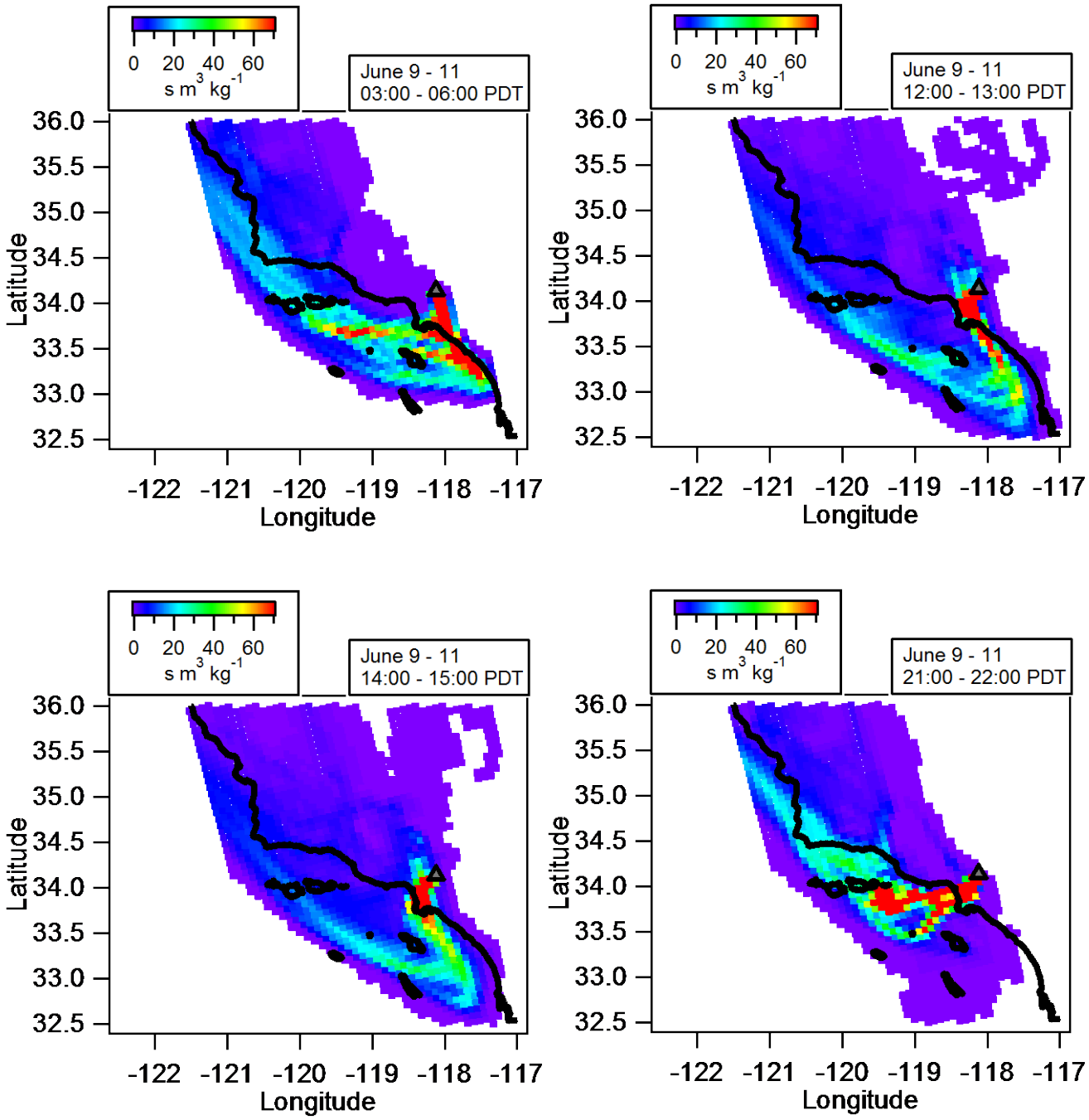

Figure A-4: Average 48 h FLEXPART back-trajectories for air masses arriving at the Pasadena ground site. Colors represent the footprint residence times. Each panel corresponds to a different time-of-day and is the average for June 9th through June 11th. The grey triangle indicates the location of the Pasadena ground site.

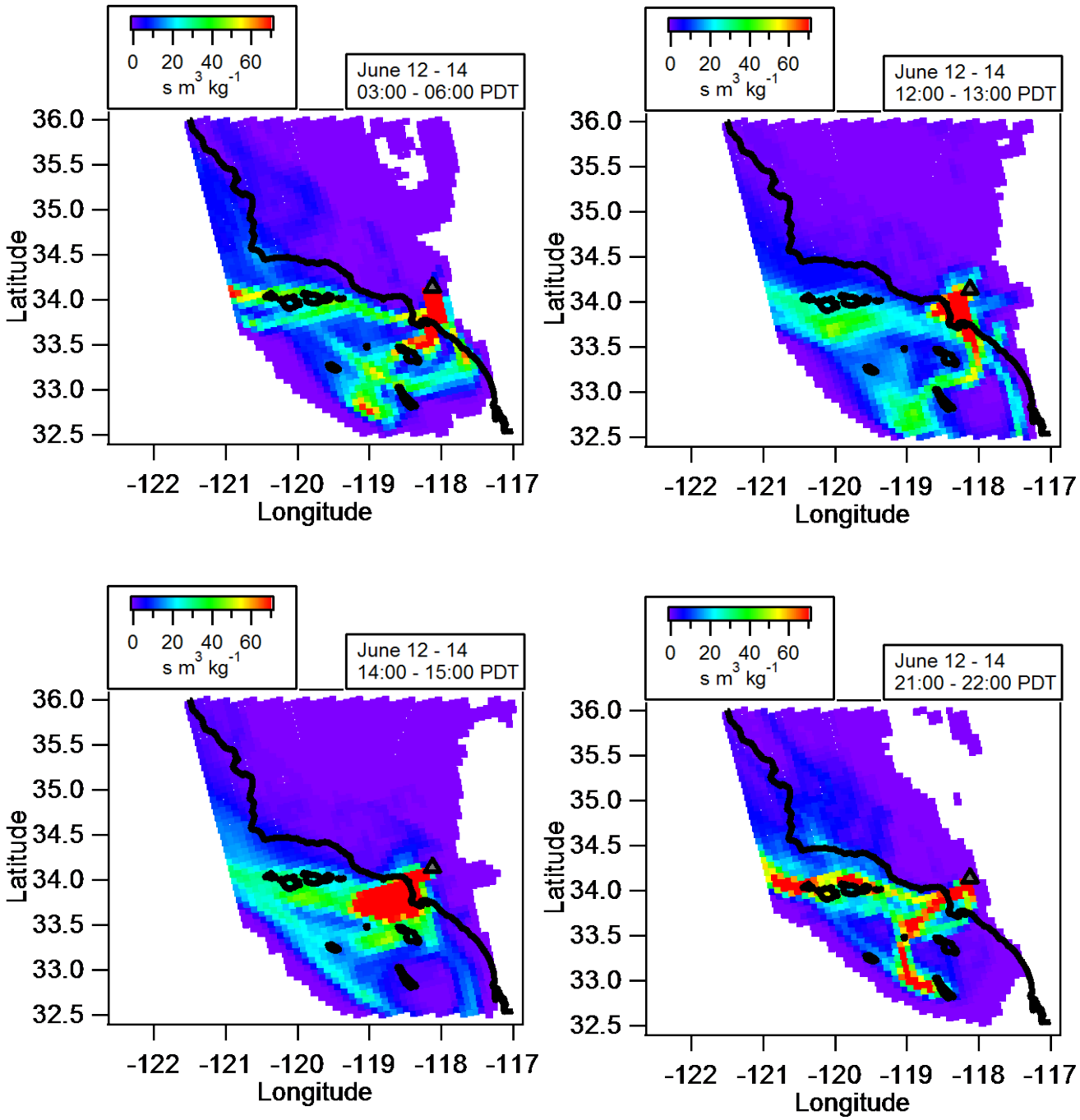

Figure A-5: Average 48 h FLEXPART back-trajectories for air masses arriving at the Pasadena ground site. Colors represent the footprint residence times. Each panel corresponds to a different time-of-day and is the average for June 12th through June 14th. The grey triangle indicates the location of the Pasadena ground site.

Appendix B: Instrument Comparisons & Selected Diagnostics

This appendix provides information that supports the validity of the AMS measurements. In Figure B-1 the time series of submicron aerosol mass concentration measured by the AMS and calculated from the SMPS and UHSAS number distributions are shown along with correlation plots for the various instruments. (Note: the UHSAS number distribution was determined using a refractive index of 1.515, which corresponds to dry ammonium sulfate at 1050 nm.) The AMS only measures non-refractory aerosol, and to partially compensate for this limitation the rBC concentration from the SP2 is added to the AMS time series. The AMS also does not measure mass from other refractory sources such as sea salt or mineral dust. These species are not expected to significantly impact the instrument comparison though, because the the relative amount of the non-EC refractory mass is less than 5% of the total PM_1 aerosol mass (Figure 2A in main text). Similarly, the PALMS instrument quantified the sum of mineral/road dust and sea salt to be 9% of total submicron volume, respectively. The AMS and SMPS instruments show good agreement, and a linear regression analysis of the two data results in a slope of 1.03 (R^2 = 0.85) as shown in Panel C. The agreement between the AMS and UHSAS is not as good (slope = 1.28, R^2 = 0.84) when the UHSAS data is truncated at 740 nm geometric diameter to approximate the 1 □m aerodyna
the reasonable agreement between the AMS and SMPS as well as other instruments (see below), it appears that the UHSAS, including the uncertainties in the conversion to volume and the estimation of refractive index, may be responsible for this discrepancy. It is noted that from 6/4 through 6/6 there are extended periods when the AMS measurement is lower than both the SMPS and UHSAS. This period exhibits an unusually large amount of mass above 740 nm (estimated geometric diameter, equivalent to an estimated vacuum aerodynamic diameter of 1080 nm) as measured by the UHSAS (Panel B). Similarly, PALMS measurements show a large volume concentration of SO_4/OA/NO_3 particles above 784 nm geometric diameter during this period (Figure 4 in main paper). The discrepancy from 6/4 through 6/6 is therefore attributed to a period of unusually large particles, which are near and above the 1 □m aerodyna
size cut for measurement by the AMS.

The SMPS measurements are also validated by calculating the Mie scattering from the number size distribution data, and then comparing the result against extinction measurements (Figure B-2). The extinction measurements are from the CAPS instrument and were taken at 532 and 630 nm. Good agreement between the calculated scattering and measured extinction is observed when using an index of refraction 1.54, which is the average for dry ammonium sulfate and ammonium nitrate [*Kleinman et al.*, 2007]. The refractive index of OA will vary depending on composition, but an average value of 1.55 is often assumed when predicting optical properties [*Dick et al.*, 2007; *Kleinman et al.*, 2007]. The particles were dried before measurements by the SMPS and CAPS. The amount of black carbon at the site is relatively small, and thus, scattering dominates the aerosol extinction [*Thompson et al.*, 2012], which allows for the direct comparison of calculated scattering and measured extinction performed here.

To further examine the AMS data, the concentrations of nitrate and sulfate aerosols measured by the AMS and the PILS-IC instrument were compared (Figure B-3). An important consideration when carrying out this comparison is that the PILS-IC was equipped with a $PM_{2.5}$ inlet, which transmits larger particles that cannot be measured AMS. For sulfate the agreement is generally good, and a linear ODR regression analysis of the two data sets results in a best-fit slope of 1.01 (R^2 = 0.84). The same analysis for nitrate results in a slope of only 0.64 (R^2 =

0.85), however. A possible explanation for the discrepancy between the nitrate measurements is the presence of super-micron sodium nitrate that is formed when sea salt reacts with nitric acid as discussed in Section 3.I.B of the main text. To test this hypothesis, the regression analysis for nitrate was repeated using only periods with PALMS sea salt volume concentrations of less than 0.35 $\mu m^3\ cm^{-3}$, which corresponds to the 5th percentile of the data. A substantial improvement in agreement is observed with the slope increasing to 0.89 (from 0.64). For the sake of completeness the same test was performed on the sulfate data, but there is only a small increase in the slope to 1.09 (from 1.01). Interestingly, the excellent agreement between the PILS-IC and AMS sulfate, as well as the weak dependence on PALMS sea salt concentrations in the scatter plot, suggests that little sodium sulfate has been formed from the reaction of sea salt and sulfuric acid. Despite the technical differences between the AMS and PILS-IC, after accounting for the presence of sodium nitrate in the supermicron mode there is reasonable agreement between these two instruments with respect to sulfate and nitrate concentrations.

The comparisons of the AMS organic mass (OM) with other measurements of organic aerosols at the Pasadena ground site exhibits reasonable agreement. The different OM and OC measurements are listed in Table B-1, and the results of the OM and OC comparisons are summarized Table B-2 and Figure B-4. In Panel A of Figure B-4 the AMS OM_1 (the subscript indicates the size cut in µm) and the online Sunset organic carbon mass ($OC_{2.5}$) are plotted together and a strong correlation between the two measurements is observed. The AMS OM_1 and online Sunset $OC_{2.5}$ data (Panel B) yield an R^2 value of 0.76, but the regression slope of 3.3 is significantly higher than the expected range of 1.4 – 2.3 [*Aiken et al.*, 2008; *Turpin and Lim*, 2001]. Such a large discrepancy is outside the AMS uncertainty bounds of ±30% [*Middlebrook et al.*, 2012]. While the exact reason for this discrepancy is unclear it may be related, at least partially, to the presence of a denuder upstream of the Sunset carbon analyzer. Specifically, the denuder may cause volatilization of particulate OC that is induced by re-equilibration of organic concentrations after removal of vapor-phase organics by the denuder [*Grover et al.*, 2008]. It also should be noted that, as discussed in the paragraph below, the AMS OC_1 displays about a 10 – 20% difference with respect to the filter-based $OC_{2.5}$ measurements, which may also explain a portion of the discrepancy at a level consistent with known AMS uncertainties.

A scatter plot of the AMS OM_1 versus the $OC_{2.5}$ measured from two sets of filter samples collected by the Georgia Institute of Technology (GIT) and U.S. Environmental Protection Agency (EPA) groups (Panel C) yields very reasonable slopes of 1.7 and 1.9 (R^2 = 0.82 and R^2 = 0.80, respectively). These slopes are similar to the OM_1:OC_1 of 1.7 that was determined from the elemental analysis of the AMS mass spectra. The $OC_{2.5}$ concentration was also measured on a third set of filter samples collected by the University of North Carolina (UNC) group. For the UNC $OC_{2.5}$ measurement the slope obtained from the regression analysis (Panel D) is 1.4, which is lower than the other filter samples. This difference seems to be related to the collection times for the filter samples. The UNC samples included several intensive sampling periods of 6 h or less, whereas the GIT and EPA filters were switched daily. If only the daily UNC samples are included in the regression analysis a slope of 1.8 is obtained, which is similar to the GIT and EPA samples. The AMS OM_1 and the FTIR $OM_{2.5}$ obtained from filter samples are compared in Panel E resulting in a regression slope of 1.3 (R^2 = 0.63). Both the filters analyzed by FTIR as well as the UNC filters exhibit higher amounts of organics relative to the 24 hr filters when the collection times are shorter, which is likely due to evaporation losses of semi-volatiles from the daily samples [*Russell et al.*, 2009a]. Furthermore, high temperatures on the asphalt-coated roof

where the filter samplers were located may have increased the influence of evaporation. It should be noted that all the analyses are for $PM_{2.5}$ particles except the AMS, which is a PM_1 instrument. The impact of the different size cuts on the comparison can be evaluated by estimating that 15% of the $PM_{2.5}$ organic mass is present between 1 and 2.5 □m on avera determined from online Sunset OC measurements that were performed while switching between a $PM_{2.5}$ and PM_1 cyclone from 6/12 through 6/16. Accounting for this additional mass that is not measured by the AMS would increase the slopes for the regression analyses, but the corrected values for the GIT, EPA, and UNC filter samples would still fall within the expected range of 1.2 – 2.2 for OM/OC (the expected 1.7 value with a ±30% uncertainty range for the AMS, and neglecting the uncertainty of the OC measurements).

For completeness, the slopes from linear ODR regression analyses for each possible pairing of OM or OC measurements are summarized in Table B-2 along with R^2 values. The AMS measurements of OM_1 are converted to OC_1 using the OM:OC ratios determined from the elemental analysis of the AMS mass spectra. The AMS and all of the filter $OC_{2.5}$ measurements (GIT, EPA, UNC) are in agreement within the uncertainties, exhibiting slopes between 0.81 and 1.14 and R^2 values higher than 0.60. The lowest correlations are for comparisons with the UNC filter samples, which is likely due to different slopes observed in the regression analyses for the 24 h versus intensive UNC sampling periods. If comparing only 24 h $OC_{2.5}$ data from the UNC group against the AMS as well as the EPA and GIT filter samples, then all the R^2 values are higher than 0.78. The online Sunset $OC_{2.5}$ measurement shows good correlation with the AMS and the filter OC measurements ($R^2 \geq 0.75$), but it is systematically lower by about a factor of two against all other measurements, which might be due to the denuder utilized in the online Sunset $OC_{2.5}$ measurement as described in the preceding paragraph. Alternatively, the un-denuded $OC_{2.5}$ filter samples may be impacted by a positive artifact due to adsorbing volatile organic gases, although the agreement between the online AMS OC_1 and offline filter $OC_{2.5}$ indicates that this positive artifact is not impacting other comparisons. Lastly, when comparing the 24 h FTIR $OM_{2.5}$ against the 24 h GIT and EPA filter $OC_{2.5}$ the slope is considerably lower than the expected OM:OC ratio, although the correlation between the measurements is reasonable ($R^2 \geq 0.52$). One possible reason for the low FTIR $OM_{2.5}$ concentrations may be that the evaporation of organics from the FTIR samples was more extensive. The UNC filter $OC_{2.5}$ shows better agreement with the FTIR $OM_{2.5}$ results (FTIR $OM_{2.5}$: UNC $OC_{2.5}$ = 1.29, $R^2 \geq 0.76$), which is expected since these samplers were located closer to each other on the Keck Building rooftop, and both analyses included intensive samples. Selecting only the intensive periods slightly improves the best-fit slope in the regression analysis (1.33 vs. 1.29). As discussed above the AMS OM_1 and FTIR $OM_{2.5}$ agree reasonably well although the FTIR $OM_{2.5}$ is somewhat lower (AMS OM_1 : FTIR $OM_{2.5}$ = 1.25, $R^2 \geq 0.63$). This observation is consistent with previous comparisons that have shown FTIR measurements tend to be lower than and less correlated with AMS measurements when carried out in urban areas [*Russell et al.*, 2009b].

The fraction of organic signal at *m/z* 44, termed f_{44}, is often taken as an indicator of relative oxygen content because in ambient measurements *m/z* 44 is typically dominated by the CO_2^+. The scatter plot of O/C and f_{44} shown in Figure B-5 confirms this relationship for Pasadena during CalNex. Figure B-5 also includes the best-fit lines determined from regression analyses of the CalNex data as well as for Riverside and Mexico City. All three lines are similar, which supports the validity of the AMS measurements for Pasadena and provides a sample of the variability of the O/C to f_{44} relationship across different field sites and time periods.

Table B-1: Summary of the different OM and OC measurements taken on the Caltech campus during the CalNex campaign (GIT = Georgia Institute of Technology, EPA = U.S. Environmental Protection Agency, UNC = University of North Carolina). Note: the intensive periods for the UNC Filter OC and FTIR OM coincided.

	Online/Offline?	Location	Dates for Sampling	Number of Samples	Time Resolution	Size Cut
AMS	Online	Ground Site	5/15-6/15	3681	2.5 min	PM_1
Sunset Online OC	Online	Ground Site	5/15-6/15	775	44 min	$PM_{2.5}$
GIT Filter OC	Offline	Keck Roof	5/15-6/15	31	23 h	$PM_{2.5}$
EPA Filter OC	Offline	Keck Roof	5/15-6/15	32	23 h	$PM_{2.5}$
UNC Filter OC	Offline	Keck Roof	5/15-6/13	58	23 h, or 3-6 h	$PM_{2.5}$
FTIR OM (Scripps)	Offline	Keck Roof	5/15-6/15	57	23 h, or 3-6 h	$PM_{2.5}$

Table B-2: Slopes and correlation coefficients for regression analyses of various OM and OC measurements located on the CalTech campus during CalNex (GIT = Georgia Institute of Technology, EPA = U.S. Environmental Protection Agency, UNC = University of North Carolina). *Note:* FTIR results correspond to FTIR OM data, while all other data sets are exclusively OC.

Slope	AMS OC_1	FTIR $OM_{2.5}$ (Scripps)	Online Sunset $OC_{2.5}$	GIT Filter $OC_{2.5}$	EPA Filter $OC_{2.5}$	UNC Filter $OC_{2.5}$	(y data)
AMS OC_1							
FTIR $OM_{2.5}$ (Scripps)	1.25[a]						
Sunset Online $OC_{2.5}$	1.95	3.13					
GIT Filter $OC_{2.5}$	0.99	0.83	0.48				
EPA Filter $OC_{2.5}$	1.13	0.99	0.56	1.14			
UNC Filter $OC_{2.5}$	0.81	1.29	0.41	1.12	0.88		
(x data)							

R^2	AMS OC_1	FTIR $OM_{2.5}$ (Scripps)	Online Sunset $OC_{2.5}$	GIT Filter $OC_{2.5}$	EPA Filter $OC_{2.5}$	UNC Filter $OC_{2.5}$
AMS OC_1						
FTIR $OM_{2.5}$ (Scripps)	0.63[a]					
Sunset Online $OC_{2.5}$	0.75	0.49				
GIT Filter $OC_{2.5}$	0.78	0.52	0.86			
EPA Filter $OC_{2.5}$	0.78	0.55	0.82	0.93		
UNC Filter $OC_{2.5}$	0.76	0.76	0.75	0.75	0.60	

[a]The AMS vs. FTIR comparison is for OM vs. OM.

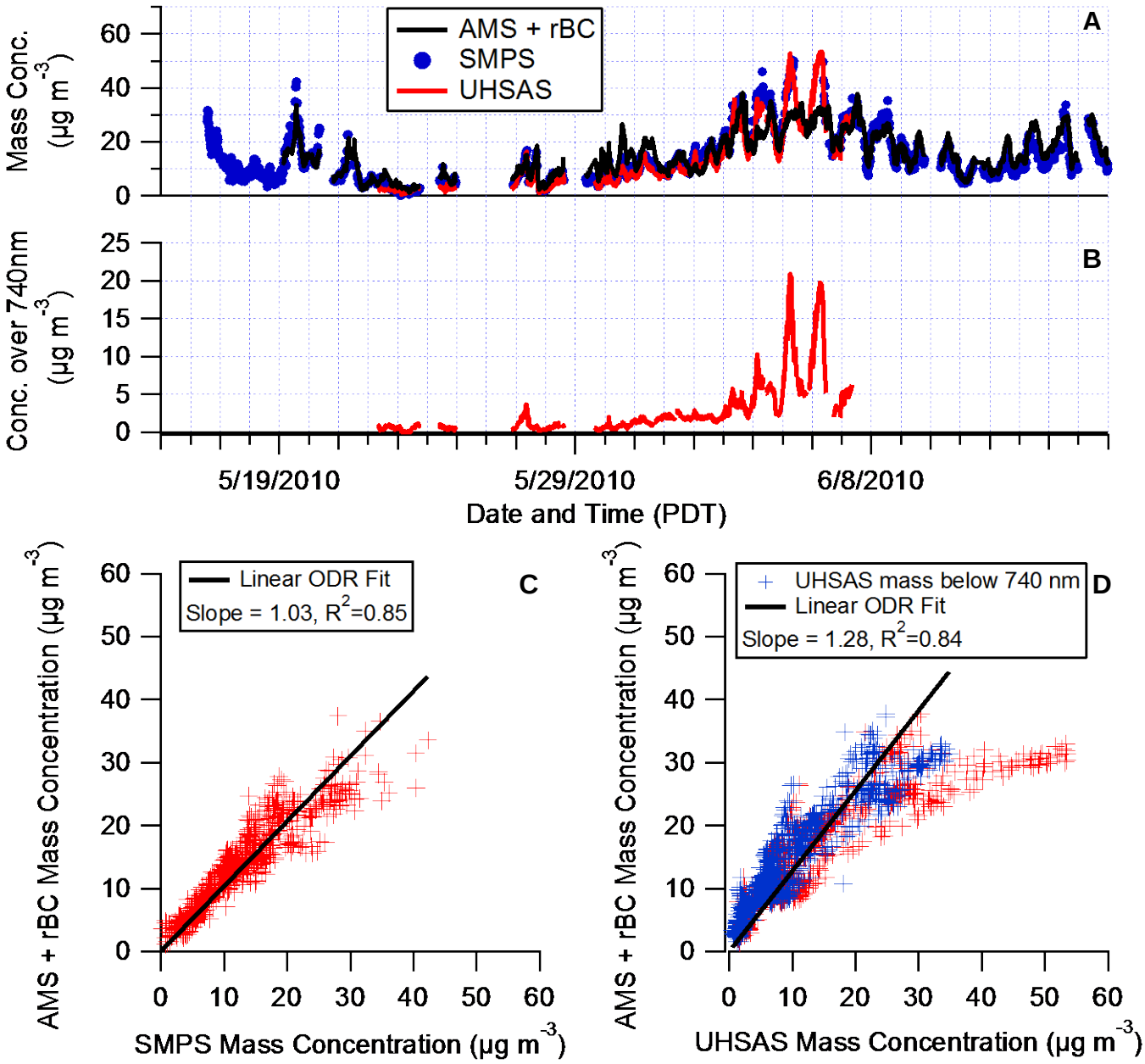

Figure B-1: (A) Time series of mass concentrations as measured by the AMS, SMPS, and UHSAS. rBC from the SP2 has been added to the AMS time series. The SMPS and UHSAS mass concentrations are calculated using the estimated particle density, which is obtained from the AMS composition and rBC measurements [*Q Zhang et al.*, 2005]. **(B)** The mass over 740 nm estimated geometric diameter, equivalent to ~1080 vacuum aerodynamic diameter, as measured by the UHSAS. **(C)** Scatter plot of the AMS plus rBC versus SMPS mass concentrations with linear fit. **(D)** Scatter plot of the AMS plus rBC versus UHSAS mass concentrations. The total UHSAS mass (red markers) and the UHSAS mass for particles less than 740 nm in geometric diameter (blue markers) are displayed. The linear fit corresponds to the UHSAS mass below 740 nm geometric diameter.

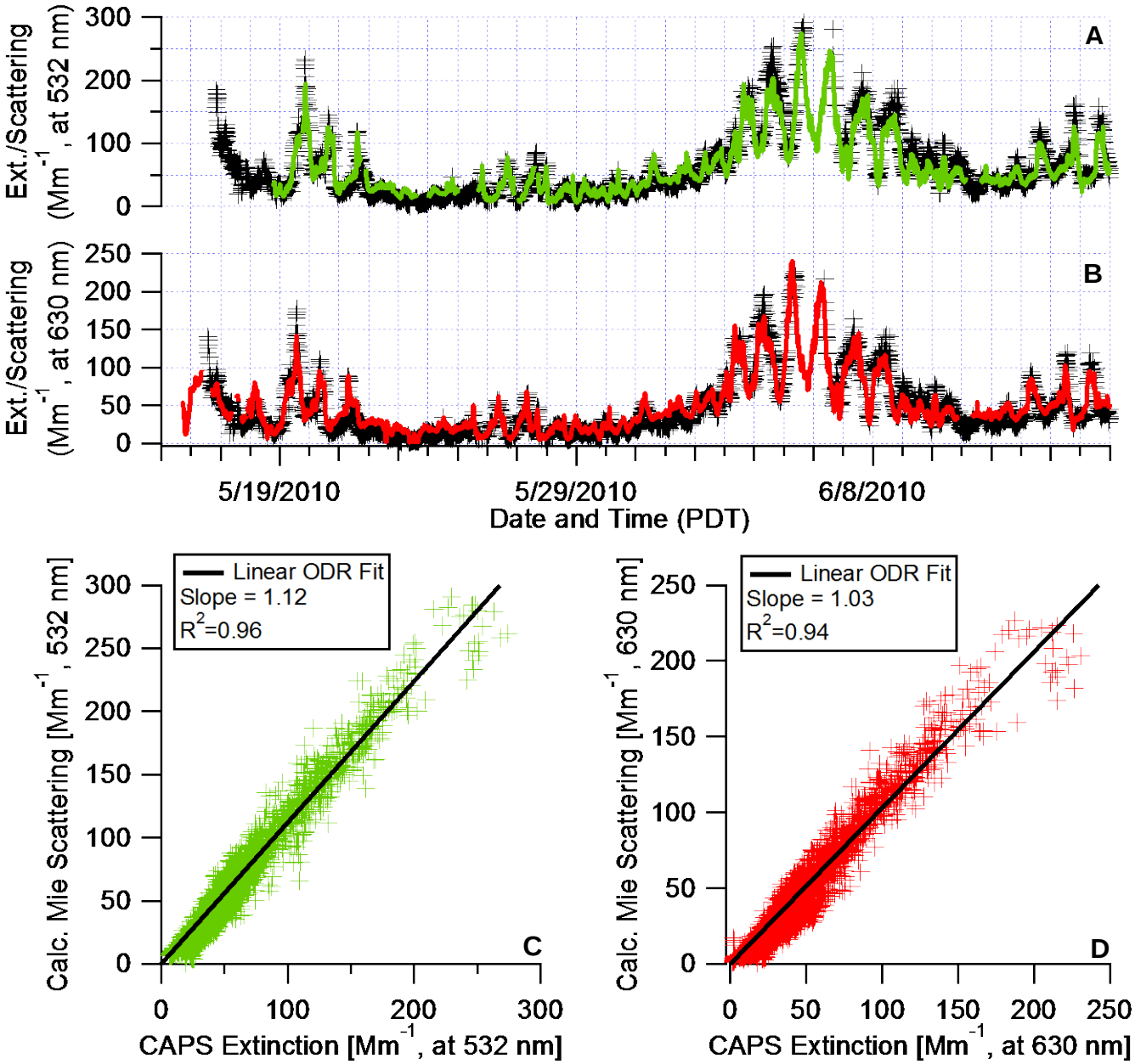

Figure B-2: (A) Time series of extinction measured by the CAPS instrument and Mie scattering calculated from SMPS data. Both traces correspond to a wavelength of 532 nm, and the Mie scattering was calculated using a refractive index of 1.54, which is the average for $(NH_4)_2SO_4$ and NH_4NO_3 [*Kleinman et al.*, 2007]. **(B)** Time series of CAPS extinction and calculated Mie scattering. Both traces correspond to a wavelength of 630 nm, and the Mie scattering was calculated using the same index of refraction (1.54). **(C)** Scatter plot of calculated Mie scattering and CAPS extinction for 532 nm with a linear fit of the data. **(D)** Scatter plot of calculated Mie scattering and CAPS extinction for 630nm with a linear fit of the data.

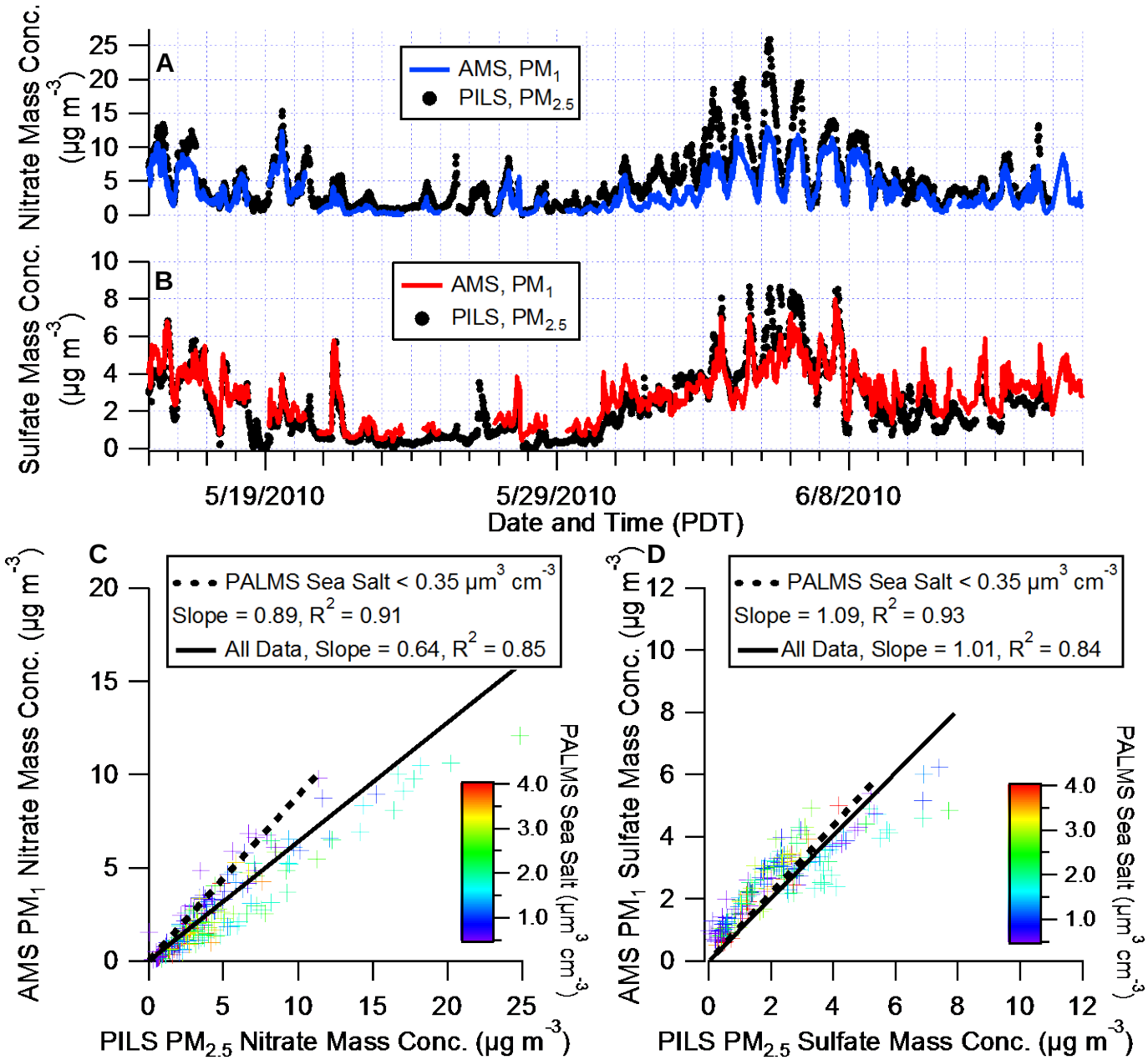

Figure B-3: (A) Time series of nitrate mass concentration measured by the AMS and the PILS-IC instrument. **(B)** Time series of sulfate mass concentration measured by the AMS and the PILS-IC instrument. **(C)** Scatter plot of the AMS and PILS-IC nitrate mass concentrations. Linear fits are shown for the entire data set (solid line), and also for selected periods with low PALMS sea salt concentrations (dashed line). **(D)** Scatter plot of the AMS and PILS-IC sulfate mass concentrations. Linear fits are shown for the entire data set (black solid line), and also for periods with low PALMS sea salt concentrations dashed line). The PALMS data corresponds to a $PM_{2.5}$ size cut.

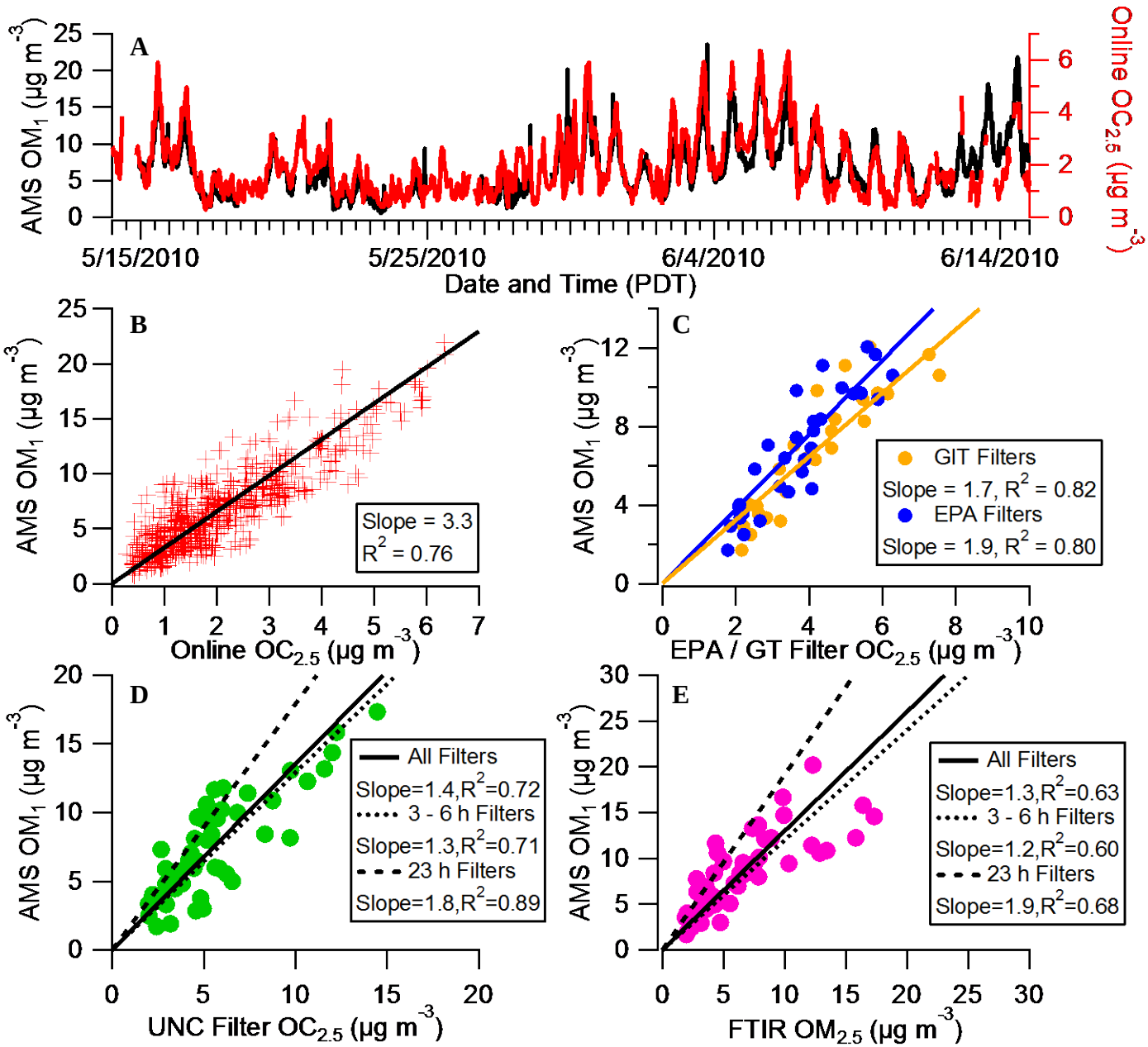

Figure B-4: (A) Times series of the OM_1 measured by the AMS and the $OC_{2.5}$ measured online by the Sunset Labs OC/EC analyzer. **(B)** Scatter plot of the AMS OM_1 versus the online Sunset $OC_{2.5}$. **(C)** Plot of the AMS OM_1 versus the $OC_{2.5}$ measured using two sets of filter samples collected by the Georgia Institute of Technology group (gold) and the EPA group (blue). **(D)** Plot of the AMS OM_1 versus the $OC_{2.5}$ measured from the UNC group filter samples. **(E)** Plot of the AMS OM_1 versus the $OM_{2.5}$ determined from FTIR measurements. The lines in Panels B – E represent linear fits of the data. Subscripts indicate measurement size cut in µm and for aerodynamic diameter.

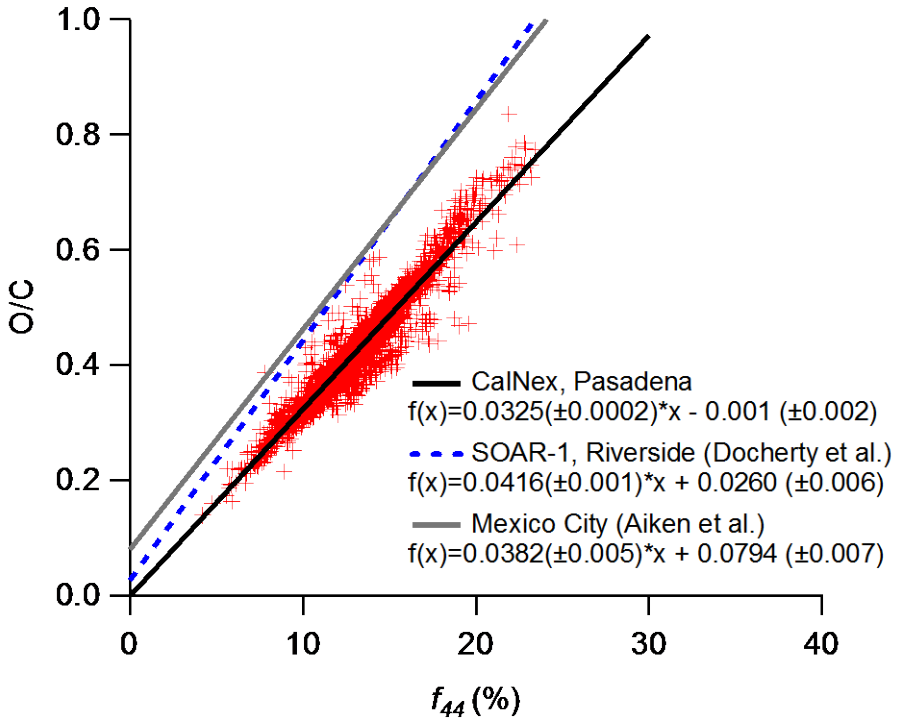

Figure B-5: Scatter plot of f_{44} versus O/C calculated from HR-ToF-AMS high resolution data. A linear ODR fit of the CalNex data is shown along with the similar results from Riverside, CA [*Docherty et al.*, 2011] and Mexico City [*Aiken et al.*, 2008].

Appendix C: Selection of PMF solution & Additional PMF Figures

This appendix describes the process for selecting the 5-component PMF solution that is described in the main text. An in-depth description of PMF and its application to AMS data is not included here as it has already been provided in previous publications [*Paatero and Tapper*, 1994; *Ulbrich et al.*, 2009], and instead we focus on the specific analysis of the CalNex data set. The selection of the solution was based on the mass spectral profiles, the time series, diurnal cycles, and the correlations of the components with time series for tracer species. Panel A of Figure C-1 summarizes the types and mass fractions of the different components identified as the number of components is systematically increased from 3 to 10 (for FPeak=0). The 3-component solution is similar to that found for PMF analyses of other data sets with HOA, SV-OOA, and LV-OOA components identified. If the number of components is increased to four, then CIOA is also resolved. The mass fraction of HOA is substantially reduced in the 4-component solution compared to the 3-component solution. Furthermore, HOA in the 3-component solution exhibits a unique evening peak, and in the 4-component solution CIOA displays this peak instead of HOA. Together these observations suggest that a large portion of the CIOA mass is classified as HOA in the 3-component solution. We conclude that the CIOA component is distinct from the other components, and in particular HOA, based on it substantially different diurnal cycle (Figure 7A), and the dramatic improvement in the correlation of HOA with rBC (R increases from 0.55 to 0.72) when increasing the number of components to four. This conclusion is further supported by the mass spectra as discussed in this section below.

Increasing the number of components to five leads to a third OOA component, but it is unclear if the additional component represents a different type of OOA given the lack of unique correlations with tracers. In contrast, at six components LOA is resolved, which is clearly distinct from the previously identified components. The LOA component is nitrogen-rich, and has a substantially different time series (Figure 6). As described in the main text the LOA mass spectra is distinguished by prominent fragments that are characteristic of amines: CH_4N^+ (*m/z* 30), $C_2H_4N^+$ (*m/z* 42), $C_3H_6N^+$ (*m/z* 56), $C_3H_8N^+$ (*m/z* 58), $C_5H_{10}N^+$ (*m/z* 84), $C_5H_{12}N^+$ (*m/z* 86). The sum of the absolute residuals associated with these amines is plotted versus number of components in Panel B of Figure C-1. This residual decreases with the number of components, but the decrease is largest between the five-component and six-component solutions. In addition, there is only a slight decrease in the residuals when increasing the number of components beyond six. Clearly, LOA in the 6-component solution is needed for PMF to properly account for amines in OA measured at the Pasadena ground site.

For PMF solutions with more than 6 components interpretation becomes increasingly difficult. Numerous oxygen-rich components are identified, which could be classified as OOA. Unique correlations to identify separate sources for these components are not found though. A key limitation of PMF analysis is the assumption of a constant mass spectrum for each component. Thus, it is possible that the variable nature of the SOA spectrum with, for instance, photochemical age leads to significant residuals in PMF, and when increasing the number of components beyond six these residuals control the additional components in the PMF solution, leading to more 'OOA' components [*Ulbrich et al.*, 2009].

In this analysis it would be helpful to resolve the LOA component while at the same time limiting the number of OOA components to two, SV-OOA and LV-OOA, to facilitate comparison with previously published research where typically one or two OOA components are

identified. As described above, it is also unclear if the additional OOA components (i.e., beyond SV-OOA and LV-OOA) represent distinct sources or chemical types. Specifically, for the 6-factor solution two of the three OOA components exhibit a high correlation in time (R=0.77), which further suggests these two components may not be distinct. To address these concerns, the PMF analysis is repeated after subtracting out the contribution of LOA to the mass spectral matrix. The LOA contribution is determined from the 6-component solution of the original PMF analysis, and is included when summarizing the final PMF results. Thus, this method is equivalent to constraining LOA to have a time series and mass spectrum that is invariant as the number of component in increased [*Lanz et al.*, 2008]. It should be noted that the LOA contribution to the total OA mass is small. Also, LOA exhibits a time series and mass spectra that contributes significantly to the PMF residual and is quite different from the other components. Thus, subtracting the LOA contribution only has a weak influence on the PMF solutions.

In Panel C, the mass fraction and identities of the components are summarized for the PMF analysis with the fixed LOA contribution. The 5-component solution is the final solution described in the main text. Similar to the original PMF analysis, a dramatic increase in the correlation of HOA and rBC is observed when the CIOA component is resolved in the 5-component solution (Panel D), and subsequent increases in the number of components either marginally increase or decrease this correlation. This observation is consistent with concluding that CIOA is distinct from the other components. In addition, the 6-component solutions for the two PMF analyses are similar, which is expected since the LOA contribution in both analyses is identical. The similarity indicates that holding the LOA contribution fixed does not create unforeseen changes in the PMF analysis. The Q/Q_{exp} values for the various PMF solutions are shown in Panel D. Specifically for the final 5-component solution a reasonable value of 1.9 is obtained. A Q/Q_{exp} value near one indicates that the assumptions of the bilinear PMF model are appropriate and that the estimation of the errors for the input data is accurate. In future work, the PMF analysis will be used on a combination of data from ambient and thermally denuded samples to explore if additional components can be identified similar to Docherty et al. [2011].

Figure C-2 shows the value of Q/Q_{exp} as a function FPeak for the 5-component solution with the fixed LOA contribution. Minimum Q/Q_{exp} values are observed for FPeak equal to zero. In addition, the correlation of the HOA component time series with that of the external tracer rBC does not improve for non-zero FPeak values. Thus, the 5-component solution corresponding to FPeak = 0 is the final solution selected for further discussion in the main text. Additionally, Figure C-3 summarizes an analysis of the residuals for the final 5-component solution (with FPreak = 0).

It was recently shown by Mohr et al. [2011] that HOA and cooking organic aerosol can be distinguished by their relative values of AMS f_{55} and f_{57}, which represent the fraction of the total OA at *m/z* 55 and *m/z* 57, respectively. The differences in f_{55} and f_{57} between the two components are driven by the relative prominence of the oxygenated fragments $C_3H_3O^+$ and $C_3H_5O^+$ in the mass spectra of cooking organic aerosol. For the CalNex PMF solution, the mass spectrum of the CIOA component (Figure 6A) shows the presence of these fragments, and they represent a greater fraction of the signal at *m/z* 55 and *m/z* 57 for CIOA versus HOA. To further explore if the mass spectra of HOA and CIOA for CalNex are consistent with previously published studies, f_{55} versus f_{57} data for the two PMF components are plotted in Figure C-4A.

The lines in Figure C-4A are taken directly from Mohr et al. [2011] and represent linear fits of f_{55} versus f_{57} data from previously reported cooking organic aerosol and HOA PMF components as well as from cooking and traffic source emission studies. Also plotted in Figure C-4A is f_{55} versus f_{57} for the total time-resolved organic mass spectra after subtracting out the contribution of SV-OOA and LV-OOA (the axes are labeled with 'OOA sub' to indicate this subtraction) so the data reflects only contributions from primary components. The resulting data points are colored by the relative contribution of CIOA. The CIOA component lies along the line for cooking source emissions, consistent with the description of CIOA as 'cooking-influenced' aerosol. The HOA component at CalNex does not match the linear fits for HOA as well, but it does lie within the range of the raw values used for the regression analysis in Mohr et al. [2011]. Since the differences between CIOA and HOA in f_{55} versus f_{57} space are related to oxygenated fragments, it is possible that the higher HOA oxidation in our study may lead to changes in the HOA data points in this space and explain the difference between the CalNex HOA component and the linear fits from Mohr et al. [2011]. For the time-resolved data, when CIOA has a large contribution the data in f_{55} versus f_{57} space resembles cooking emission sources, whereas when the CIOA contribution is low the data more closely resemble the expected HOA values. This result supports the conclusion that the organic aerosol at the Pasadena ground site had substantial contributions from both primary combustion and cooking sources. In addition, the CIOA and HOA components contain spectral characteristics that are similar to analogous components and primary emissions from previous studies.

The time series of the PMF components can be further analyzed using an autocorrelation plot in which the correlation of each factor with itself is calculated for various time offsets. In this analysis species with high frequency fluctuations in concentrations (i.e., having many 'spikes' in their time series) will have a steep profile and vice versa. As seen in Figure C-4B the autocorrelation profiles of SV-OOA and LV-OOA are the flattest, which is consistent with the more regional nature of these components. Furthermore, the observation that the LV-OOA profile is less steep than SV-OOA supports the association of LV-OOA with aged secondary organic aerosol that is expected to vary in concentration on longer time scales than fresh secondary organic aerosol. In contrast, the HOA component has a steep profile at the shortest times and a flatter profile at longer times indicating that this component has both local and regional sources. This finding is not surprising given that some HOA is generated by local traffic in the Pasadena area, but HOA is also advected to Pasadena from other areas in the LA Basin. Interestingly, the CIOA component appears to be more dominated by local sources in comparison to HOA, which may be related to the lower wind speeds and reduced advection in the evenings when CIOA is highest in concentration. Alternatively, if the atmospheric lifetime of CIOA was shorter than HOA, then that would also result in a relatively steeper profile for CIOA. The autocorrelation data was reanalyzed for only daytime and nighttime periods (Figure C-4C and C-4D) to partially separate out the confounding variable of wind speed. Even for daytime periods only, CIOA appears to have a steeper profile compared to HOA, which indicates that lower wind speeds and reduced advection at night are not solely responsible for the steeper CIOA profile. As described previously, the LOA component time series varies rapidly with time, and thus displays the steepest profile in the auto-correlation plot, supporting the description of this factor as 'local' organic aerosol.

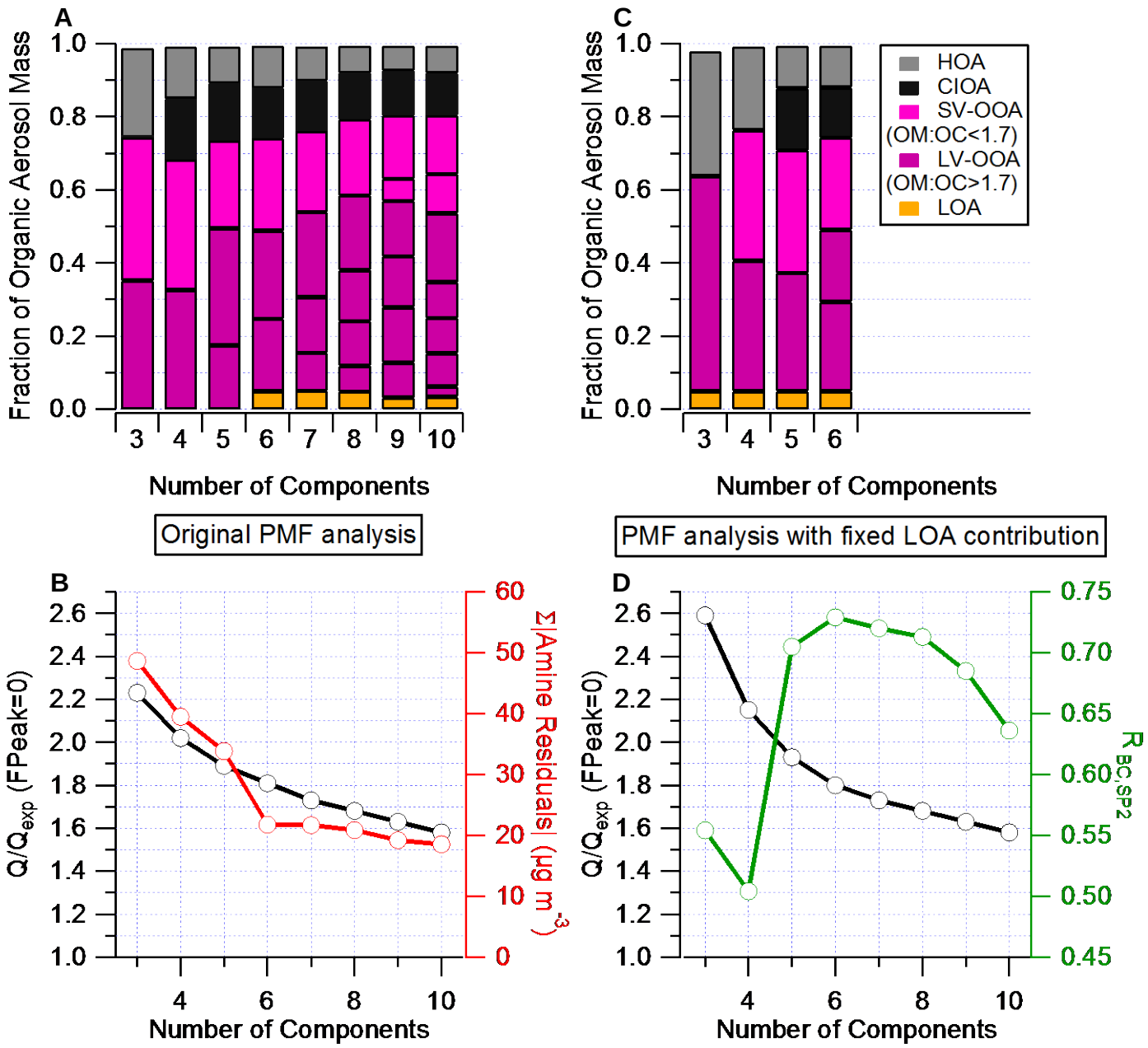

Figure C-1: (A) Stacked bar plot showing the relative contribution of each PMF component as a function of the number of components. **(B)** Q/Q_{exp} for the original PMF analysis (black line and markers) and the sum of the absolute values of the residuals for selected amine-containing ions (red line and markers). Both data traces are displayed as function of the number of components. **(C)** The relative contribution of each PMF component, similar to the figure on the top left, but for PMF solutions where the LOA contribution to the OA spectra is fixed. **(D)** Q/Q_{exp} for the PMF analysis with a fixed contribution from the LOA component versus number of components (black line with markers). The correlation of HOA with rBC is also displayed (green line and markers).

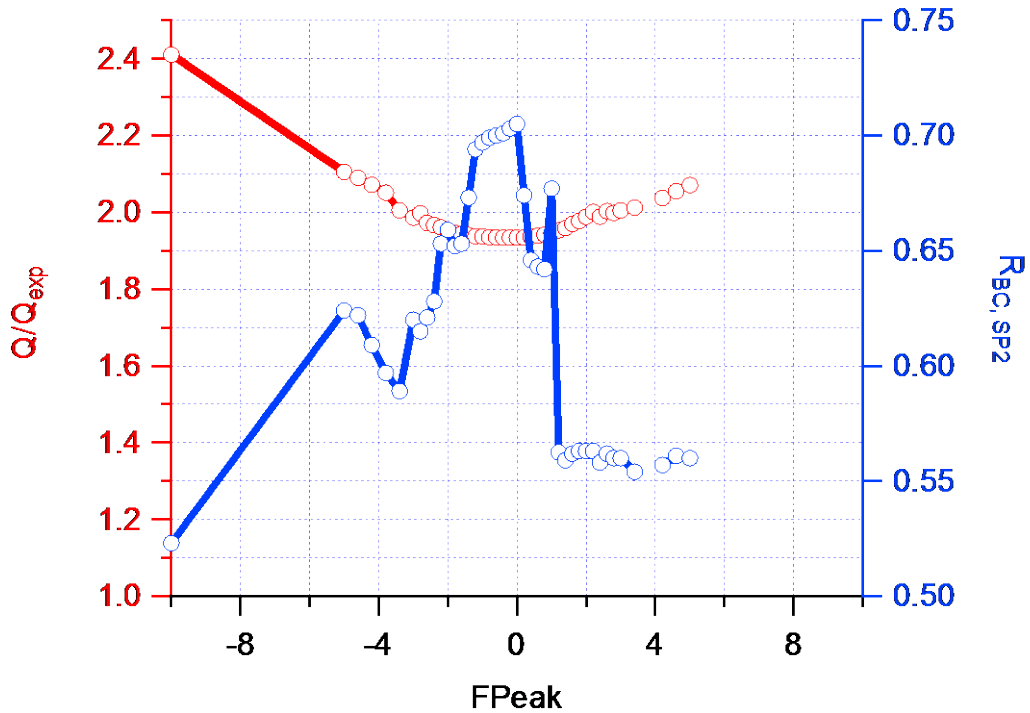

Figure C-2: (Left Axis) Q/Q_{exp} for the selected 5-component solution with the fixed LOA contribution plotted as a function of FPeak. **(Right Axis)** Correlation between HOA and rBC from the SP2 as a function of FPeak for the selected 5-component solution.

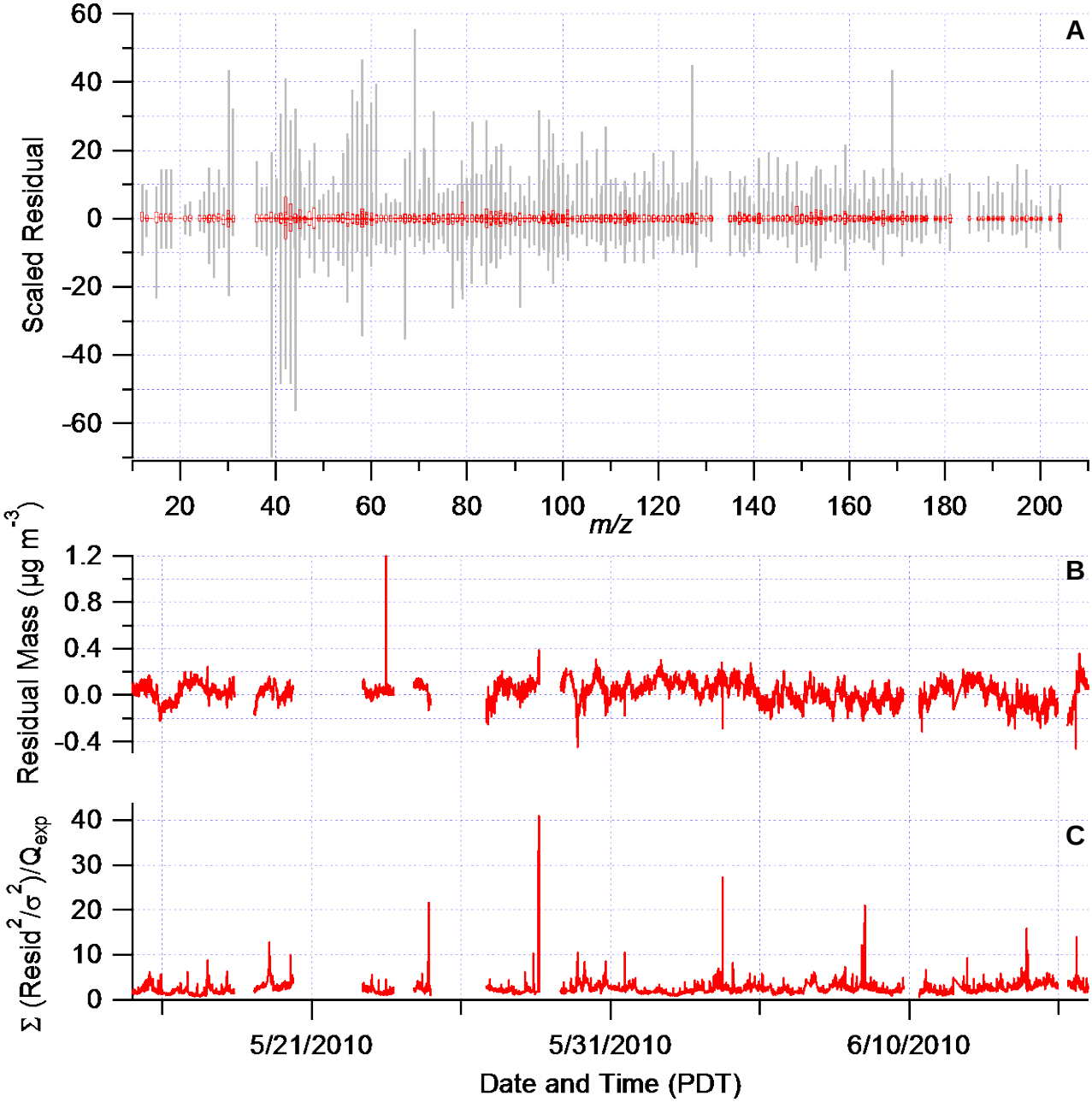

Figure C-3: (A) Box-and-whisker plot of residuals for each organic ion scaled to the predicted error from the error matrix. The boxes represent that 25th and 75th percentiles, and the whiskers represent the 5th and 95th percentiles. **(B)** Time series of the residual organic mass (= measured mass – reconstructed mass from PMF). **(C)** Time series of Q/Q_{exp} (i.e., the residual squared divided by the predicted error squared, which is then normalized to Q_{exp}).

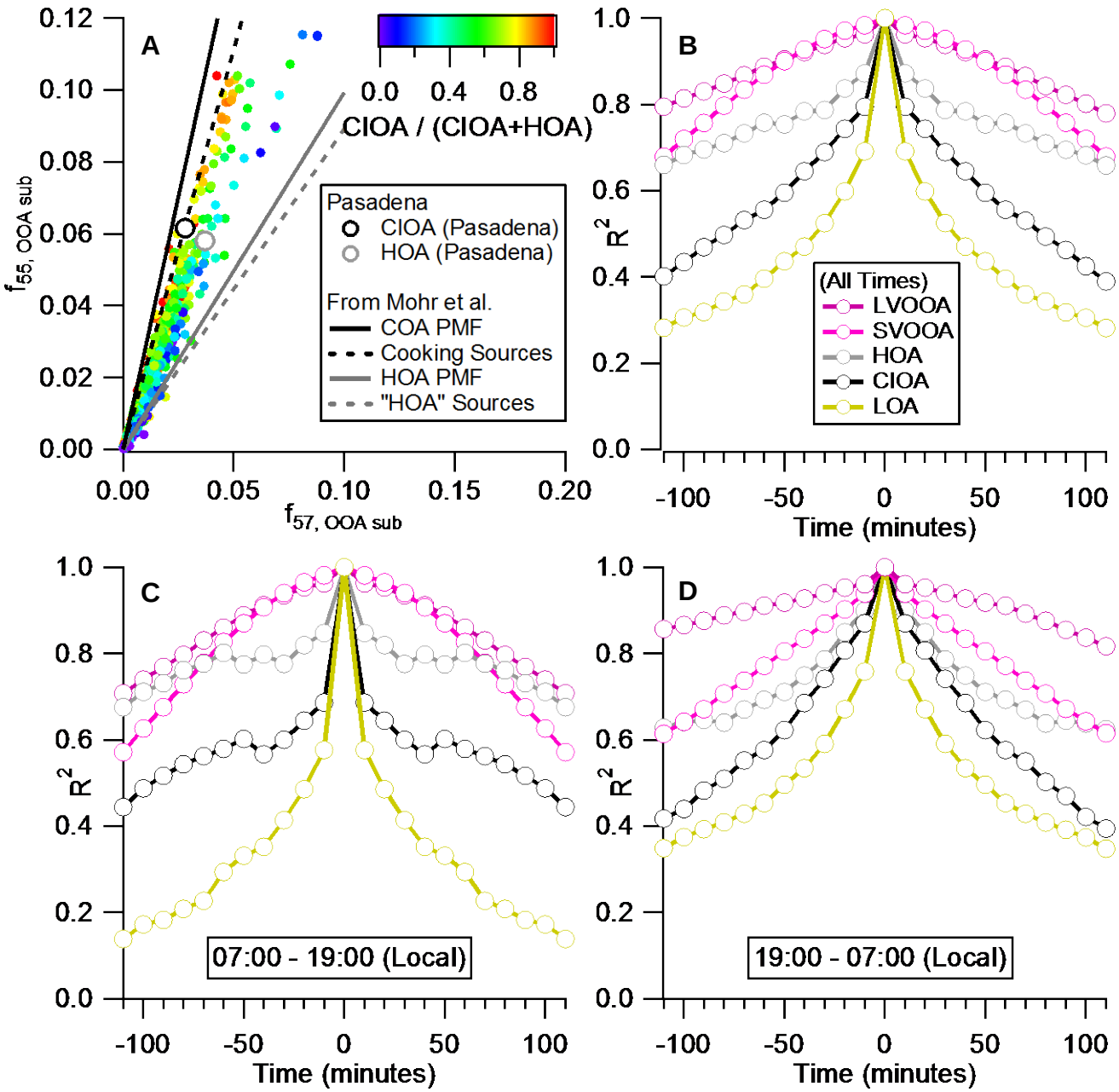

Figure C-4: (A) Scatter plot of $f_{55,\ OOA\ sub}$ versus $f_{57,\ OOA\ sub}$ colored by the relative amount of CIOA (markers). Also shown is f_{55} versus f_{57} for CIOA (black circle) and HOA (gray circle). The lines represent linear fits of f_{55} versus f_{57} data from previously reported cooking organic aerosol (COA) and HOA PMF factors (solid lines) as well as from cooking and traffic source emission studies (dashed lines). The linear fits are reproduced from Mohr et al. [2011]. **(B)** Auto-correlations for the PMF component time series over +/-110 minutes. Also shown are auto-correlations for daytime periods **(C)** and nighttime periods **(D)**.

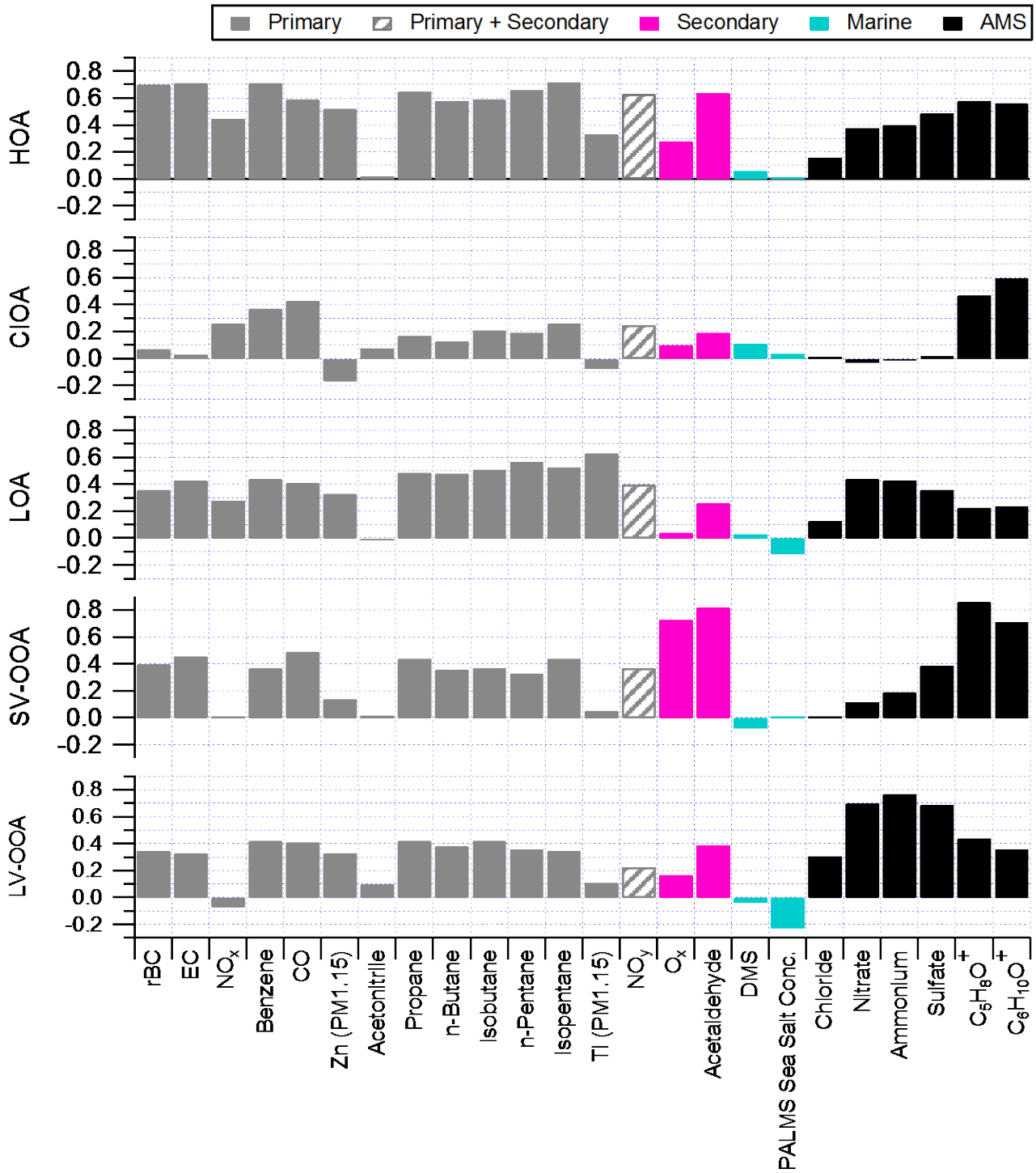

Figure C-5: Bar graph summarizing the correlations of the PMF factors with key tracer species. The correlations are taken from Table 3 in the main text. The bars are colored by the tracer classification.

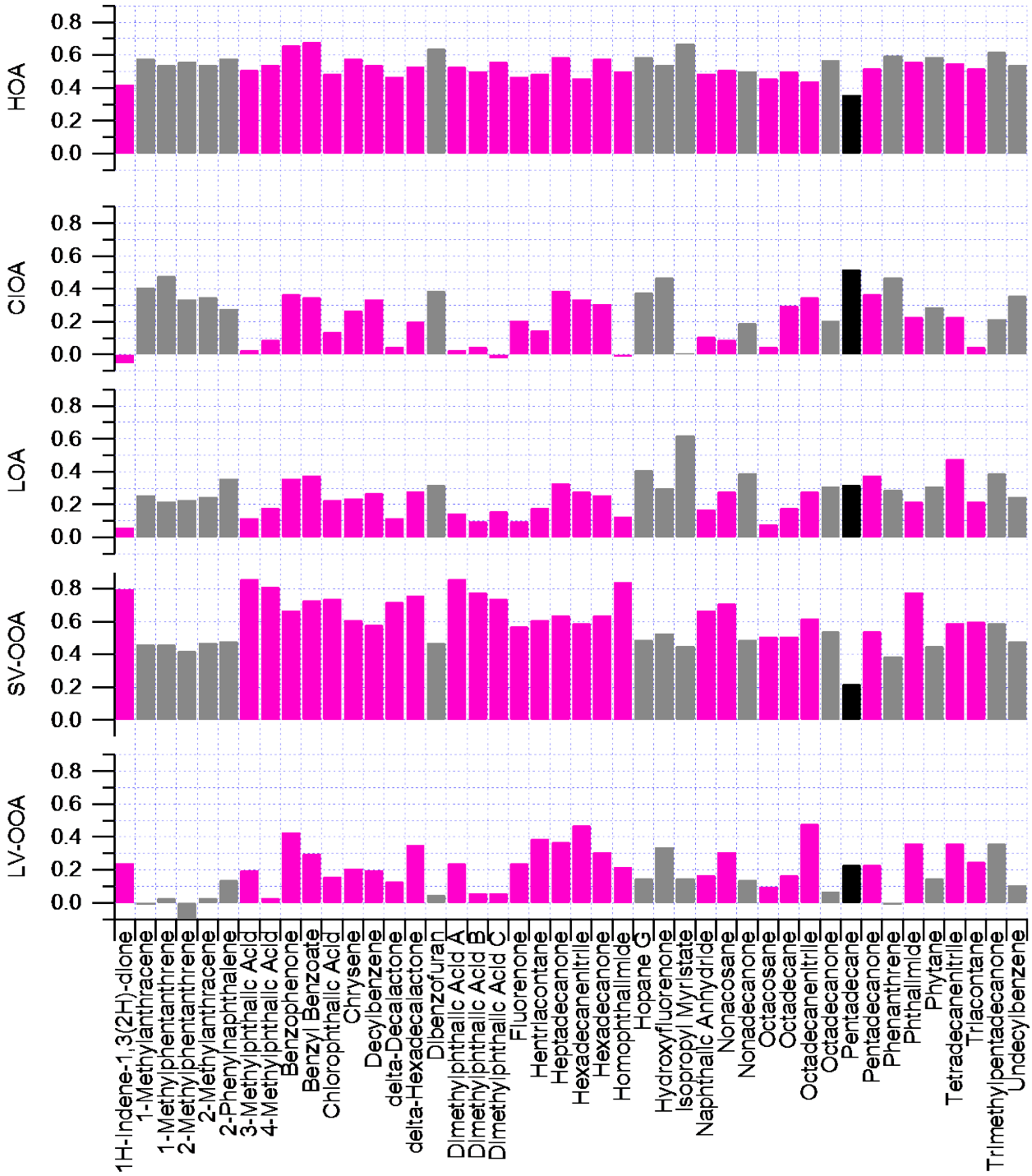

Figure C-6: Bar graph summarizing the correlations of the PMF factors with 2DTAG compound concentrations. The correlations are taken from Table 4 in the main text. The bars are colored to indicate the PMF factor exhibiting the highest correlation with each compound (Grey = HOA, Black = CIOA, Pink = SVOOA).

Appendix D: Real-time Measurements of Secondary Aerosol from the PAM Reactor

D.I. Summary

Recent field studies reveal large formation of secondary organic aerosol (SOA) under urban polluted conditions. To study this formation in real-time, a Potential Aerosol Mass (PAM) flow reactor was deployed with submicron aerosol size and chemical composition measurements during the CalNex campaign in Pasadena, CA, in 2010. A high-resolution aerosol mass spectrometer (AMS) and a scanning mobility particle sizer (SMPS) alternated sampling ambient and reactor-aged aerosol every few minutes. The PAM reactor produces OH concentrations up to 4 orders of magnitude higher than in ambient air, achieving equivalent aging of ~2 weeks in 5 minutes of processing. OH radical concentration was stepped every 20 minutes to obtain measurements of real-time SOA formation at multiple aging levels. Results show enhancement of both SOA and inorganic aerosol from aging. The enhanced OA mass from reactor aging peaks at night, in the absence of ambient photochemistry, and correlates with trimethylbenzene concentrations, thus indicating the dominance of short-lived SOA precursors in the LA Basin. Aging in the reactor mimics atmospheric processing as the elemental composition of ambient and reactor measurements, when plotted in a Van Krevelen diagram, follow similar slopes; additionally, reactor measurements extend over a larger range of oxygen-to-carbon ratios (O/C). While reactor aging always increases O/C, often beyond maximum ambient levels, we observe a transition from functionalization to fragmentation oxidation reactions at intermediate OH exposure levels, with fragmentation dominating at maximum OH exposures. Maximum net SOA production is observed between 3-6 days of aging ($4.0–8.0\times10^{11}$ molec. cm^{-3} s) and decreases at higher exposures. Results show the value of PAM-AMS as a tool for in-situ evaluation of changes in OA concentration and composition due to SOA formation and POA oxidation. A publication is in preparation reporting these findings.

D.II. Experimental

To study SOA formation in the LA Basin, we used a potential aerosol mass (PAM) photochemical flow reactor [*Kang et al.*, 2011; *Kang et al.*, 2007] at the Pasadena ground site during the CalNex 2010 field campaign. This reactor, a small (13.1 L) flow-through reactor, with reduced wall losses and rapid response time, was used to expose ambient air to high levels of OH and O_3. These oxidants are produced when UV light from two low-pressure mercury lamps (model no. 82-9304-03, BHK Inc., with discrete emission peaks at 254 nm and 185 nm) initiates O_2, H_2O and O_3 photochemistry. We use the term "aging" to refer to the combined effect of OH, O_3, and light exposure in the flow reactor, although reactions in the chamber are thought to be almost completely dominated by OH. The intensity of aging was stepped by adjusting between 50–110 VAC the voltage supplied to power the lamps, which modulates the photon flux and consequently the quasi steady-state oxidant concentrations in the reactor.

Ambient air was continuously sampled in an open flow-through configuration via a 14-cm opening. The PAM flow reactor output was measured by an Aerodyne high-resolution time-of-flight aerosol mass spectrometer (AMS) [*DeCarlo et al.*, 2006], a scanning-mobility particle sizer (SMPS, TSI Inc., Model 3936 with TSI 3010 CPC), an O_3 monitor (2B Technologies, Model 205), and a SO_2 Pulsed Fluorescence analyzer (Thermo Scientific, Model 43i Trace Level-Enhanced). Fast switching valves were used to automatically alternate AMS and SMPS sampling between the reactor and ambient sample line with 5 minute resolution, as seen in

Figure D-1. Both the reactor and ambient sample lines were located adjacent to one another, on the roof of the instrument trailer at the Pasadena ground site. This setup allowed near-continuous measurements of both photochemically-aged and ambient aerosol. The AMS measurements, analysis, and operational information are detailed above in Section 2.II. Oxidant concentrations in the reactor were stepped in 20 minute intervals, in a three hour cycle (Figure D-2). As lamp intensity increased, O_3 and OH concentrations increased in the reactor. To account for particle losses due to the additional residence time of the reactor (4 minutes), reactor concentrations have been normalized to ambient levels during each period with lights off. O_3 and SO_2 measurements were used to calculate OH exposure in the reactor. With these two gas phase measurements OH exposure is determined by both real-time SO_2 decay measurements and calibrated O_3/H_2O/Flow rate approximations from laboratory data.

D.III. Results

The 24 h time series of ambient and reactor AMS data are shown in Figure D-3. The series are representative of the diurnal profiles observed from 06/04/2010 to 06/10/2010. The oscillations in reactor data are due to OH exposure stepping as shown in Figure D-2. Eight hour day and night periods are highlighted to indicate the period of active ambient photochemistry. Ambient nitrate and ammonium concentrations peak in early morning hours before sunrise, while organic aerosol peaks in the late afternoon, the most photochemically active part of the day. While reactor-aged inorganic aerosol peaks at the same time as ambient, reactor-aged SOA peaks overnight about 8 h before the ambient OA peak. The nighttime reactor-aged OA mass peaks at approximately the same level as the following day's ambient OA concentration, and the daytime reactor-aged OA mass is not enhanced significantly above the ambient OA mass. These results indicate the precursors dominating SOA mass are very reactive. By midday these precursors have reacted away and are not available to contribute much to further SOA formation.

As seen in Figure D-4, organic mass enhancement (reactor OA – ambient OA) has a similar diurnal profile as trimenthylbenzene (TMB; τ_{OH} ~ 3hrs) and not benzene (τ_{OH} ~6 days). Both TMB and organic mass enhancement have diurnal profiles out of phase with OOA (derived from ambient AMS PMF analysis). This relationship further suggests SOA formation is dominated by short-lived precursors.

The relative organic enhancement ratio (ER_{OA} = reactor OA / ambient OA) is plotted with respect to photochemical age in Figure D-5 for the period from 06/04/2010 20:00 to 06/09/2010 20:00. OA mass is enhanced up to 2.5 times ambient OA from aging. Organic enhancement peaks around 3 to 6 days of aging and reactor OA mass decreases below ambient after 8 days aging. The majority of mass enhancement is seen at night. During the night the boundary layer is lower and highly reactive precursors accumulate due to the absence of photochemistry. In contrast, during the day the emissions are diluted by the higher boundary layer, and reactive precursors may be depleted due to ambient photochemistry. Interestingly, when sampling aged air masses already processed by the atmosphere, the reactor does not significantly add mass, but does continue the aging process. This continued aging process appears to consist of oxidation/fragmentation reactions as described in the next paragraph.

Comparing reactor and ambient OA elemental composition in a Van Krevelen diagram, the reactor data follows a trend very similar to ambient data (Figure D-6). This similarity is consistent with the reactor approximately representing the relevant ambient oxidation chemistry

during the CalNex field campaign. Reactor O/C ratios increase with aging and span a wider range than ambient observations. In Figure D-7 the evolution of O/C and H/C with OH exposure and relative organic enhancement is plotted, and continual oxidation with OH exposure is observed. The maximum organic enhancement (i.e., net SOA production) is observed at intermediate exposures and O/C ratios (OH_{exp} ~7.5×10^{11} molec. cm^{-3} s and O/C ~1.1). OA mass loss (ER_{OA} < 1) is observed at the highest O/C ratios and OH exposures, which implies that fragmentation reactions leading to oxygen-containing functional groups dominate SOA chemistry. A similar trend is observed by Lambe et al. [2012] for SOA from OH oxidation of alkane precursors.

D.IV. Conclusions

Real-time measurement of potential SOA formation and aging was carried out with a photochemical reactor coupled to an AMS and SMPS during the CalNex field campaign. High OA enhancement was observed at night with reactor-aged OA mass peaking at concentrations similar to daytime ambient OA mass. The net OA enhancement time series correlates with short-lived VOCs, suggesting that short-lived precursors dominate SOA formation in the LA Basin. When elemental composition is plotted in a Van Krevelen diagram, the similarity between ambient and reactor-aged OA is consistent with the flow reactor accurately representing ambient oxidation. Total OA mass was observed to decrease at very high OH exposures while O/C continued to increase. Maximum net SOA production was observed at intermediate OH exposures and O/C ratios, indicating an increasing importance for fragmentation reactions at long aging times. Results from PAM reactor deployment during CalNex show the reactor is a viable tool for real-time measurement of SOA formation and oxidation across a range of photochemical ages.

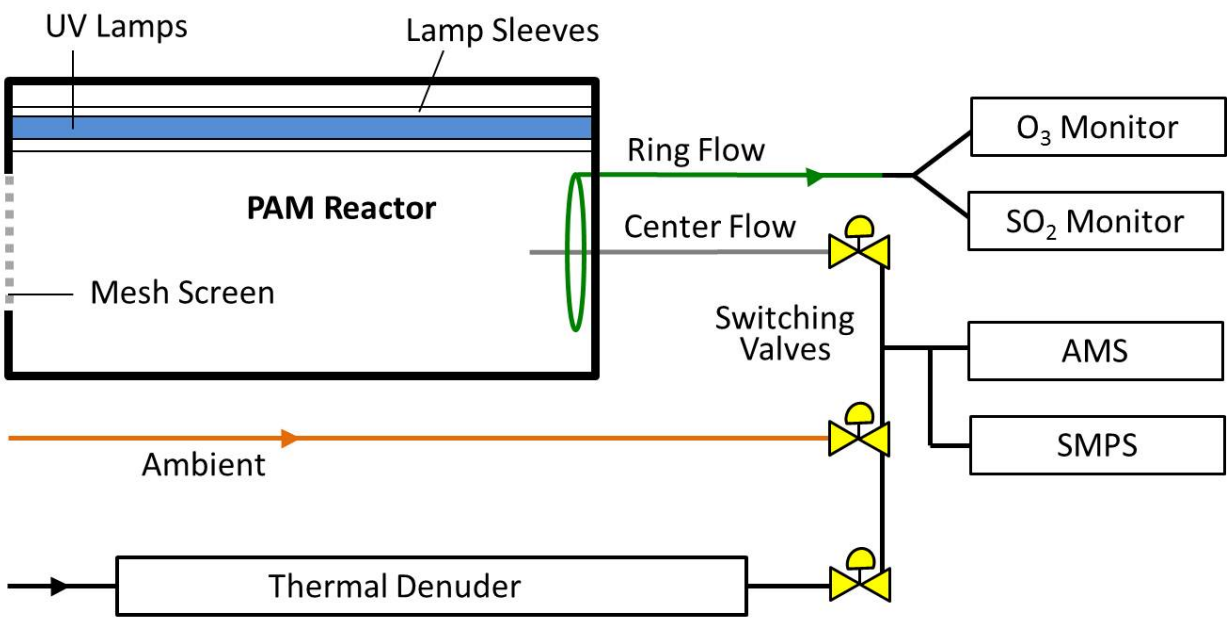

Figure D-1: Schematic of the potential aerosol mass (PAM) reactor coupled to an Aerodyne high-resolution time-of-flight aerosol mass spectrometer (AMS), scanning-mobility particle sizer (SMPS), sulfur dioxide (SO_2) analyzer, and ozone (O_3) monitor. A bypass line (orange) allows direct sampling of ambient air. Computer controlled-switching valves (yellow) allow for regular sampling from the PAM reactor and ambient air. Voltage supplied to UV lamps (blue) can be varied to control oxidant concentrations in the chamber. Ring flow (green) is a Teflon™ line and is used for gas phase measurements. Center flow (gray) is a stainless steel line that continuously pulls the sample for aerosol analysis.

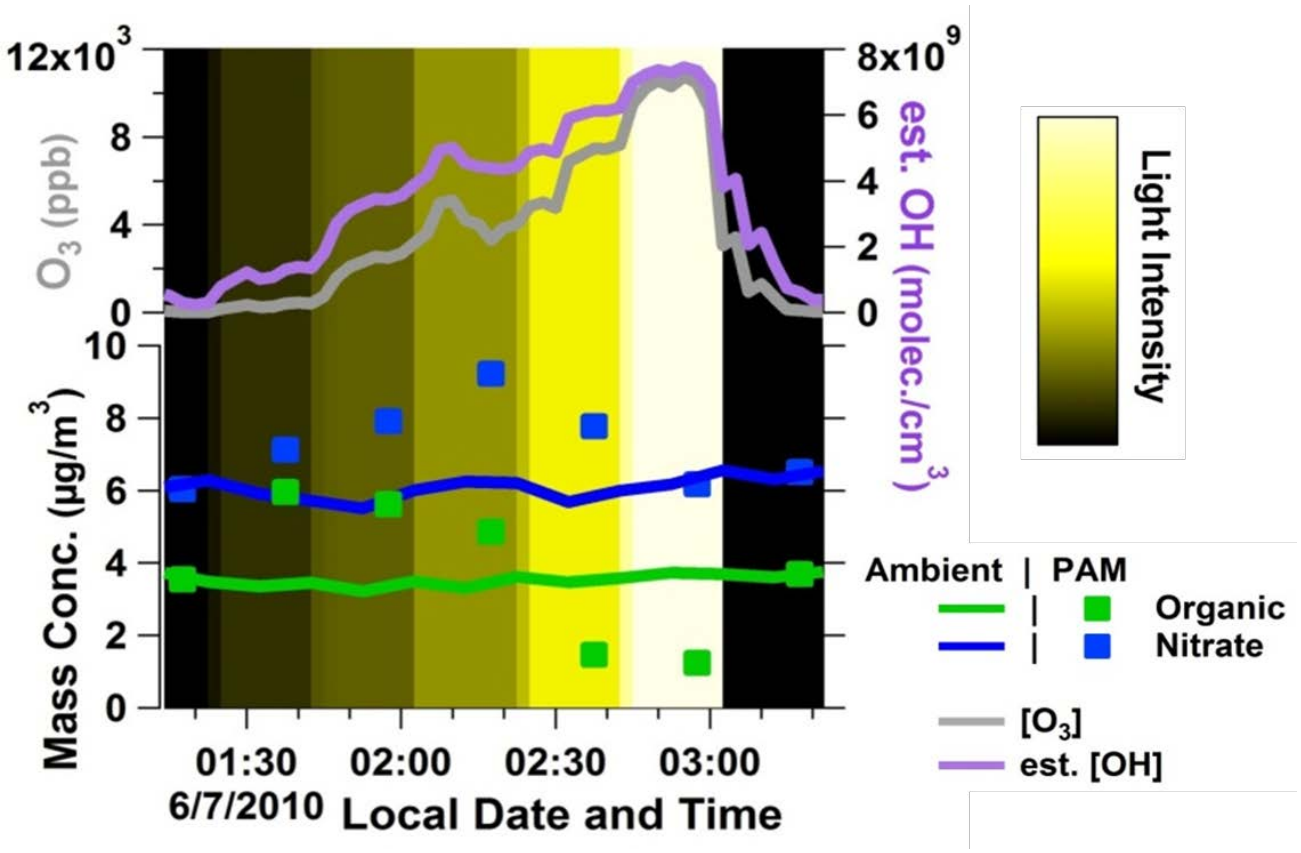

Figure D-2: Time series of OH scanning in the PAM reactor. A representative 3 hour (06/07/2010 01:14:00 – 06/07/2010 03:22:00) time series of lamp intensity (black to yellow gradient) in the reactor is plotted. Also shown are the reactor oxidant (O_3 and OH) concentrations and AMS measured organics and nitrate for ambient (solid lines) and reactor (markers) sampling.

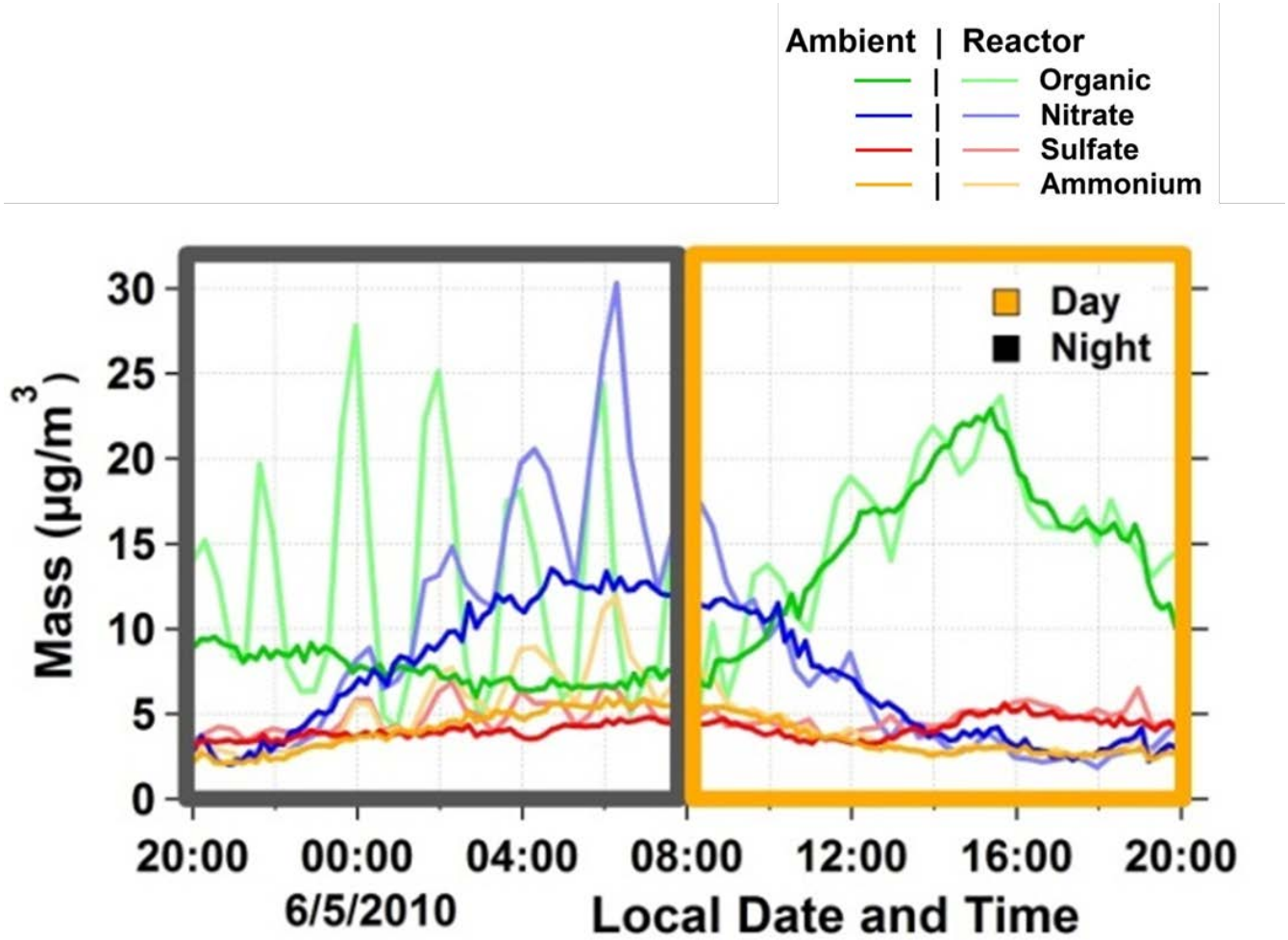

Figure D-3: Diurnal profile of AMS mass concentrations for ambient (dark) and reactor (light) measurements from 06/04/2010 20:00:00 to 06/05/2010 20:00:00. Day (orange) and night (gray) are indicated by the large rectangular frames.

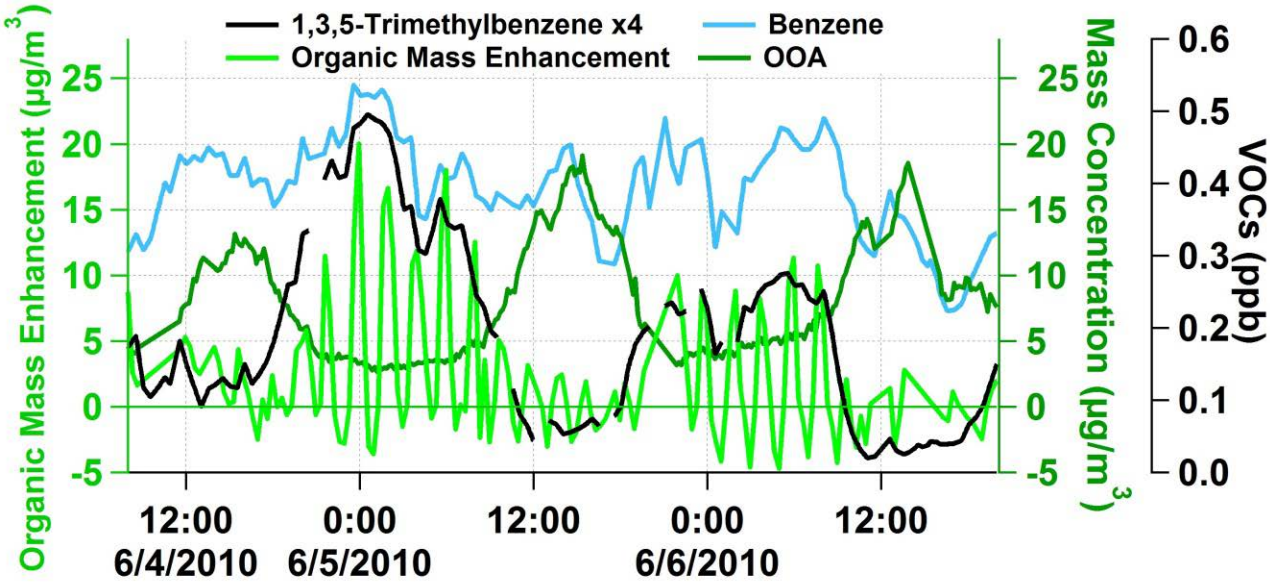

Figure D-4: Times series for SOA precursors, OOA, and organic mass enhancement. Volatile organic compounds (VOCs) were measured by in-situ Gas Chromatography Mass Spectrometry (GC-MS). The OOA time series is from the PMF analysis of the AMS measurements (dark green). The organic mass enhancement is defined as reactor OA minus ambient OA (light green).

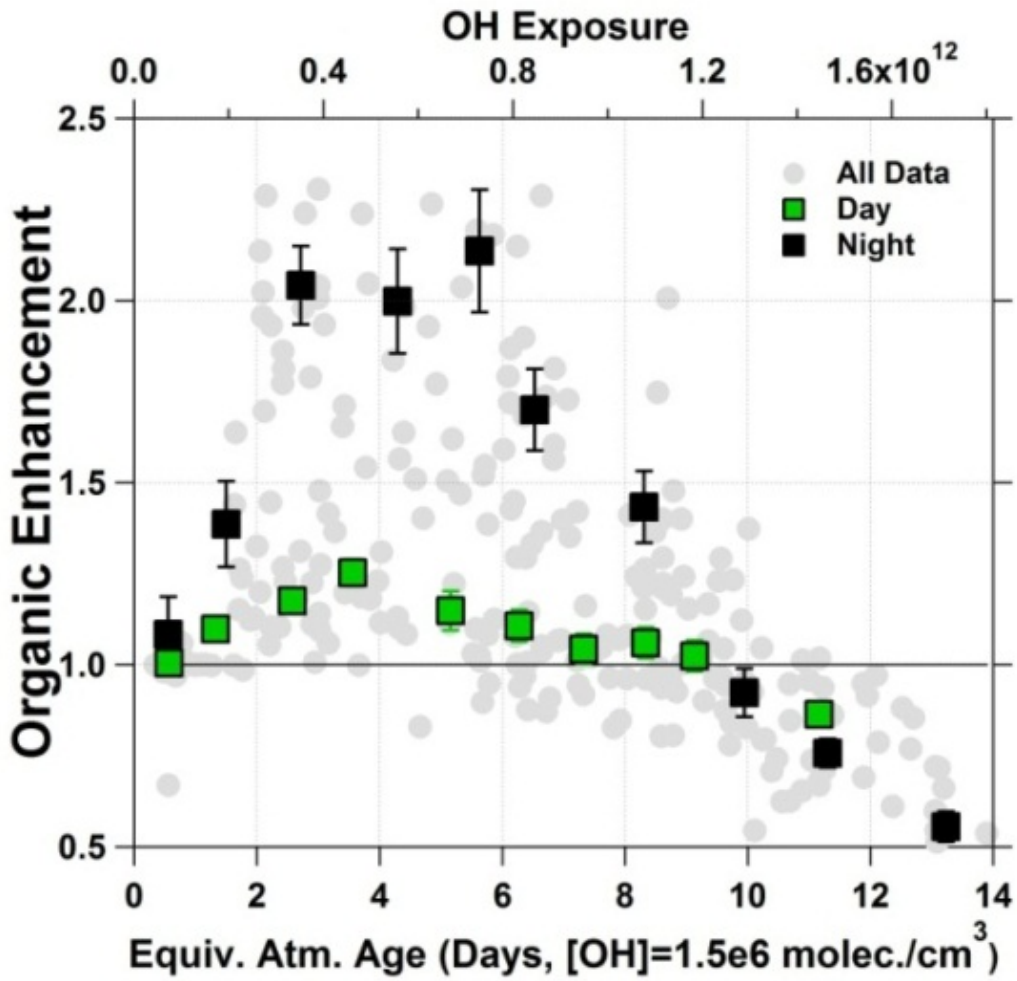

Figure D-5: Relative organic aerosol enhancement (reactor OA / ambient OA) plotted versus reactor photochemical age for 06/04/2010 20:00:00 – 06/09/2010 20:00:00. Day (green) and night (black) measurements are separated and binned with error bars indicating standard error.

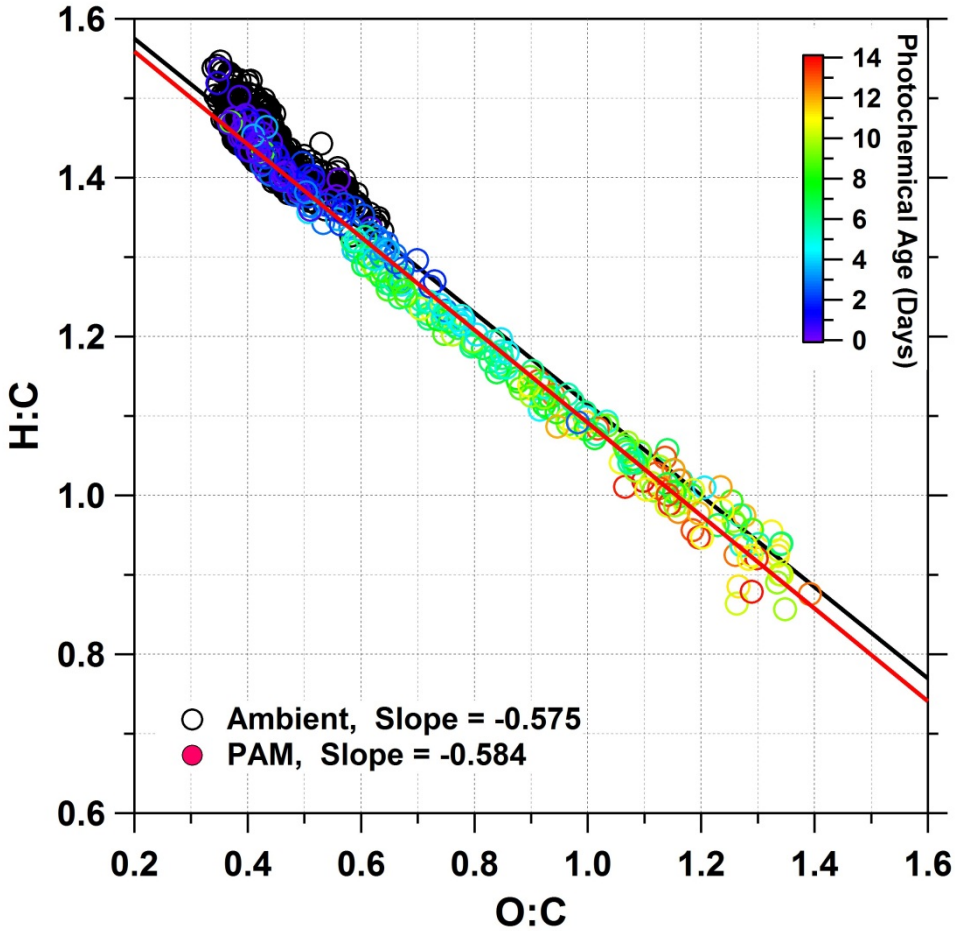

Figure D-6: Van Krevelen diagram for ambient (black circles) and reactor (colored circles) measurements taken during 06/04/2010 20:00:00 – 06/09/2010 20:00:00. Also shown are orthogonal distance regression linear fits for ambient (black line) and reactor (red line) data. Reactor measurements are colored by photochemical age in days.

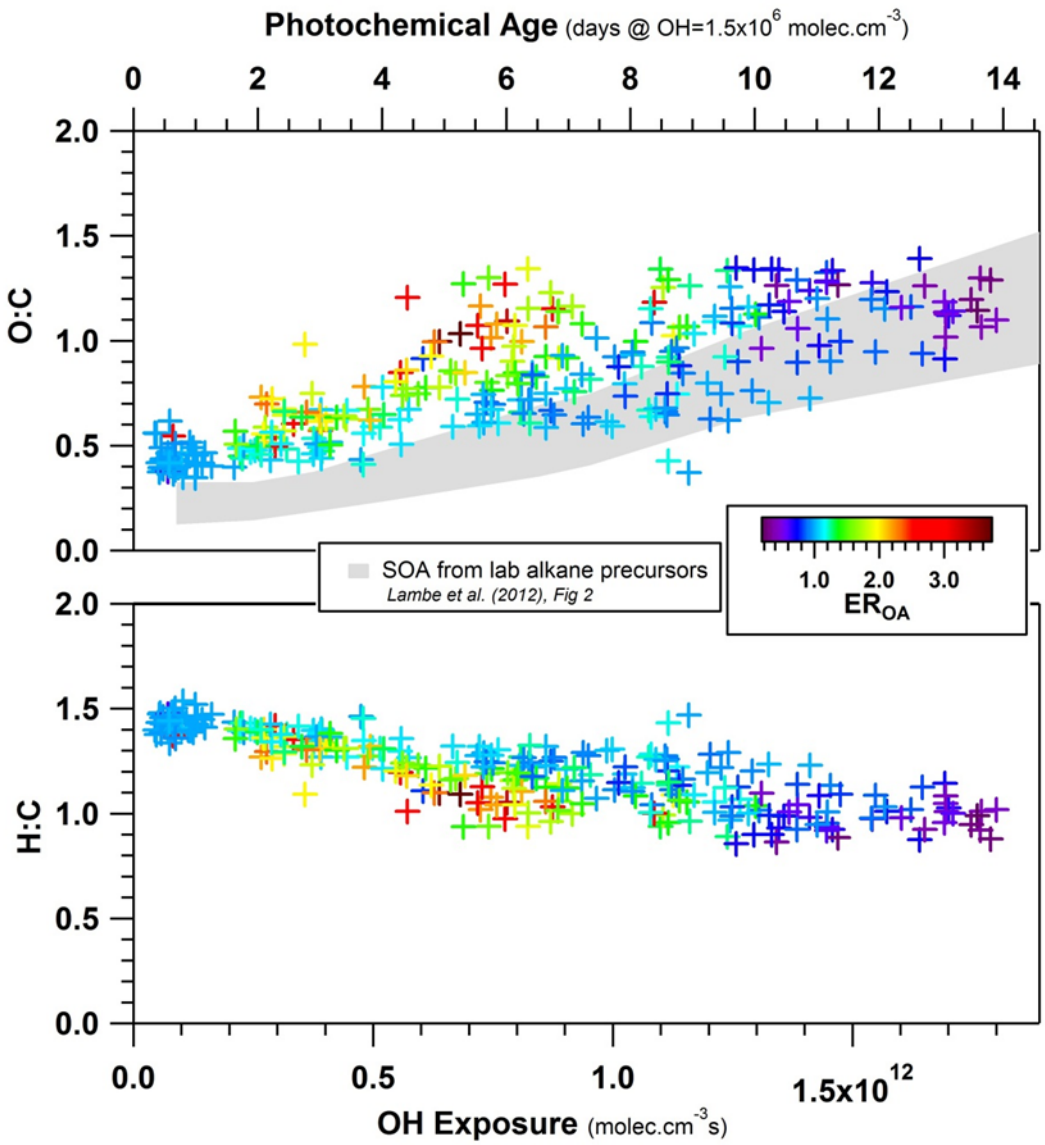

Figure D-7: Oxygen-to-carbon (O/C) and hydrogen-to-carbon (H/C) elemental ratios for the total OA mass measured from the PAM reactor with respect to photochemical age from 06/04/2010 20:00 to 06/09/2010 20:00. The data are colored by the relative organic enhancement (reactor OA / ambient OA). The results of Lambe et al. (2012) are also presented (gray region).

Appendix E: Comparison of CalNex measurements against CARB monitoring network

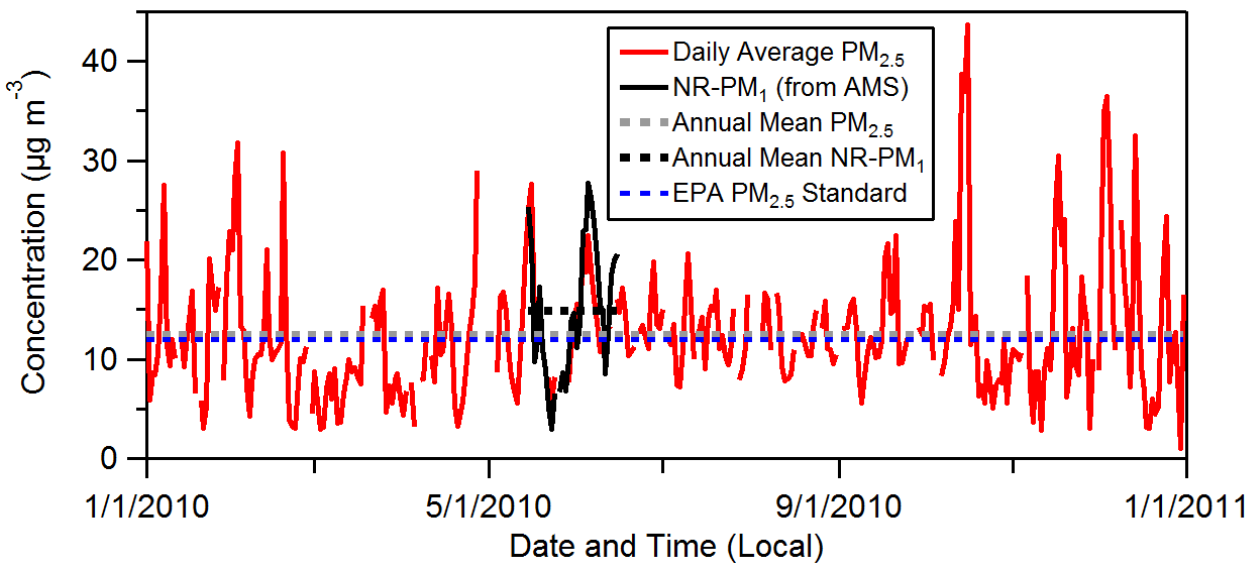

Figure E-1: Average daily $PM_{2.5}$ concentrations from the Burbank-W Palm Ave CARB monitoring station for 2010 (red trace). Also shown is the non-refractory PM_1 concentration measured by an Aerodyne Aerosol Mass Spectrometer (AMS) during CalNex. (Note: the non-refractory component accounts for more than 90% of the total PM_1 concentration as shown in Figure 2). The dotted lines indicate the annual mean $PM_{2.5}$ concentration from the Burbank-W Palm Ave monitoring station (grey), the mean NR-PM_1 during CalNex (black), and the current EPA $PM_{2.5}$ annual average standard (blue).